Development of a passive SHM impact damage detection method for monitoring composite aerospace structures

J. Voges

Delft University of Technology
Faculty of Aerospace Engineering

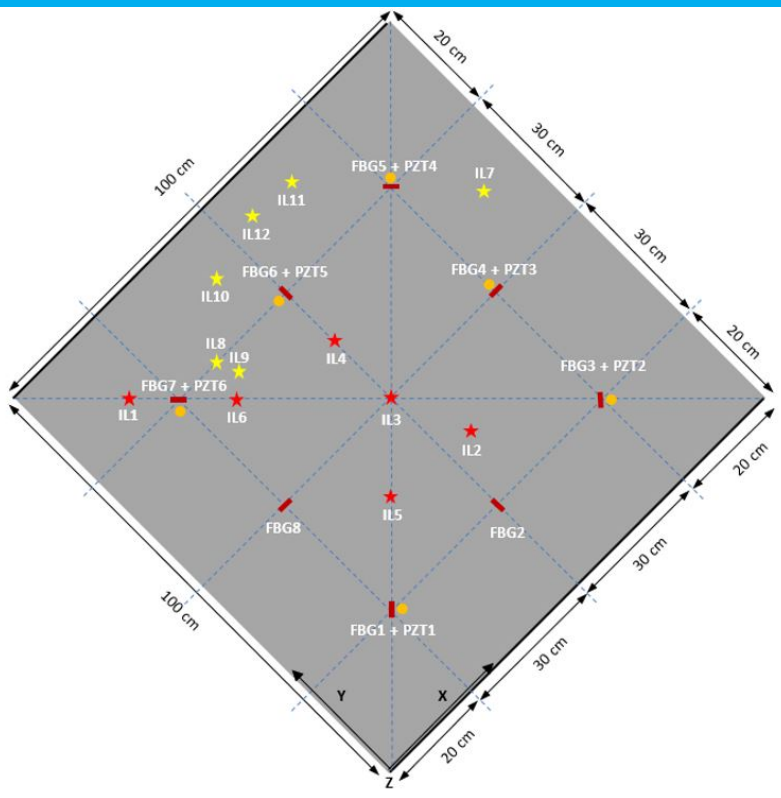

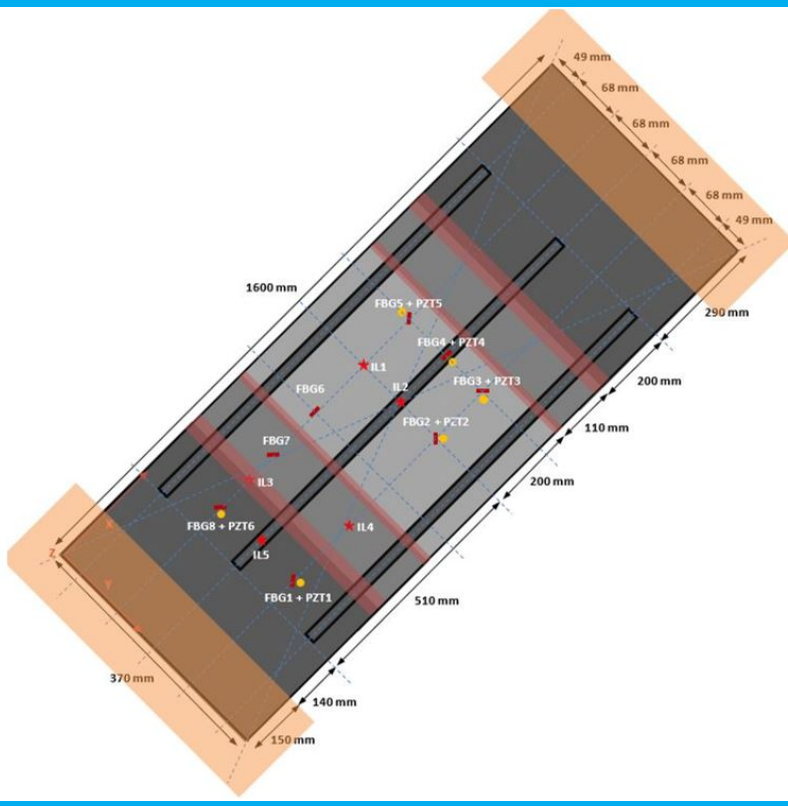

TU Delft

Development of a passive SHM impact damage detection method for monitoring composite aerospace structures

by

J. Voges

performing a master thesis project to obtain the degree of Master of Science
at the Delft University of Technology.

Faculty:	Aerospace Engineering	
Project duration:	November 4, 2022 – April 19, 2024	
Thesis supervisors:	Dr. R.M. Groves	TU Delft
	F.P. Grooteman	NLR
Thesis committee:	Ir. J. Sinke	Chair
	Dr. Jurij Sodja	Examiner
	Dr. R.M. Groves	TU Delft supervisor
	F.P. Grooteman	NLR supervisor

*This thesis is company confidential (NLR) and cannot be made public until **19 April 2027**.*

Abstract

Safety and reliability of aircraft structures are of main concern within the aerospace industry, preferably without influencing the availability of the aircraft and maintenance and operation costs. As damages in composites can be hard to detect, methods are being developed to detect damages which can potentially lead to a (catastrophic) failure of a (sub)system. Interest in structural health monitoring (SHM) has thus gained a strong interest within aerospace engineering, with the development of new systems or optimising existing ones to contribute to a safe and reliable aircraft. This research focuses on the development of an impact damage detection and quantification method for composite structures. The main research objective of this thesis is to investigate the capabilities of a PZT and a state-of-the-art FBG sensor system for passive impact damage detection and quantification on a simple composite panel and a complex stiffened composite structure.

This research objective is achieved by developing an algorithm based on the wavelet transform, making it possible to detect the damage by means of signal analysis. The data analysed by this algorithm was obtained by extensive impact testing on a flat and a stiffened composite panel, using a high sampling rate PZT and state-of-the-art FBG sensor systems. By comparing pristine non-damaging impacts with damaging impact results, verified by active phased array scans, impact damages were detected on both panels. By applying known acoustic emission peak frequency values, the failure modes matrix cracking, delamination, fibre/matrix debonding and fibre failure were detected. Delaminations, fibre/matrix debonding and fibre failure features are characterized by slope changes in the wavelet transform results, while the pristine cases show near linear trends. This linearity decreases when increasing the amount of decomposition levels. Matrix cracking is characterized by an energy drop, when compared to the pristine impact results. These characteristics tend to be similar, even with structural obstacles such as wave propagation through stiffeners, thickness changes and after direct impact on a skin section connected to a stiffener. Thickness changes have more influence on the detectability than propagation through or on a stiffener itself. Also, this research has shown that the detectability of an impact damage decreases for high frequency waves. These conclusions are drawn from the PZT sensor data, as the FBG data did not contain the relevant high-frequency components of the impact damage event.

Contents

List of Figures

List of Tables

Nomenclature

1D	one dimensional
2D	two dimensional
AE	acoustic emission
AI	artificial intelligence
AIC	Akaike's developed information criterion
ANN	artificial neural network
APC	angled physical contact
AR	auto-regressive
ASE	amplified spontaneous emission
AWG	arrayed waveguide grating
BVID	barely visible impact damage
CF/EP	carbon fibre/epoxy
CFRP	carbon fibre reinforced polymers
CTE	coefficient of thermal expansion
CWT	continuous wavelet transform
dB	decibel
DLR	German Aerospace Center
DP	damage parameter
DWT	discrete wavelet transform
EMI	electromagnetic interference
FBG	fibre Bragg grating
FDA	frequency domain analysis
FEM	finite element method
FFT	fast Fourier transform
FIR	finite impulse response
FOD	foreign object damage
FOS	fibre optic sensors
FPE	final prediction error
FRP	fibre-reinforced polymers
FT	Fourier transform
GFRP	glass fibre reinforced polymers
GMM	global matrix method
IIR	infinite impulse response
IL	impact location
ML	machine learning
MRA	multi resolution analysis
NCV	nested cross-validation
NDT	non-destructive testing
NLR	Netherlands Aerospace Centre
OSA	optical spectrum analyzer
PAF	partial autocorrection function
PEKK	Polyetherketoneketone
PSD	power spectrum density
PSO	particle swarm optimization
PWAS	piezoelectric wafer active sensors
PZT	Lead Zirconate Titanate
RC	reinforced concrete
RMS	root mean square
SG	stepwise gridsearch
SL(E)D	Superluminescent diode

SNR	signal-to-noise ratio
SOA	semiconductor optical amplification
STFT	short-time Fourier transform
SVD	singular value decomposition
TDA	time domain analysis
TDM	time division multiplexing
TFDA	time-frequency domain analysis
TMM	transfer matrix method
ToA	time of arrival
ToF	time of flight
UAV	unmanned aerial vehicle
WDM	wavelength division multiplexing
WPT	wavelet packet transform
WT	wavelet transform

Acknowledgements

This master thesis report marks the end of a very educational period at TU Delft for me. I would like to thank Dr. Roger Groves, my TU Delft supervisor, for great guidance, helpful discussions, flexibility and patience throughout this thesis project. I would also like to thank my NLR supervisors, Frank Grooteman and Jan Willem Wiegman, for the great support, sharing your experience and providing me with new insights during this project. And not to forget, thank you to all NLR engineers for supporting the tests required for this project. It was a pleasure for me to work with you all at NLR!

Doing this master thesis part time next to my job, required me to spend my spare time and many evenings working on this project. Without the support and faith of my family and friends, this would not have been possible for me to achieve. I would like to thank Jens van der Helm, with who I started the adventure of doing a master at TU Delft in parallel with our jobs. Despite the challenges we faced, we kept each other motivated throughout the years. I want to give a special thanks to Manon. Spending many nights on the project was far from easy for me. But during the entire project, you supported me and kept me motivated to achieve this goal.

Jordy Voges
Delft, April 19th 2024

1 Introduction

This research focuses on developing an impact damage detection and quantification algorithm for composite structures, for structural health monitoring. To introduce technical topics in the thesis, this section will briefly provide a definition of composite materials, failure modes of composites and introduce structural health monitoring. A thesis outline will be provided in the last section of the chapter.

1.1. Composites

A composite is a macroscopic mixture of two or more materials, consisting of a matrix material in which another (phase of a) material is embedded. [1] These composites can be a mixture of any type of material, but it should be beneficial to combine them to ensure improved properties. Within the aerospace industry, the most common form of composite material is the combination of a fibre embedded in a polymer matrix material, so called fibre-reinforced polymers (FRP). [2] The most common used fibres are glass fibres and carbon fibres, due to their low density and high Young's modulus in fibre direction. [1] The matrix is most often made of a high quality thermoset or thermoplastic polymer, of which the choice for use is determined by the application and operating environment. [1] The function of the matrix is to allow load introduction in the embedded fibres, keeping the fibres in place, allowing (limited) transverse and compressive loads and protecting the fibres from the environment and external (impact) damage. [2] The main advantages of FRPs compared to metallic materials are their high tailorability due to the vast combination of materials and fibre orientations and the limited weight due to designing the FRP required for specific performances. Corrosion resistance and high fatigue life are also excellent properties of FRPs, which make them the material choice for modern aerospace structures. [3]

1.2. Composite failure modes

Despite the many advantages that FRPs have compared to metals, they are vulnerable to damages induced by external or internal forces during manufacturing or their in-service life-time. These damages are most often more complex than those of metals, making inspection and repairs more difficult and expensive. [3] External forces leading to damage in aerospace structures, are for instance introduced by impacts from birds, weather conditions (hail and lightning) and foreign object damage (FOD) from runways. [3][4] To detect and possibly quantify damage in a composite structure, it is important to understand the main types of damages and failures in these types of structures.

The most common defects that occur during service are delamination, matrix cracking, debonding of the fibre from the matrix and fibre breakage. [3] Delamination is the separation of two different laminates in the composite material, most often occurring due to compressive and out-of-plane loading. [3] Matrix cracking is the presence and propagation of a crack in the matrix material. [5] With this type of defect, the fibre material is unaffected but the damage affects the matrix properties. Debonding of the fibre from the matrix is a similar defect as matrix cracking, only the defect is initiated at the fibre-matrix interface. [5] This defect affects the load introduction from the matrix in the fibres and matrix properties. Fibre breakage is the debonding of the fibre itself, affecting the fibre properties within the composite. This

primarily has an effect on the tensile strength of the material, as a result of for instance overloading the composite in fibre direction. Matrix cracking, fibre-matrix debonding and fibre breakage are also the three most common damages upon impact during the service of an aircraft, [3] which are schematically represented in Figure 1.1.

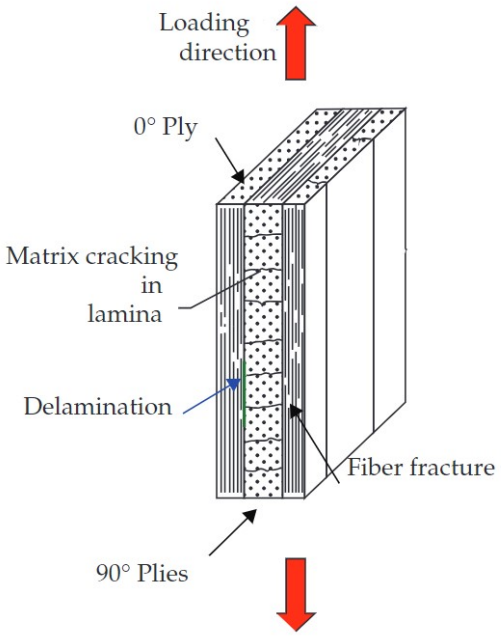

Figure 1.1: Schematic representation of composite laminate failure modes, taken from [5].

1.3. Structural Health Monitoring

Structural health monitoring (SHM) consists of numerous techniques to monitor the health of the structure by means of strain monitoring, damage detection and characterisation. [6] This is done by means of detection, localisation and quantification of the induced damage in the composite. [7] SHM relies on sensors applied on or integrated in the structure, which are lightweight, affordable and may not affect the integrity of the structure. [8] The overall goal of SHM is to ensure the integrity of the entire structure during its service live, which can be achieved by using active or passive SHM methods. [8] As mentioned in the previous section, there are many damages that can affect structural integrity, which can grow during the service live of the aircraft, of which barely visible impact damages (BVID) are of main concern. [4] These barely visible impact damages are hard to detect during routine visual inspections of the aircraft, especially in difficult to inspect areas, which can eventually lead to catastrophic failure of the structure when kept unnoticed. [8] Thus, it is necessary to create SHM methods that are able to detect BVID in an early stage, ensuring the service live of an aircraft.

SHM levels

SHM consists of the following five different levels as described in [9]:

- SHM0: Good quality control of the structure's condition
- SHM1: Online load monitoring
- SHM2: Identifying damage and its location
- SHM3: Damage quantification
- SHM4: Estimating the residual life of the structure

SHM0 is the lowest level of possible SHM, where quality control of the structure has the primary focus. Within this level, well known (active) non-destructive testing (NDT) methods are used during manufacturing, after installation and during regular scheduled maintenance. SHM level 1 uses the principle of real-time load monitoring, determining the loads on the structure by for instance using Lamb waves.

SHM2 uses the available data from the sensors to detect if there is damage and if so, to determine the location of this damage. SHM2 does not return the actual severity and size of the damage. This is where SHM3 is relevant, as this quantifies the size and severity of the detected damage. The equipment needed for this level of SHM on aircraft structures is still developing and not yet mature. The last level of SHM, SHM4, is used to predict the residual life time of a structure by analyzing large data sets obtained from the applied sensors. It is worth mentioning is that increasing the level of SHM, means that maintenance will be more preventative. This leads to near real-time monitoring of the structure, which will reduce costs and better predict the residual life in the measured structure. However, increasing the SHM level means the more complex the method will be, increasing training and equipment cost. [9]

1.4. Thesis outline

The basic theoretical knowledge required for the thesis will be introduced in Chapter 2. SHM will be further reviewed, including Lamb wave, passive SHM sensors, different domain analysis methods. The wavelet transform and some applicable wavelets will be introduced. Chapter 3 will briefly discuss the state-of-the-art literature regarding impact damage detection and quantification methods. From this literature review, the thesis research questions and objectives have been defined. Chapter 4 will focus on the most applicable wavelet transform method and wavelet for this thesis, answering the first research sub-question. This methodology basis is used to answer the second research sub-question in Chapter 5, in which an impact damage detection algorithm is developed and applied on a basic flat composite structure. This knowledge is used to answer the third research sub-question in Chapter 6, in which a more complex stiffened composite structure is analyzed by means of the developed algorithm. The main findings of the thesis are concluded in Chapter 7, also answering the main research question. This Chapter also addresses the current research limitations and the future research possibilities for further developing a real-time impact damage detection and quantification algorithm. Appendices are added to provide background information, including a test plan in Appendix A and the results of damages of all impact locations in Appendix B.

2 Theory

This section provides the basic theory and knowledge required for understanding impact damage detection and quantification. It is divided in three main topics, of which the first topic focuses on active and passive SHM. This is followed by theory on acoustic emission and guided waves. The second topic will give the basic theory of Lamb waves and how to process this type of wave. The third main topic is describing the Lead Zirconate Titanate (PZT) and fibre Bragg grating (FBG) sensor principles. The FBG interrogation method is briefly discussed, as this method is used during the testing phase of this thesis. The fourth main topic is the description of basic time, frequency and time-frequency domain analysis methods, focusing on signal filtering and the Fourier transform. This will be followed up by the wavelet transform description, distinguishing the continuous wavelet transform, the discrete wavelet transform and the wavelet packet decomposition. Finally, the different type of applicable wavelets for this thesis are described. This chapter will be concluded with a brief summary.

2.1. Active and passive SHM

As stated in the Section 1.3, structural health monitoring (SHM) monitors the integrity of the structure. This can be determined by both active and passive SHM methods. Active SHM methods are based on first exciting the structure and picking up the structural response by 'listening' sensors. By analyzing the difference between excitation and interrogation signals, damage can be detected, localized and quantified. Passive SHM only uses passive 'listening' sensors, which interrogate the structure without excitation. [10] Passive sensors can pick-up signals excited by impacts or vibrations from external sources such as impacts, internally excited vibrations due to damage occurrences and flight loads. [8] Different methods can be used for active and passive SHM, of which guided waves and acoustic emission will be further discussed due to its relevance for this thesis.

Acoustic Emission

Acoustic emission (AE) is a passive method which is used to identify primary and secondary events. [10] Primary AE events are characterized by sudden release of strain energy for a short period of time, existing from within the structure. This can be for instance due to abrupt delaminations, crack growth or fibre breakage within the composites. The frequency, intensity and duration of the wave characterizes the event which emits short bursts, propagating thought the structure. [11] Secondary AE events are initiated by external events, such as impacts. The waves, which are captured by the sensors, are elastic waves. The potential of the AE method, is that it has a real-time monitoring potential for microscopic-level damages and locations of both primary and secondary AE events. These can be located in the structure when multiple sensors are used. [10] Upon an impact event, the measured waves are initially from the impact event (primary wave), followed by a superposed high-frequency wave similar to waves that indicate a composite that has been damaged due to delaminations or breakage (reflected wave). [8] After primary or secondary AE damage events have occurred, the propagation of the wave is similar to guided wave propagation (e.g. Lamb waves). [11] The limitations of this method are that it is sensitive to noise, the specimen must be under a stress and it primarily provides qualitative damage detection. [12] Although earlier research had only been able to provide qualitative damage detection

results, recent research has shown that by using different approaches such as deep learning [13] and wavelet transforms combined with the random forest method [14], the damage type can be classified. AE signals have been measured primarily in the frequency range from 20 to 100 kHz, but can also have frequencies up to 1 MHz. [15] Qi [16] showed that using the discrete wavelet transform, three AE failure modes can be distinguished during static tensile testing. Fibre failure is detected at around 300 kHz, debonding of the fibre and matrix at around 250 kHz and matrix cracking at around 110 kHz. In other research, Gutkin et al. [17] defined the failure modes in CFRP in more detail, using different load tests where AE waves are monitored by broadband AE sensors with a range between the 100 - 1000 kHz. These results were compared with other peak frequency interpretations of different researchers. Figure 2.1 schematically shows the results of their tests, giving an indication of the frequency ranges in which damages may occur. Due to the comparison with other researchers, including the results of their own tests, these peak frequency values are most reliable and will therefore be used as a basis for this thesis.

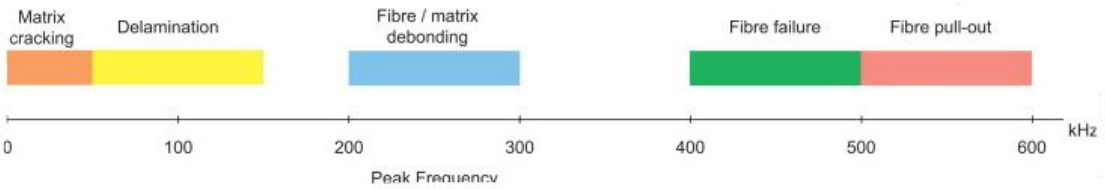

Figure 2.1: CFRP damage modes and their AE frequency spectrum schematically represented, taken from [17]

Guided waves

For SHM, both bulk waves and guided waves can be used. [18] The main difference between the two types of wave forms is that guided waves require boundary conditions and bulk waves do not. [18] Due to these boundary conditions and the possibility of damage being present, reflections of the waves propagate back into the structure. This allows for many different types of wave forms (wave mode, frequency, amplitude, velocity and the effect of dispersion), making the wave complicated to analyse, but allowing for the detection of very small sized damages (BVID). [11][18] These are damages that are only visible within 1,5 m from the impact zone, creating a damage of less than 1 inch in diameter in the composite structure. [19] The main advantages of guided waves for SHM are that the required transducers are (1) cheap, easy to attach to the structure, light-weight, able to monitor large areas, capable of detecting small damages by exciting high frequencies and damping has limited effect on the wave form. [20] Disadvantages that need to be taken into account are that the waves consists of multiple wave modes, are dispersive which changes the wave shape, are reflected by boundary conditions leading to reflections in the structure and are sensitive to environmental and operational factors such as noise. [20]

Upon interaction with damage, the guided waves will split into several different wave modes which are scattered in different directions, are susceptible for changes during their propagation through the structure, are reflected, are absorbed and operational conditions with the different environments can influence the guided waves. To overcome these difficulties, a good understanding of the different wave types is required. The most common wave modes are the Lamb waves and Rayleigh waves. Lamb waves propagate through thin plates with stress free boundary conditions, which are prerequisite. As aerospace structures most often have these stress free boundary conditions, using Lamb waves is a interesting method for aerospace SHM. Rayleigh waves are higher frequency waves, which propagate at the free surface of a thicker elastic (solid) plate. [20] Other wave modes are Love waves [21], Stoneley waves [21] and Scholte waves [22]. Love waves are shear horizontal wave modes which allow for the vertical motion of particles in the structure. Love waves are thus different, as this modes excites the particles in horizontal manner, also at the free surface. [23] Stonely waves are waves that travel at the interface of two media, exciting the vertical motion of the particles. [21] Scholte waves are waves

that travel at an interface of a fluid and solid medium. [22]

As stated above, Lamb waves are a form of guided waves. Normally Lamb waves are initiated by (piezoelectric) actuators, which provide well defined excitation of guided waves in the thin plate. This makes the signal analysis of the obtained signals more understandable. On the other hand, it has been shown in research [24][25] that out-of-plane impacts also initiate Lamb waves, of which the dominant wave mode is the anti-symmetric mode. This means that Lamb waves can also be used for SHM applications which require passive sensing, making Lamb waves the chosen wave type for this thesis.

Because the main objective of this thesis is focused on passive SHM methods using waves initiated by out-of-plane impact for damage detection, the Lamb wave method is further discussed in the section 2.2. It is possible to use of fibre optic sensors (FOS) and piezoelectric sensors for detecting Lamb waves in composite panels (also see section 2.3).

2.2. Lamb waves

As stated in the previous paragraph, Lamb waves are a form of guided waves. This type of wave has proven to be the dominant wave form in thin plate structures, of which aerospace panels are an example. [26] Due to the long distances (several meters [27]) the waves can propagate, low loss in signal response (attenuation), it being highly sensitive for small imperfections and damages in a structure, able to detect damage (size) and its location and it being able to be used for life time prediction of the structure, makes Lamb wave monitoring a suitable method for aerospace SHM. [26] The initiator of the wave within passive SHM is most often an external source or internal damage (acoustic emission). Due to the high potential of this wave form just discussed, it will be discussed in more detail below.

2.2.1. Fundamental of Lamb waves

Lamb waves are also known as plate waves, which are elastic waves in thin plates. [21] These waves are a superposition of the shear modes and longitudinal modes present. [21] A thin plate is defined as a body which has far greater planar dimensions compared to the thickness of the body. [21] The wavelength (λ) also has to be in the same order of size as the thickness (d) of this thin plate for this theory to be applicable, meaning that Lamb waves will occur for $\frac{d}{\lambda} \leq 1$. [9][21][23] Lamb waves exist in both symmetric and anti-symmetric modes. Figures 2.2 and 2.3 visualizes these modes.

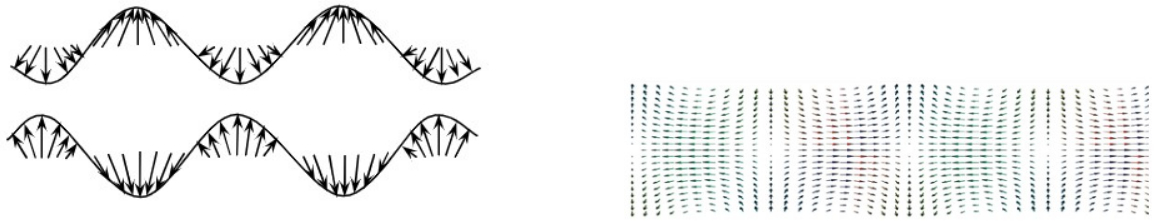

(a) Symmetric Lamb wave mode [21]

(b) Symmetric Lamb wave mode model [28]

Figure 2.2: Symmetric Lamb mode representations

(a) Anti-symmetric Lamb wave mode [21]

(b) Anti-symmetric Lamb wave mode model [28]

Figure 2.3: Anti-symmetric Lamb mode representations

Taking a thin plate with homogeneous and isotropic characteristics into account (Figure 2.4), the generic Lamb waves can be described by the Cartesian tensor [21]

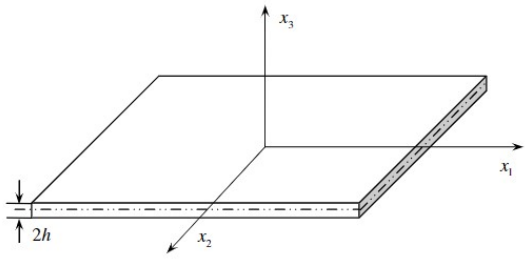

Figure 2.4: Thin plate with the coordinate system and thickness $2h$, taken from [21]

$$\mu \cdot u_{i,jj} + (\lambda + \mu) \cdot u_{j,ji} + \rho \cdot f_i = \rho \cdot \ddot{u}_i \qquad \text{(i,j = 1, 2, 3),} \tag{2.1}$$

in which u_i is the displacement force in direction x_i, f_i is the body force in direction x_i, ρ is the density, μ is the shear modulus and λ is the Lamé constant. Using the Helmholtz decomposition, the displacement fields, stresses and strains can be derived. Thus, the symmetric and anti-symmetric modes can be described by means of the symmetric (S) and anti-symmetric (A) Lamb wave equations in isotropic and homogeneous thin plates as

$$\frac{tan(qh)}{tan(ph)} = -\frac{4k^2qp}{(k^2-q^2)^2} \qquad \text{Symmetric modes} \tag{2.2}$$

$$\frac{tan(qh)}{tan(ph)} = -\frac{(k^2-q^2)^2}{4k^2qp} \qquad \text{Anti-symmetric modes} \tag{2.3}$$

in which ω is the frequency in angular direction, k the wave number defined as $k = \frac{\omega}{c_p}$, h half the thickness of the plate, $p^2 = (\frac{\omega^2}{c_L^2} - k^2)$, $q^2 = (\frac{\omega^2}{c_T^2} - k^2)$, c_L the longitudinal mode velocity and c_T the transverse/shear mode velocity. From hereon, the symmetric modes are described as S_i and the anti-symmetric modes as A_i for $i = 0, 1, 2, \ldots$. [21] The propagation velocity of these waves are characterized by the phase velocity c_p and the group velocity $c_g(f \cdot d)$. The phase velocity is defined as the speed of a wave phase, of which the overall wave contains a specific frequency, to which the wavelength is linked. It is described as

$$c_p = \frac{\omega}{2\pi} \cdot \lambda_{wave} \tag{2.4}$$

in which λ_{wave} is the wavelength. [21] The group velocity is the speed of the overall amplitudes of the multiple waves in different layers and is dependent on the wave frequency and the plate thickness and is described as

$$c_g(f \cdot d) = \frac{c_p^2}{c_p - (f \cdot d)\frac{dc_p}{d(f \cdot d)}} \tag{2.5}$$

in which d is the thickness of the plate and f is the central frequency defined as $f = \frac{\omega}{2\pi}$. [21]

These equations describe the relationship between the frequency, group velocity and phase velocity while taking the thickness of the plate into account. By numerically solving these equations at different frequencies, an infinite amount of wave numbers can be solved for different frequencies. As k is linked to the wave number, the values of c_p and $c_g(f \cdot d)$ can also be determined. [21] The typical form of the dispersion curves for symmetric and anti-symmetric wave modes in an aluminium plate is shown in

Figure 2.5. The ratio of the thickness and the wavelength determines the stiffness of the plate and thus the wave velocity. This Figure shows that the dominant wave modes are the S_0 and A_0 modes in low frequency ranges and that the waves are dispersive (meaning that the wave velocities are dependent on the frequency). When increasing the frequency-thickness, other wave modes will be present in the plates. For application of a proper Lamb wave mode, one must take into account that there is no dispersion, there is no to minimal attenuation of the signal, the system is highly sensitive, the signal is easy to excite through the structure, the signal is easy to detect and the mode must be easy to select. [23] To overcome dispersion of the signal, it is advised to use narrow bandwidth signals in which toneburst is used, instead of pulse signals. [23] As S_0 and A_0 modes are most often used, A_0 modes are increasingly used in applications as the short wavelength is beneficial for effectively detecting delaminations and transverse ply cracks. [23]

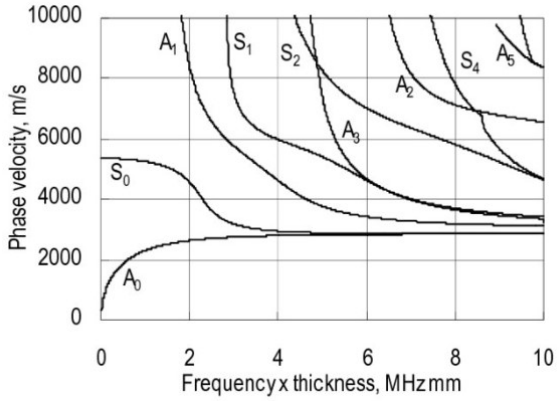

Figure 2.5: Typical form of Lamb wave velocity dispersion curves in a 1 mm thick aluminum plate, taken from [25]

As most composite plates consist of multiple layers (and are thus anisotropic if the layers are in different directions), not only the wave propagation in individual layers contribute to the wave forms, but also the interaction of the interfaces needs to be taken into account. The anisotropic characteristics of multilayered composites lead to a change of Equation 2.1 to

$$\mu^n \nabla^2 u^n + (\lambda^n + \mu^n)\nabla(\nabla \cdot u^n) = \rho^n \frac{\partial^2 u^n}{\partial t^2} \qquad \text{(n = 1, 2, ..., N)}, \tag{2.6}$$

in which all the layers of a N-layered plate satisfy the Navier displacement equation in displacement field u for n layers. $\nabla = \frac{\partial}{\partial x_1} + \frac{\partial}{\partial x_2} + \frac{\partial}{\partial x_2}$, $\nabla^2 = \frac{\partial^2}{\partial x_1^2} + \frac{\partial^2}{\partial x_2^2} + \frac{\partial^2}{\partial x_3^2}$, λ^n (Lamé constant) and μ^n are material properties. [21]

Because multilayered laminates most often consist of layers with different fibre orientations, the dispersion curves will be different compared to the typical curves shown in Figure 2.5. Due to these different fibre orientations, the Lamb waves will exhibit different propagation properties and directions in the different layers, changing the waves mode velocities. This is related to the slowness and dispersion, of which more will be described below. Multilayered composites which are assumed to have free upper and lower surfaces, introduce four constants C_1^n to C_4^n with $n = (1, 2, \ldots, N)$ within Equation 2.6. This leads to in total $4N$ equations, in which the boundary conditions and continuity conditions have been taken into account. These conditions are stated as the normal and transverse traction, the displacement of the $N-1$ interfaces between two layers and that the upper and lower free surfaces are ensured. When relating the frequency and the wave number to the thickness of the individual layer n and the material properties λ^n and μ^n, the dispersion curves of multilayered composites can be calculated by [21]

$$\begin{bmatrix} A_{11} & A_{12} & \cdots & A_{1(4N)} \\ A_{21} & A_{22} & \cdots & A_{2(4N)} \\ \vdots & \vdots & \ddots & \vdots \\ A_{(4N)1} & A_{(4N)2} & \cdots & A_{(4N)(4N)} \end{bmatrix} \begin{bmatrix} C_1^1 \\ C_2^1 \\ \vdots \\ C_4^N \end{bmatrix} = \begin{bmatrix} 0 \\ 0 \\ \vdots \\ 0 \end{bmatrix}. \tag{2.7}$$

In Equation 2.7, $[A]$ defines the coefficient matrix, which has to be zero for the equation to be generally applicable. This leads to

$$| A(\omega, k, \lambda^n, \mu^n, d_n) | = 0. \tag{2.8}$$

Lamb waves can be actively generated by means of ultrasonic probes, piezoelectric elements, laser based ultrasonics and interdigital transducers. [21][23] Using these methods, the exact frequency for the initiated waves can be chosen. Besides these active Lamb wave excitation in structures, Sultan et al. [24] and Miesen et al. [25] proved that out-of-plane impact also lead to Lamb wave propagation through structures, allowing for passive SHM application, relevant for this thesis. When out-of-plane impacts are the cause of guided waves, the frequency cannot be chosen, making analysis harder compared to the previous described active generation methods.

2.2.2. Signal processing of Lamb waves

When signal processing Lamb waves, it is important to consider some factors that are inextricably linked to the waves. Slowness, attenuation and temperature influences are relevant to take into account upon processing of the Lamb wave signals. [21] When looking at damage, one must take the sensor placement and size of the sensor into account to detect the signal. [23] Further, different numerical, semi-analytical, frequency and time domain methods can be used for signal processing. [21][23]

Slowness is the discrepancy of the Lamb wave velocity in different directions in the composite laminate. In isotropic materials or composite plates, the wave velocity is omnidirectional, meaning that the waves propagate with the same speed in all directions. Within anisotropic materials, this is not the case. [21] Waves will travel at different velocities, meaning that the wave is dependent on the direction of propagation (e.g. by fibre directions). In Table 2.1 the calculated and measured phase and group velocities for carbon fibre laminates are represented. Figure 2.6 represents the slowness profile of a typical CF/EP laminate in regard to the $0°$ fibre direction. Here can be seen that the lower order Lamb wave modes are clearly dependent on the laminate orientations (fibre direction). This dependency decreases with quasi-isotropic laminates. This can be of interest for aerospace applications, as quasi-isotropic laminates could potentially be simplified as isotropic materials. [21]

Table 2.1: Measured and calculated phase and group velocity of different laminate lay-ups

Laminate layout	Prop. Direc.	Phase velocity [km/s] (at 1 MHz)		Group velocity [km/s] (at 0.8 MHz)		
		Cal. S_0	Cal. A_0	Cal. S_0	Meas. S_0	Meas. A_0
$[0]_8$ (8-ply)	0	10.3	1.9	10.25	9.9±0.7	1.7±0.1
	±45	7.4	1.6			
	90	2.2	1.3		2.9±0.2	1.4±0.1
$[0/90]_{2s}$ (8-ply)	0	7.1	1.6	6.77	6.8±0.3	1.6±0.1
	±45	5.5	1.5		5.3±0.2	1.6±0.1
	90	7.3	1.5		6.9±0.3	1.5±0.1
$[\pm45/0/90]_s$ (8-ply)	0	6.5	1.5	6.27	6.1±0.2	1.6±0.1
	±45	6.5	1.5		5.9±0.2	1.6±0.1
	90	6.3	1.5		6.0±0.2	1.5±0.1
$[0/90]_{4s}$ (16-ply)	0	2.1	1.6	6.67	6.8±0.3 *	1.6±0.1
	±45	1.9	1.6		5.1±0.2 *	1.7±0.1
	90	1.9	1.6		6.9±0.3 *	1.6±0.1
$[\pm45/0/90]_{2s}$ (16-ply)	0	1.9	1.6	6.07	6.0±0.2 *	1.6±0.1
	±45	2.0	1.6		6.0±0.2 *	1.6±0.1
	90	1.9	1.6		6.1±0.2 *	1.6±0.1

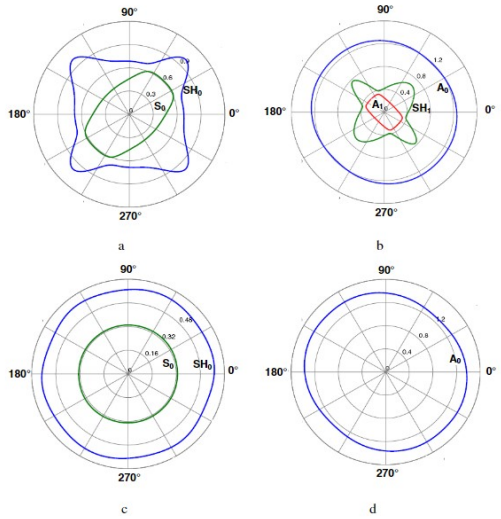

Figure 2.6: Typical slowness profiles of isotropic (c)(d) and anisotropic (a)(b) laminates

Attenuation of Lamb waves occurs upon propagation through the structure by means of geometric barriers or material properties. [29] The energy of the wave dissipates with the distance it travels, resulting in a decrease in the magnitude of the signal. [21] Geometric factors such as the presence of stiffeners, fasteners, beams, step thickness and damage and material factors such as material properties and thickness deviation (not being step thickness), contribute to attenuation of the Lamb wave through a structure. [21][29] Table 2.2 represents the attenuation coefficient for different materials, Lamb wave modes and excitation frequencies. This Figure shows that one must take this into account when applying Lamb wave based SHM on larger structures. Two key points can be derived from the table, being that (1) Lamb waves tend to travel further in carbon fibre reinforced polymers (CFRP) than in glass fibre reinforced polymers (GFRP) and that (2) symmetric Lamb waves travel farther than the anti-symmetric wave modes. [21] The higher attenuation of the anti-symmetric wave mode can be linked to the more dominant out-of-plane movement of the particles compared to the symmetric wave mode. This leads to energy loss to the environment. The rate of Lamb wave amplitude attenuation in a plate, measured at two locations along the propagation path, decays proportionally to the inverse square root of the propagated distance, described as

$$\frac{A(d_1)}{A(d_2)} = \frac{\sqrt{d_2}}{\sqrt{d_1}}, \tag{2.9}$$

in which A is the Lamb wave magnitude, d_1 the distance of the first sensor and d_2 the distance of the second sensor from the actuator. The attenuation can be compensated by means of correcting the wave amplitude due to beam spreading, described as

$$f^*(t) = f(t)\sqrt{t} \tag{2.10}$$

in which $f^*(t)$ is the compensated frequency, $f(t)$ is the original measured signal and t is the travelling time of the signal through the structure. [21] This method does not take scaling factors of material properties into account, but can appropriately be used for compensation. [21]

Ambient temperature changes also have influence on Lamb wave propagation. Both the signal travel distance and the magnitude of the Lamb waves increase upon higher temperatures of the structure. [21] The central frequency of the signal also tends to shift upon ambient temperature changes. [21] This is not only due to material property changes in the structure that is measured, but also on the transducers and sensors that are placed on that structure. Different coefficients of thermal expansion (CTE) also contribute to altering Lamb wave signals. [21] When the ambient temperature variation is minimized upon measuring (within 25°C), there is no need to compensate for the signal. One must take into account that these temperature changes have more effect upon measuring small damages,

Table 2.2: Examples of attenuation coefficients of different materials and wave modes, taken from [21]

Composite layouts	Lamb mode	Excitation frequency [kHz]	Attenuation coefficient [mm^{-1}]	Distance until decay to 10% [mm]
CFRP woven (8-ply)	S_0	250	0.0014	1700
CFRP woven (10-ply)	A_0	285	0.027	85
CFRP woven 10-ply with T-stringers *	S_0 (∥)	250	0.00078	3000
	S_0 (⊥)	250	0.0016	1500
GFRP random	S_0	220	0.0035	660
CFRP/GFRP hybrid sandwich foam core	S_0	250	0.013	182
CFRP/GFRP hybrid sandwich honeycomb core	S_0	250	0.0036	640
	S_0	150	0.0015	1600
GFRP filament wound pipe	S_0	250	0.015	150
	S_0	150	0.011	210

when the measurements take place in elevated ambient temperatures and when the signal modulation is sensitive to changes in ambient temperature. A simple method to compensate for the temperature using a linear inter- or extrapolation method by calculating the compensated signal $f_T(t)$ is

$$f_T(t) = \frac{T - T_1}{T - T_2}(f_{T2}(t) - f_{T1}(t)) + f_{T1}(t), \tag{2.11}$$

in which T is the temperature, $f_{T1}(t)$ and $f_{T2}(t)$ the sensor signals from the same sensors in different temperatures. [21]

For damage detection the difference between the phase and/or group velocity and the amplitude indicate a change in the stiffness of the material. This is an indication of damage being present in a specimen. [30] Upon wave interaction at the structural damage, unique scattering patterns - dependent on the type of damage - can be distinguished. When the excited waves interact with a through-the-thickness hole, the waves creep around the damage, leading to omni-directional scattering of the Lamb waves. Due to this phenomena, sensor location is less of importance. When the excited waves interfere with a crack, notch or a sufficiently sized damage in length, it leads to a directional change in Lamb wave direction. Good sensor positioning is required for sensing these damages, as the positioned sensors may not effectively pick-up the scattered signals. [23] Thus, upon interaction with the damage, the guided Lamb wave scatters through the specimen. The interaction leads to an additional (secondary) wave, which can be diffuse and is in most cases different in phase to the primary wave. The behavior of this scattered wave is dependent on for instance the frequency of the incidence wave, angle of incidence of the wave with the damage and the Lamb wave mode. Also mode conversion can take place, in which the wave mode of the scattered wave is different from the primary Lamb wave. Delaminated regions in composite materials show multiple reflections, of which the energy is trapped below and above the delaminated area. [31] These reflections are present until all the energy of the wave is dissipated. When the guided wave enters the delaminated region, the primary wave will be split into the top and bottom layer and propagates through these layers respectively. The reflections, existing from the boundary conditions of the specimen, will pass back through the damaged region until the energy is fully dissipated. Due to the layers having different thicknesses compared to the pristine lay-up, the waves will have different characteristics which can be analysed. This method (trapped in- and out-of-plane waves) has been further researched in a quantitative manner in [31].

Multilayered laminates are harder to process and analyse than isotropic materials. [21][30] When solving the isotropic dispersion Equations 2.2 and 2.3, there are an infinite amount of wave numbers k that can be solved (analytically but also numerically), real or imaginary. But when a higher-order equation is used, which is a non-algebraic function, it may not be solved analytically. This means

that for isotropic materials a numerical method is used to solve them. For multiple layer anisotropic laminates, the latter always requires a numerical method to solve the equations and find the dispersion curves. In the basis there are two main numerical methods that can be used. These methods are the transfer matrix method (TMM) and the global matrix method (GMM), but will not be discussed in detail. [21][30]

Processing and feature extraction methods are broadly available from descriptions in research papers. This paragraph will provide an overview of the different methods, each consisting of different accuracy and precision characteristics relevant for (passive) damage detection and identification systems. Yet, all the to be discussed methods are expected to efficiently and correctly extract all relevant information from the captured signal (Lamb wave). These methods are most often digital, meaning only digital signal processing methods will be discussed. The different feature extraction and processing methods can be grouped in four main topics, being time domain analysis (TDA), frequency domain analysis (FDA), time-frequency domain analysis (TFDA) and the wavelet transform (WT). All these methods are described in more detail in in [21] and [23]. For this thesis, the TFDA and WT will be used during the analysis. Due to the large amount of theory, these processing methods will be discussed in a separate Section 2.4.

When processing Lamb wave signals, one must take into account that the signals may be altered due to contaminations such as mechanical noise and fluctuation in temperature/humidity, damage signals are sensitive to external vibrations during measuring (active SHM), presence of multiple Lamb wave modes (as discussed in Section 2.2.1) and a vast amounts of data due to the high sampling rates (kHz/MHz range). [21] By applying averaging and normalisation, de-noising, damage index and feature extraction and compression steps during the signal processing, allows for good data results as discussed in more detail in [21]. It is important to keep in mind that vibrations from noise cannot be fully eliminated during SHM, as shown in recent research by Ochoa et al. [32], in which machinery and high-amplitude low-frequency vibrations are monitored on a composite aircraft structure.

2.3. Passive SHM sensor types

For structural health monitoring, many sensors can be used. Each sensor has its own benefits and restrictions regarding SHM information gathering during the service life of the structure. This section will describe the potential and shortcomings of the two types of sensors that are used for this thesis. These sensors are piezoelectric sensors and fibre optic sensors (FOS). First the main sensor specifications, required for accurate SHM in aerospace structures, will be discussed. With this knowledge, the sensor types will be reviewed and compared to the required specifications to get a good understanding of the capabilities of these sensors. Finally, in the conclusion, a table will be presented to give a good overview and capabilities of the different sensors.

2.3.1. Sensor characteristics for SHM

It is important to use capable sensors for aerospace SHM for its intended application, as each different type of sensor has its own strengths and weaknesses. To choose the right type of sensor, fundamental specifications have been characterized for damage detection SHM applications. As stated in the comprehensive SHM review of Hassani et al. [12], the type and amount of sensors, the costs of the system, installation procedures, in service damage protection and the way data is collected and is able to be analysed are important factors for sensor and system selection. As this thesis will research an impact damage detection and quantification application, a good knowledge of restrictions and possibilities of sensors is prerequisite. These sensor specifications are shown in Table 2.3 and will be the basis for sensor evaluation in this section.

The sensors that are described in the following paragraphs, will be compared to the characteristics from Table 2.3.

2.3.2. Piezoelectric transducers

Piezoelectric transducers can be both used for actuation and sensing of waves through a (composite) specimen. [33] When actuating, the probe is connected to a power supply allowing for the piezoelectric

Table 2.3: Sensor characteristics for damage detection in composite structures, taken from [12]

Specifications	Description
Range	The variation in measurements is limited between a minimum and maximum value, termed the range of a sensor
Sensitivity	The sensors should be sensitive enough to the response of a system to the applied load
Accuracy	The value shown by a sensor might be slightly off by a factor, whereby the accuracy of the sensor can be characterised
Stability	The durability of sensors for long-term condition monitoring of structure
Repeatability	The measurement made by the sensor on the structure subjected to the same load should not vary much from the previous measurements
Energy Harvesting	Energy harvesting capability of sensors is essential for sensors used for long–term condition of structures
Compensation due to change in temperature and other environmental parameters	The signal conditioning feature of the sensors should be capable of reducing the environmental variations effects

element to be actuated in a controlled way. This actuation, which is able to be done in different frequency ranges (kHz and MHz), allows for Lamb wave generation in the structure. When the probe is sensing, the Lamb wave actuates the probe, producing a current change. This current is changed into an electrical potential difference by a charge-to-voltage amplifier, which is used as measuring variable. Because this thesis focuses on passive SHM, only the sensing mode will be described in this section.

Piezoelectric sensors, for instance piezoelectric wafer active sensors (PWAS) , are ideal sensors for repeatedly measuring low and high frequency Lamb waves or acoustic emission (AE) vibration in structures. [10] The output voltage is proportional to the strain rate that the sensor endures, making it an ideal sensor for high frequency measurements. Because PWAS have a charge leakage, they are less accurate at low frequencies, but still useable during quasi-static measurements. [33] These transducers are mostly made of piezoceramics, -composites or -polymers. The most common and well known sensor for passive SHM in aerospace structures is made of a piezoceramic material called lead zirconate titanate (PZT). Due to the poled PZT ceramic, a voltage is created upon mechanical loading (e.g. compression and tension) due to the change in dipole moment, also known as the direct piezoelectric effect. In Figure 2.7 the direct piezoelectric effect is schematically represented, by a voltage measurement by changing the dimensions of the ceramic material. Both in compression and tension the output voltage is the same, but change in sign. [34][35].

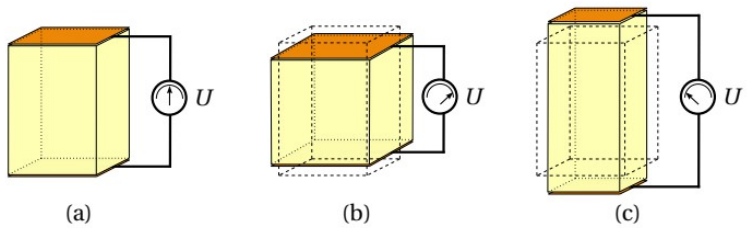

Figure 2.7: Direct piezoelectric effect on a specimen undergoing shape deformation in neutral position (a), out-of-plane stress (b) and in-plane strain (c), taken from [35]

It is important to understand that, to increase the sensor sensitivity, the thickness, Young's Modulus or the piezoelectric voltage constant can be increased. [35] The piezoelectric voltage constant is related to the piezoelectric charge constant and the dielectric constant. The piezoelectric charge constant is dependent on the material and geometry. The dielectric constant is a sensor parameter, given in the sensor data sheet. The higher the piezoelectric voltage constant, the more sensitive (up to 5 $V/\mu\varepsilon$ [36])

the sensor will be [35]. PZTs are able to measure up to 6000 $\mu\varepsilon$ with a durability up to $12{\cdot}10^6$ cycles. [37] One must take into account that increasing the thickness or the Young's Modulus will affect the guided waves near the sensor as the sensor will affect the signal. Therefore, for optimal guided wave sensing, thin sensors with a low Young's Modulus are advised, even though thicker sensors are more sensitive than thinner sensors. [33] A compromise of sensor readability and interference of the guided waves per application thus has to made. [38] Brittleness and poor conformability of the PZT sensors is also to be considered for handling purpose and its application. [34]

Because PZT sensors are well known and understood for passive SHM applications, this sensor will also be used during the experimental phase of the thesis.

2.3.3. Fibre optic sensors

Fibre optic sensors (FOS) in general have gained increased interest in the aerospace SHM research field due to their immunity to electromagnetic interference (EMI) , insensitivity of corrosion, possibility of multiple FOS in one optical fibre (multiplexing), possibility of direct embedment in the composite matrix, light weight and small dimensions. [39] Besides these many advantages, FOS require advanced data acquisition equipment for translation to physical and understandable readings, of which the bandwidth of the equipment is nowadays the limiting factor for FOS applications. [39] Fibre optics can be divided into three main sensor types, namely interferometric sensors, grating-based sensors and distributed sensors, which are represented schematically in Figure 2.8. As interferometric sensors have low multiplexing capabilities and distributed sensors have many uncertainties in the area of interest, fibre Bragg grating sensors will be the choice of sensor for this thesis. This choice will be further clarified in this paragraph.

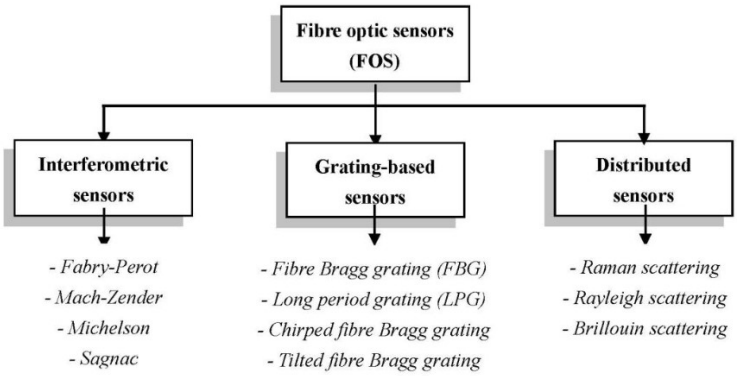

Figure 2.8: Schematic of fibre optic sensors and their working principles, taken from [40]

Interferometric sensors base their measurements on the phase shift of two similar wavelength light waves. These sensors are able to achieve a high resolution ($\mu\varepsilon$) and have a high range (up to 5000 $\mu\varepsilon$). [40] However, the low multiplexing capability of this sensor makes this sensor unpopular for aerospace SHM. [40]

When using distributed sensors, based on the Rayleigh and/or Brillouin scattering principle for strain measurements, the optical fibre itself is used as sensor. Changes in the scattered light characteristics, excited by temperature changes or vibrations in the structure, are measured. [40] Current systems provide a spatial resolution between the 2 and 10 cm, with respectively an accuracy of 4 to 15 $\mu\varepsilon$. Their strain range is promising with approximately ranges of $10.000\mu\varepsilon$. Although this technique is promising regarding range and sensitivity, for aerospace SHM principles the processing equipment requires large bandwidths and the measurements are prone to many uncertainties at the area of interest. [40]

The last type of sensor, is the grating based sensor, of which the fibre Bragg grating (FBG) sensors have already been extensively explored in the aerospace SHM research field. As shown in Figure 2.9, over a short segment in the fibre the refractive index is modified to give equally spaced reflectors called Bragg

gratings, within a certain periodic refractive index n_{eff}. The spacing between these indexes is called the Bragg grating period (Λ_B). The grating spacing determines which wavelength (λ_B) is reflected, according to

$$\lambda_B = 2n_{eff}\Lambda_B. \tag{2.12}$$

This means that upon introducing a light wave as input - containing a small spectrum of wavelengths - in a single mode optical fibre, the light wave travelling with the Bragg wavelength λ_B will be reflected by the gratings. The rest of the light wave spectrum is further transmitted through the fibre, where it may be used for sensing at later FBGs.

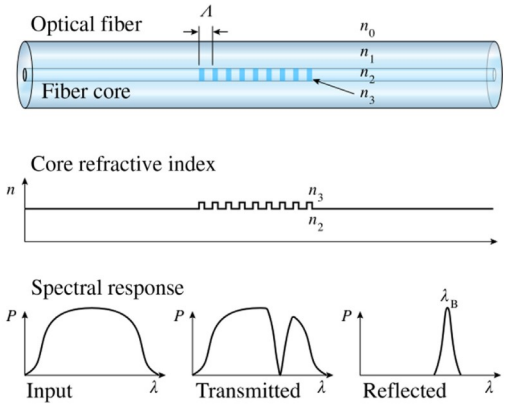

Figure 2.9: Fibre Bragg grating (FBG) working principle, in which λ_B is the wavelength, Λ is the Bragg grating period, n_{eff} is the refractive index for $_{eff} = 1, 2, \ldots$ and P is the spectral response, taken from [41].

Due to the working principle of FBG sensors, they can be used for (Lamb wave-induced) strain and temperature measurements. Both excitation methods change the dimensions of the Bragg gratings, leading to a shift of the reflected wavelength. These changes in wavelengths are correlated to an amount of local deformation, as the grating period in the FBG changes correspondingly. Strain can be thus detected according to

$$\frac{\Delta\Lambda_B}{\Lambda_B} = (1 - p_e)\varepsilon + (\alpha_\Lambda + \alpha_n)\Delta T \tag{2.13}$$

in which p_e is the strain optical coefficient, ε the local strain sensed by the FBG sensor, α_Λ the thermal expansion coefficient, α_n the thermo-optic coefficient (coefficient describing the change in shape and refractive index upon changing the temperature) and ΔT the temperature change. When the FBG is bonded to or embedded in a composite structure, one must also take the CTE of the structure into account as represented in

$$\frac{\Delta\Lambda_B}{\Lambda_B} = (1 - p_e)\varepsilon + (\alpha_\Lambda + \alpha_n + (1 - p_e)(\alpha_{struc} - \alpha))\Delta T \tag{2.14}$$

in which α_{struc} is the CTE of the tested material. [42]

Due to the sensitivity of the sensor over the entire Bragg grating length, microscopic deformations due to strain or temperature can be measured, making it a high sensitive measuring method with typical strain sensitivities of 1 $\mu\varepsilon$, a temperature sensitivity of up to 0.1°C and a life cycle of approximately $10 \cdot 10^6$ cycles and/or a max elongation of approximately 25.000 $\mu\varepsilon$ ([43]). It is important to consider that FBG sensors are capable of sensing Lamb waves, only if the grating length is smaller than the propagating wave. [40] If not taken into account, the signal will be equivocal and interrogation of the signal will be more difficult or even impossible eventually leading to unusable measurements. Also, any damage in the fibre or in the FBG itself influences the entire SHM system when multiplexed. The above described principles and sensors are discussed more extensively in [39], [41] and [40].

One of the advantages of a FBG sensor is that the sensors can be multiplexed on one optical fibre, meaning that multiple FBG sensors can be placed in one optical fibre. When a (broadband) wavelength light signal is emitted in the fibre, the different FBGs will reflect a different spectrum (dependent on the local strains and the grating of the individual sensor). [23] This method is called wavelength division multiplexing (WDM) . A second method is when FBGs with the same refractive index are multiplexed in a single fibre and the reflection of the FBG can be determined by the time difference between reflections. The further away the FBG is from the interrogator, the longer it takes for the reflection to arrive, allowing for the distinction of the signals. This method is called time division multiplexing (TDM) . [44]

The length of an FBG also has effect on the strain measurements done on a structure. As stated above, the length of the grating in the FBG must be smaller than the wavelength to be detected. Besides this necessity, the length of the FBG is also important to consider. Tahir et al. [45] have proven that, independent of the length of the FBG, under the similar increase in strain and at the same temperature (as FBGs are sensitive to temperature changes), the sensors have a linear wavelength shift $\Delta\Lambda_B$ (Equation 2.13). They also concluded that the sensitivity increases when decreasing the sensor length. With smaller FBGs, higher wavelength shifts can be detected, thus meaning the sensor is more sensitive. Directivity also has influence on the sensor response signal, as the grating in the FBG does not collect the Lamb wave signals omnidirectionally as PZT sensors do. Placing a FBG sensor parallel to the propagating wave, makes the magnitude of both the S_0 and A_0 wave modes 100x greater than placing them perpendicular to the propagation direction. Ideally, placing the FBG sensor parallel to the wave propagation direction, gives the best signal response. However, damages in the material at the unknown location of an impact, bring challenges for optimal FBG placement. Placing the FBGs in a rosette configuration as shown in Figure 2.10, meaning that the FBGs are placed 120° with respect to each other and trigonometry can be applied to define the wave propagation direction. [21]

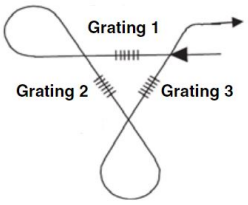

Figure 2.10: Rosette configuration of FBG sensors, taken from [21]

Upon measuring, birefringence can occur. Birefringence is a split or parting phenomena occurring in the response signal of a FBG sensor, making it harder for signal processing. Figure 2.11 shows a typical response of a FBG sensor which is disturbed (split), in this case of plain stress, compared to a pristine undisturbed sensor. This occurs for both low reflective and high reflective FBG sensors, when subjected to transverse and/or linearly distributed load on the FBG. To minimize the effect of birefringence when measuring strain or temperature, a well applied coating on the fibre, especially on the FBG part, is required. [46]

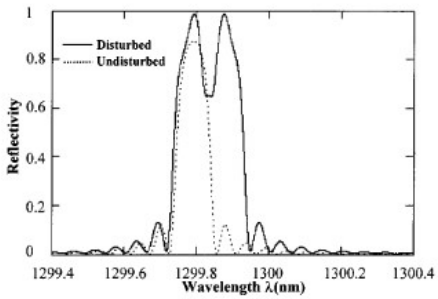

Figure 2.11: Example of a birefringence signal response of a FBG sensor, taken from [46]

The signal reflection can also be affected due to manufacturing methods. Primarily, FBGs are manufactured by three main techniques, namely direct laser writing [47], draw tower [47] and strip and recoating [48] methods. The direct laser writing method uses the femtosecond laser technique, which emits optical pulses in the femtosecond (10^{-15}) domain. The laser is focused on the core of the optical fibre for FBG encryption, without damaging the coating or the cladding. As stripping and recoating of the fibre is not required, these fibres tend to be the strongest type of fiber in tensile strength and have a light reflectivity of $\geq 50\%$. [47] The draw tower method allows for integrating fibre extraction and FBG writing - by means of an UV-light interference pattern, in one process - gaining signal reflectivity of $\geq 15\%$. [47] Stripping and recoating of the fibre ensures precise FBG writing with a phase mask and an UV-laser, gaing a signal reflectivity of $\geq 80\%$. [48]. Both the draw tower and recoating fabrication methods require recoating of the fibre, affecting the fibre strength properties. [49] When measuring strains or temperatures with FBG sensors, Angled Physical Contact (APC) fibre connectors are typically used. These connectors have a polished angle of $5°$ to $15°$, minimizing back reflections which can alter the signal response. [50]

FBG Interrogation methods

The signals that the different optical sensors produce, also need to be interrogated, meaning that the obtained reflections will be measured within a certain frequency range. The higher the frequency of the interrogator, the more reflections can be taken into account in the final analysis. There are two main methods to interrogate FBG signals. The first method is measure the reflection spectra with a spectrometer, characterizing the peaks of each sensor in the fibre. The second method is to measure the reflected wavelength band at the photo-detector while scanning through different wavelengths. This can be done in either the time or frequency domain. Interrogation can thus be done by a conventional spectrometer [51], optical spectrum analysers, arrayed waveguide gratings [52], the edge filter technique [52], the twin-FBG technique [52] and the tunable laser approach [52]. For this thesis, a state-of-the-art AWG FBG interrogation system will be used. Therefore, this interrogating principle will be discussed in further detail.

Optical spectrum analyzers (OSA) and arrayed waveguide gratings (AWG) are used to demodulate the reflected spectrum of the FBGs in the fibre and their working principle is similar to that of the typical spectrometer. [52] Both methods make use of a broadband light source from an amplified spontaneous emission (ASE) or superluminescent light-emitting diode (SLED). Both the SLED and the ASE light sources illuminate the C-band (1530 - 1565 nm wavelength [53]), which allows for signal propagation to all FBGs in the fibre connected to one output connector. The OSA and AWG demodulation techniques are very similar, as shown schematically in Figure 2.12. The FBGs in the fibre reflect certain wavelengths from the emitted light source, which are sent to the OSA or AWG. Due to the need of only a broadband light source and an optical fibre with FBGs, the demodulation by an OSA is an easier method for FBG signal analysis compared to AWG. The AWG method requires an additional display to project the demodulated signal, where OSA has an integrated display. Furthermore the OSA demodulation technique is expensive, is heavy, is sensitive to damage, has a resolution of about $50pm$ (dependent on the model), does not provide accurate peak detection (due to limited software capabilities), is limited to static strain measurements [52] and has a low interrogation frequency [54]. These disadvantages make this method undesirable for real-time SHM in aerospace applications. In contrast to OSA, AWG hardware (based on a scanning filter or laser [54]) is commercially available and can be used as stand-alone equipment which is less fragile due to lacking of mechanical parts. The internal spectrometer is used for WDM, splitting the wavelengths of the FBGs as a diffractometer and projecting them on a diode array with a high resolution (approximately $2pm$), low noise and high efficiency. Therefore they do allow for strain, temperature and pressure measurements but also at high costs. [52] This method also has a higher scanning frequency than OSAs. [54]

2.4. Time, frequency and time-frequency domain analysis methods

2.4.1. Signal filtering

A simple method to analyse (parts of) signals in both the time and the frequency domain is by applying filters. In the time domain, filtering of the signal is also referred to as convolution of the input signal with the impulse response filter. When filtering in the frequency domain, the operation is based on

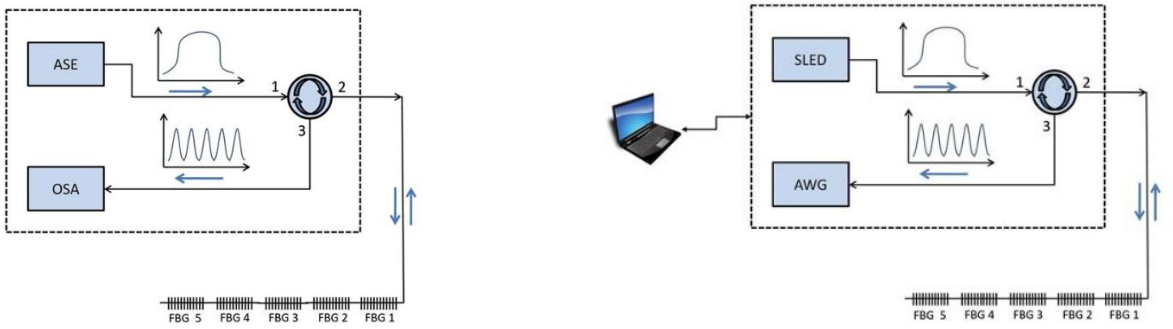

(a) Schematic representation of an optical spectrum analyzer (OSA) set-up.

(b) Schematic representation of an arrayed waveguide grating (AWG) set-up.

Figure 2.12: OSA and AWG demodulation techniques, taken from [52]

the multiplication of the input signal and impulse response filter, both transformed into the frequency domain by means of the Fourier transform. The goal of signal filtering is to remove or minimize unwanted signal responses such as noise, to better understand and analyse the signal. [55] The filters can be finite impulse response (FIR) or infinite impulse response (IIR) filters. The differences between the filters are that FIR filters have a finite duration, meaning that the filter returns to zero after a given moment in time. An IIR filter is infinite, meaning that the filter will return to nearly zero in time. Other differences between FIR and IIR filters are that FIR filters can be exactly linear in phase and they are stable (a bounded input returns a bounded output). [56][57] IIR filters are always recursive, meaning that the output depends on previous inputs, current inputs and previous outputs (feedback). FIR filters are always non-recursive, meaning that the current output is independent on any previous outputs. [55] Typically, FIR filters are of higher order than IIR filters when a certain performance wants to be achieved. Applying these filters to a signal, lower frequencies can be filtered out by applying a high-pass filter and higher frequencies can be filtered out by applying low-pass filters. When combining the two filters in one application, a pass-band or stop-band filter can be applied. A pass-band filter allows a certain (central) frequency range to not be filtered out, as where a stop-band filter eliminates frequencies within a defined frequency band. [55]

Another feature in signal filtering to take into account, is causality versus non-causality of the filters. Causal filters do not take future inputs of the signal into account. In other words, the causal filter does not respond to an input that is present in the future. Non-causal filters thus respond to input signals that occur in the future, which can be convenient for signal analysis. [55]

2.4.2. Fourier Transform Analysis

The Fourier transform (FT) is a 1D or 2D signal analysis method in the frequency domain. It shows signals that are global in time and local in frequency. The original signal $f(t)$ is continuously transformed to the frequency domain signal $\hat{f}(\omega)$ by

$$\hat{f}(\omega) = \int_{-\infty}^{\infty} f(t) e^{-i\omega t} dt, \tag{2.15}$$

in which ω is the frequency and t is the time. [58] Due to continuously transforming the signal, this method requires high computational cost and processing time, which can be a major disadvantage when much data needs to be analysed.

The Fast Fourier Transform (FFT) is a linear operation of which the goal is to decrease the computational cost and analysis time during the transformation to the frequency domain. This overcomes the shortcoming of the FT. Both the FT and FFT allow for the original signal to transform to a different domain by rotation in function space. The basis functions used in both transformations are sines and cosines, being relatively simple functions. [58] Due to the simplicity of these functions, the FT and FFT

methods are only suitable for stationary signal analysis and not for transient signals as they lack time resolution in picking up the transient features. [59] As impact events are most often transient - signals lasting for a short period of time - other methods have to be used. [58] Also, FT and FFT are only capable of extracting the frequency characteristics over the length of the entire signal. [60] To overcome some of these shortcomings, the short-time Fourier transform (STFT) can be used.

The Short-Time Fourier Transform Analysis (STFT) is a time-frequency domain analysis (TFDA) method in which the signal is also transformed to the frequency domain, but including in a shift/translation parameter u. The signal is transformed by sinusoidal basis functions within defined time windows. The STFT is defined as

$$\hat{f}(u,\omega) = \int_{-\infty}^{\infty} f(t)w^*(t-u)e^{-i\omega t}dt, \tag{2.16}$$

in which ω is the frequency, w is the selected time window and w^* is the complex conjugate (equal magnitude of the real and imaginary part) of w. [58] These additional factors allow for a windowed Fourier transform, which can be applied for multiple window sizes and translations. The wider the time window, the higher the frequency resolution but the lower the time precision. The chosen window can be overlapped. The more overlap of the signal, the higher resolution of the results, but the more computational time is required. The power spectrum of the STFT shows the power (also known as the amplitude) at each frequency level. By adding all the amplitudes of the different sinusoidal basis functions, the entire power of that frequency is shown in a single plot. Another method is to display the time and the frequency components of the signal, allowing for analyzing the frequency responses at certain time intervals of the signal. Although this method is better for signal analysis then the FT, the resolution of the transform is poor when the wavelength is longer than the window size chosen in equation 2.16 and the resolutions of the time and frequency is limited due to the Heisenberg inequality [61] (uncertainty principle, which is discussed further in the following section). Another downside of this method is that it is very poor in localizing the high frequency components of the signal [58], but does give a good initial indication of the frequency component deviations within certain frequency ranges. [62]

Overall, Fourier transformations have several limitations in signal analysis, consisting of the lack of localisation in space, requiring additional algorithms for increasing the transformation speed, the need for more flexibility, the lack of arbitrary domains, limitation of transforming signals which have an irregular sampling rate [58] and having a constant resolution [63]. Therefore, this method is not ideal for the real-time impact damage detection system, intended to be achieved within this thesis project. Despite the limitations of the STFT, it does offer decent indications of frequency components in signals. The wavelet transform overcomes many of the shortcomings of the STFT and will be discussed in detail in the next section.

2.5. The wavelet transform

The WT is a time-frequency domain resolving method capable of extracting features in both the time and frequency domain, while taking the Heisenberg inequality (uncertainty principle) into account. [63] The WT consists of orthogonal functions, translation and dilation functions, allowing the wavelet function to shift and expand in low and high frequency components within the time-frequency domain. [64] The WT also has the advantage that it does not require a baseline vibration database of the pristine structure, making this method suitable for real-time damage detection of composite structures. [65]

The WT allows for signal representation and analysis locally in the time and frequency domain. The idea of the WT is basically the same as that of the STFT, but when the signal frequency increases, the relative bandwidth is kept constant. This allows for an increase of resolution in time. For better understanding of the WT, it is necessary to describe what a wavelet is. A wavelet ψ is a function which satisfies two time domain conditions which are: (1) containing a small energy burst which is finite in time (making it little and localized) and (2) undergoing a oscillation in time, being dependent on the type of wavelet chosen (making it ”wavy”). [66] Orthogonality (generation of one scaling function and wavelet) and bi-orthogonality (generation of one scaling function and one wavelet, but also generating

a set for reconstruction of the signal) are important characteristics of the wavelet, as this allows for the easy decomposition of the original signal during analysis. [60] The basis function, also called the mother wavelet ψ, is the basis function for the WT analysis. This mother wavelet function must satisfy two conditions, the first of which is that the wavelet must have a zero average value in time t, as shown by [60]

$$\int_{-\infty}^{\infty} \psi(t)dt = 0. \tag{2.17}$$

The second condition is that the basis function must satisfy the condition that it is square integrable or has a finite value for the energy, represented as [60]

$$\int_{-\infty}^{\infty} |\ \psi(t)\ |^2\ dt < \infty. \tag{2.18}$$

The family of wavelets $\psi_{s,u}(t)$, is provided by dilation and translation of the mother wavelet and is represented as

$$\psi_{s,u}(t) = \frac{1}{\sqrt{s}}\psi(\frac{t-u}{s}), \tag{2.19}$$

in which s is the dilation factor ($s = 1/\omega$) and u is the translation factor. A wide window results in a low frequency wavelet, for analyzing low frequency signal components. This is achieved by choosing a scaling value of $s > 1$. When the high frequency parts of the signal need to be analysed, by means of a narrow window resulting in high frequency wavelets, a scaling value of $s < 1$ is required. [58][60]

2.5.1. Continuous wavelet transform

Now the basis of the wavelets is known, it can be further described for the 1D continuous wavelet transform $CWT(u,s)$. The CWT source function, capable of generating the daughter wavelets, is represented as

$$CWT(s,u) = \int_{-\infty}^{\infty} f(t)\frac{1}{\sqrt{s}}\psi^*(\frac{t-u}{s})dt, \tag{2.20}$$

in which s is the scale (allowing dilation), u is the translation factor and ψ^* is the complex conjugate of ψ. [58] The $1/\sqrt{s}$ allows for the wavelets on all scales to have the same energy and area. This equation allows for the original signal $f(t)$ to be convoluted with a translated and scaled basis wavelet. [58] The CWT coefficients contain all the values of the translated and dilated functions of the wavelet ψ. The time and frequency resolution of the CWT can be defined by means of the duration (Δt_ψ) and bandwidth ($\Delta\omega_\psi$) of the wavelet, being dependent on the dilation factor s. This relation is defined as

$$\Delta t = s\Delta t_\psi, \Delta\omega = \frac{\Delta\omega_\psi}{s}. \tag{2.21}$$

Equation 2.21 states that the resolution increases and decreases when the frequency respectively decreases and increases. This means that similar localisation accuracy in time and frequency is impossible. This relation is also referred to as the Heisenberg uncertainty principle, which is defined as $\Delta t\Delta f \geq \frac{1}{4\pi}$ [60][61]. The WT slightly overcomes the Heisenberg uncertainty as time and frequency are not fixed. Therefore, it allows to overcome the STFT shortcoming, in which the time and frequency resolution is fixed. [60]

The main advantages of the CWT is that the adaptive windows - by means of altering the value s - allow for the information in time and scale to be presented simultaneously, it allows for modal parameter estimations and it is applicable for damage identification in structures. The CWT also allows for good decoupling of vibration modes (only if the natural frequencies are not overlapping or close to each other), which makes extraction of damping and frequency values possible. [67] The CWT does have some shortcomings, due to its impracticality and lack of redundancy. [58] It is more impractical due to the computational cost to find the coefficients at every scale value. It lacks redundancy as there is only one decomposition possible per signal being analysed. [60] To overcome some of these challenges, the discrete wavelet transform (DWT) can be applied.

2.5.2. Discrete Wavelet Transform

The discrete wavelet transform (DWT) discreties the scaling and translation factors, by using dyadic translations and scales. This means that the decomposition is done with discretized values of s and u by integer powers of two. This allows for more efficient analysis with lower computational costs. Low- and high-pass filters are used at different cut-off frequencies for further frequency analysis, as shown in Figure 2.13. [60]

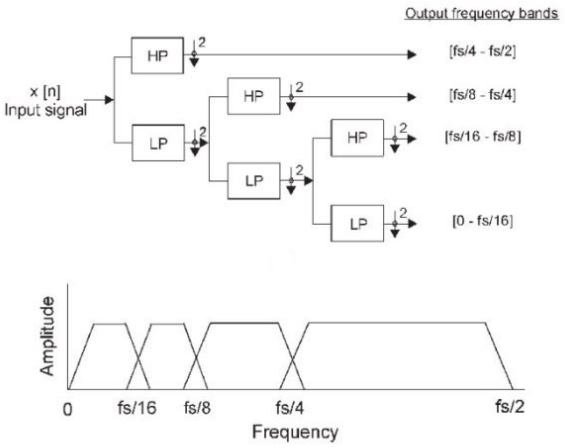

Figure 2.13: Signal decomposition of the original signal $x[n]$ and f_s begin the sampling frequency, taken from [68]

The DWT function is defined by means of equation

$$DWT(m,n) = \sum_{n} x(n) \frac{1}{\sqrt{s}} \psi^*(\frac{n-u}{s}), \tag{2.22}$$

in which n is the reference to a sample in the discrete input signal $x(n)$, m and n are integer parameters for the discretized scaling function $s = s_0^m$ and and translation function $u = nu_0 s_0^m$. The values of s_0 and u_0 depend on the chosen wavelet. [68] The original signal $x(n)$ can be recomposed by the detailed (D) and approximation (A) coefficients by

$$x(n) = A_N + \sum_{j=1}^{N} D_j. \tag{2.23}$$

In this equation, N represents the total decomposition level and j the individual decomposition levels. As shown in Figure 2.13 the original signal is passed through a low- and high-pass filter (both being finite impulse response (FIR), which corresponds to the chosen scaling and wavelet function, allowing for the signal convolution (decomposition). Where the CWT only uses a wavelet function, the DWT requires a scaling function. Important to understand is that only orthogonal wavelets (wavelets of which its wavelet transform is also orthogonal) require scaling functions. The scaling function is represented as

$$\phi(t) = \sum_{n=0}^{N} l(n)\phi(2t-n) \tag{2.24}$$

in which $l(n)$ is the converged final value of the impulse response. [60] The scaling function prevents the need of an infinite amount of wavelet functions. This scaling function must satisfy three conditions, being: [60]

1. The scaling function integrates to a value of 1:

$$\int_{-\infty}^{\infty} \phi(t)dt = 1; \tag{2.25}$$

2. It has an energy value of 1:

$$\int_{-\infty}^{\infty} | \phi(t) |^2 \, dt = 1; \tag{2.26}$$

3. The scaling function and the integers after translation are orthogonal:

$$\langle \phi(t), \phi(t-n) \rangle = 0. \tag{2.27}$$

After passing through the filter, the signals samples are devided by a factor of 2, meaning that all the other samples are taken from the signal after convolution. [58] Figure 2.13, shows these output frequency bands at each level of decomposition. This means that every level of decomposition shows a different frequency spectrum of the original signal, allowing good signal analysis possibilities. [68]

Overall, the DWT is better in real-time structural monitoring than CWT, as sudden changes in structural properties (degradation in local stiffness) seem to appear clearly using DWT signal analysis. [60]

2.5.3. Wavelet Packet decomposition

Applying wavelet transform analysis, both CWT and DWT, can result in a poor resolution in the high frequency ranges. This, due to the detailed coefficients not passing through another filter. [68] The wavelet packet transform (WPT) is a method to overcome this disadvantage. [60] It not only provides the decomposition of the low-pass filter (approximation) coefficients (as the DWT does), but also for the high-pass filter (detailed) coefficients at each level, as shown in Figure 2.14. Similar to the WT, the WPT provides wave forms containing position and scale parameters. In addition, the WPT provides the wave forms with frequency characteristics. [64]

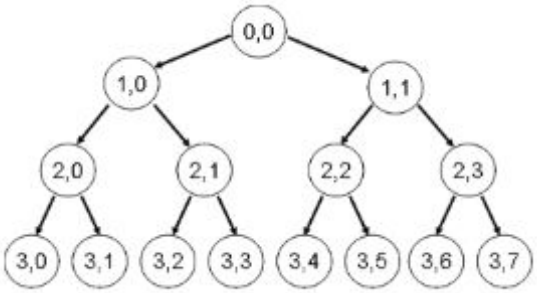

Figure 2.14: Wavelet packet transform tree diagram of which the numbers represent the wavelet packet, taken from [64]

The WPT signal $f_j^i(t)$ is a function of coefficients $c_{j,k}^i$and the (linear) wavelet packet function $\psi_{j,k}^i(t)$, represented as [60]

$$f_j^i(t) = \sum_{k=-\infty}^{\infty} c_{j,k}^i \psi_{j,k}^i(t). \tag{2.28}$$

The coefficients in Equation 2.28 are obtained by [60]

$$c_{j,k}^i = \int_{-\infty}^{\infty} f(t) \psi_{j,k}^i(t) dt. \tag{2.29}$$

A prerequisite for the WPT to work, is that only wavelets with orthogonal properties are applied. [60] The two main difference of the WPT compared to the DWT, is schematically represented in Figure 2.15. The first difference is that at every decomposition level, both the detailed and approximation coefficients are further passed through a high- and low-pass filter. The second difference is that the frequency range of all the coefficients at each range is the same. [68]

So in conclusion, the time domain analysis, frequency domain analysis, WT and the FT methods have similarities and dissimilarities. When looking at the time and frequency domain methods, they are both

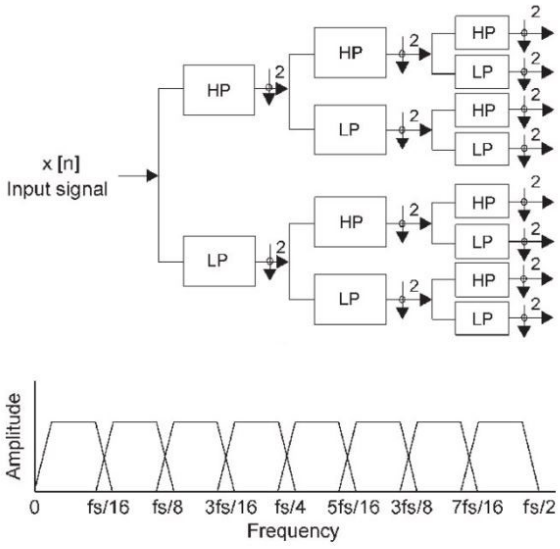

Figure 2.15: Wavelet packet transform signal decomposition of the original signal $X[n]$ and f_s begin the sampling frequency, taken from [68]

simple methods, returning information in only the time or frequency domain. When looking at the WT and the FT, both the methods are linear, the basis functions required for the methods are frequency localized and create similar matrices of the transform. The dissimilarity of the WT compared to the FT is that the wavelets used for the WT are also localized in space and can be defined in many different ways, as the sine and cosine FT functions are not and are limited in possibilities. The possibility that the FT offers when windowing is applied, allows for high resolution transform signals which are of same quality in all the time-frequency regions. The WT has this in lesser amount (dependent on the type of WT used), due to allowing variations in the window size. This allows for adjusting the window to the signal, leading to better signal analysis possibilities. [58] Figure 2.16 schematically shows the resolution in the time-frequency domain between the STFT and the WT in which can be seen that the resolution in time and frequency is fixed with the STFT and variable with the WT. For the WT, the time resolution is higher at higher frequency levels, where the frequency resolution is better at lower frequency levels. As higher frequency portions of the signal tend to be brief and very localized in time compared to the lower frequency parts of the signal. Lower frequencies thus do not require a narrow time frame to be detected, allowing for broader time windows.

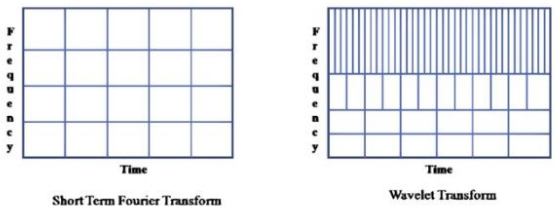

Figure 2.16: Resolution of the STFT (left) and the WT (right), taken from [69]

2.6. Wavelets and their properties

Now that the basis of the WT is formed, the focus can be placed on the types of wavelets available. Each wavelet has its own characteristics, meaning that every application or area of interest in the signal requires a different wavelet. It is therefore important to choose the right wavelet for the application. This paragraph will describe the different wavelets available, containing characteristics and possible

applications.

Basically the wavelets can organized in three generations. The first generation wavelets were developed as the Fourier transform could not provide localisation in space, required additional algorithms for fast signal analysis, did not have the possibility to adapt to the most current problems, did not consist of arbitrary domains and it could not provide analysis of irregular data. The wavelets which are classified as the first generation are Haar, Meyer, Daubechies, Morlet, Shannon and Coiflet. They did require the Fourier transform for them to be effective, but they provided localisation in space and no additional algorithms were required. What first generation wavelets are good at, is denoising of a signal, frequency identification and image compression. [58]

Because first generation wavelets still had the limitations of not being flexible, still relying on the FT and not being capable of analyzing real-world problems (being non-Euclidean spaces), second generation wavelets were developed. These wavelets were independent of the FT while keeping the time-frequency localisation capabilities possible due to the WT. These methods are based on splitting the input signal in odd (detailed coefficients) and even (approximation coefficients) samples. The detailed coefficients in the next higher decomposition level are obtained by using interpolated values of the detailed coefficients in the previous level and adding a prediction operator. This operator uses the approximation coefficients of the previous level as input of the next lower level and the detailed coefficients of the current decomposition level. This also creates filter banks on different decomposition levels, such as in the DWT. Where first generation wavelets are able to analyse signals in the $L^1(\mathbb{R})$ space (absolutely integrable signals in $\mathbb{R}$), second generation wavelets support signals in the $L^2(\mathbb{R})$ space (finite energy signals being square integrable in $\mathbb{R}$). These wavelets are primarily used for finding frequency data in signals, data compression, analysis of geographical data and graphics (computational drawing). [58]

Third generation wavelets mostly consist of the complex and bi-orthogonal wavelets. They are extremely good at reconstruction, redundancy and computation. The wavelets are based on creating filter banks (comparable to the first and second generation wavelets), but doing this in both the real and imaginary region. This makes them good in visual and graphical computational applications. [58] Complex wavelets are also capable of splitting the amplitude and the phase of the signal. [67]

Besides the three generation differences among wavelets, the wavelets can also be classified in Gaussian or Morlet families. The Gaussian wavelets are real wavelets, obtained from the standard Gaussian function. These wavelets tend to have a short duration and thus decay back to a value of zero quickly. This makes them very good in time and frequency localisation, which is one of the advantages of the WT as discussed before. These wavelets are particularly good in signal transitioning and signal deficiencies. [67] The second family is the Morlet wavelet family, of which the wavelets are complex. They are obtained by the derivation of the standard Morlet wavelet (which is a first generation wavelet). The family of the Morlet wavelets are analytic, meaning that it only has positive frequency values. [67]

For wavelets, causality (realizable) and non-causality (not realizable) is also a valid characteristic which needs to be taken into account when using the method. As stated in [70], a causal wavelet is a wavelet that has values that equal zero before its time of origin and it is only realized on the positive time scale. Non-casual wavelets are wavelets that do have a value before and after its origin time that do not equal zero. For signal filters, a filter is also called realizable when it is causal (so not dependent on future outputs). This is referred to as a causal FIR filter, which can be compared with a causal wavelet, as both the filter and the wavelet have an infinite amount of coefficients without using future signal inputs. [70]

As every wavelet is different, there is no rule that states which wavelet is the best or most effective in different applications. For a good wavelet transform application it is required to choose a suitable wavelet. [68] Therefore, the most commonly used wavelets will be further discussed below.

Haar wavelet

The Haar wavelet is a simple first generation wavelet applied in the CWT and DWT, which can be easily described as a block or rectangular wavelet. It is compactly supported in the $L^2(\mathbb{R})$ space over 1 time unit. This allows for reducing computational cost and better resolution in the time domain, but results in poorer resolution in the frequency domain. [71] The wavelet is also orthonormal. This means that the wavelet is orthogonal, but also the vectors have an unit length (in this case the energy value) of 1. [58] Orthonormal wavelets have coefficients which are independent of each other, have no energy loss during the analysis as it is all stored in the wavelet coefficients, have good localisation in time and frequency and they are easy to compute. [71][72] It is only orthonormal when the family of wavelets is constructed with integers increasing by powers of 2, which limits the translations and dilations parameters (also known as the dyadic lattice). [66] Despite the Haar wavelet being orthonormal, it is not good in localizing both time and frequency components due to the decay of the Fourier transform. [71] The Haar wavelet can be represented as [58]

$$\begin{aligned} \psi(t) &= 1 \text{ for } 0 \leq t < \frac{1}{2} \\ &= -1 \text{ for } \frac{1}{2} \leq t < 1 \\ &= 0 \text{ otherwise.} \end{aligned} \tag{2.30}$$

This wavelet is typically good at analyzing rectangular signals, images and video's due to its rectangular nature, as shown in Figure 2.17. [58]

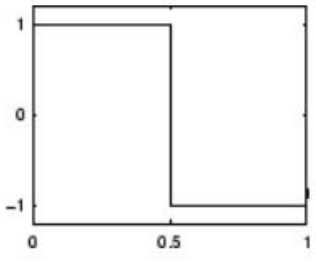

Figure 2.17: Haar wavelet, taken from [73]

When using the Haar wavelet in CWT, the wavelet shown in Figure 2.17 is used. When the Haar wavelet is used for DWT, the Haar wavelet is applied by means of using low- and high-pass filters containing coefficients. These coefficients are shown in Figure 2.18. These are discrete values within a time unit of 1, as this is where the Haar wavelet exists for. The Haar coefficients are positive or negative values of $1/\sqrt{2}$. In this case, the h-terms represent the low-pass filter coefficients and the g-terms represent the high-pass filter coefficients required for decomposition of the signal. [74]

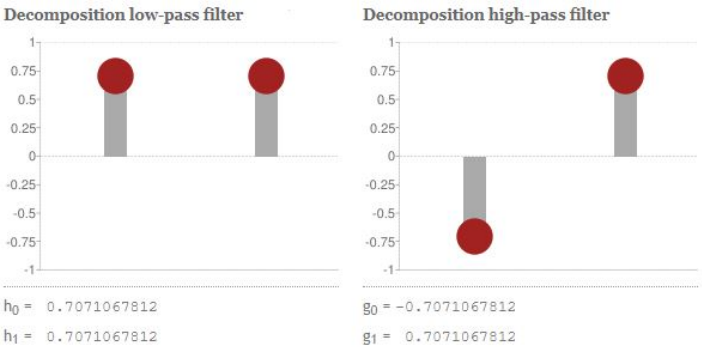

Figure 2.18: Haar wavelet, taken from [75]

The signal f, which is discretized to signal x at the time units in which the Haar wavelet filter coefficients

exist, is multiplied by the filter coefficient matrix H. This multiplication returns the coefficients in matrix X as represented in

$$X = H \cdot x. \tag{2.31}$$

Here, X consists of the decomposed discrete signal, which is subdivided into 2 sub-signals half the length of the original signal. The first half of the coefficients in matrix X are the trend (approximation or scaling coefficients) and the second half represent the fluctuation (detailed or wavelet coefficients). [74][76] The Haar wavelet further consists of another characteristic, also known as the small fluctuation feature. This feature allows for the magnitude of the detailed coefficients (fluctuation) to be significantly smaller than that of the original signal. This feature makes the Haar wavelet ideal for signal compression. In more detail, we can define a third property for the Haar wavelet:

"*If a signal is (nearly) constant over the support of the Haar wavelet, then the fluctuation values in all decomposition levels are (nearly) zero*". [76].

When applying the Haar wavelet in DWT, the original signal after the decomposition is two times smaller in length than before the decomposition and the coefficients are also shrunk by a factor of $\sqrt{2}$ in magnitude. Initially the multiplication of $\sqrt{2}$ was to preserve its energy during the decomposition. Shrinking the time intervals during multi level decomposition, some energy will be lost (approximately 0.002% at the first level decomposition) as this is inevitable due to the Heisenberg inequality. [76] Multi level decomposition with the Haar wavelet is possible as long as the discretized signal allows for a coefficient degradation by a factor of 2. [74]

The main characteristics of the Haar wavelet are thus that it can both be used in CWT and DWT analysis, it is compactly supported, it is orthonormal, it preserves energy (especially in a 1-level decomposition), it compresses the original signal and it is the most basic wavelet available in wavelet transform analysis. The downside is that this wavelet transform does not have a good resolution in both time and frequency, which other wavelets do have, as described further below.

Daubechies wavelet

The Daubechies wavelet is another type of anti-symmetric, compactly supported (support width over $2N-1$ time units) and orthonormal wavelet, capable of CWT and DWT. [58] The wavelet is orthonormal, the family of wavelets consists of N vanishing moments and consists of extremal phases. [58] The more vanishing moments, the higher the oscillations of the wavelet. Vanishing moments are represented in the Daubechies wavelet family as dbN, in which db indicates the Daubechies wavelet and N is the index number referring to the amount of vanishing moments. Its number of coefficients are indicated as $2N$. The scaling and wavelet coefficients, also indicate the time units required in the original signal during the DWT. [77] Extremal phase means that the sum of the squared coefficients increases way more rapidly than those of other wavelets, such as the Symlet and Coiflet wavelets. [78] A wavelet is said to have an extremal phase when the roots of the polynomial equation - when making an orthogonal and compact supported wavelet - are present in the complex unit circle. This creates filters that contain non linear phases resulting in high energy values at the low valued intersections on the x-axis (abscissas). [79] The Daubechies wavelet family is represented as

$$\psi(t) = \sum g_k \phi(2t-k), \tag{2.32}$$

in which the scaling function ϕ has compact support and the filter coefficients g_k are > 0 for a finite number of indices. [66] The Daubechies 1 ($db1$) wavelet is similar to the Haar wavelet, as shown in Figure 2.17. For $N > 1$, the Daubechies wavelets are shown in Figure 2.19. These wavelets are mostly used in applications such as image compression, ultrasonic wave analysis, denoising, self-similarity determination of signals and communication. [58] Due to the variety of the Daubechies wavelet family, its usage is broad.

The principle of applying the Daubechies wavelet is exactly the same as that for the Haar wavelet, as the approximation and detailed coefficients are obtained by applying the scaling and wavelet coefficients to the discretized signal. Due to the Daubechies wavelet family having other characteristics as compared

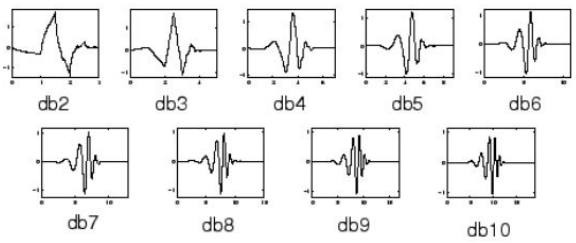

Figure 2.19: Daubechies wavelet family, taken from [73]

to the Haar (or other) wavelets, the coefficients thus differ. The main differences are the shape of the wavelets and the amount of supports the wavelet requires. The WT using the Daubechies wavelet can be performed as long as the signal being analysed can be divided by a factor of 2. [77] The scaling function, wavelet function, scaling coefficients and wavelet coefficients of the db3 (3 vanishing moments and 6 scaling and wavelet coefficient values) are shown in Figure 2.20.

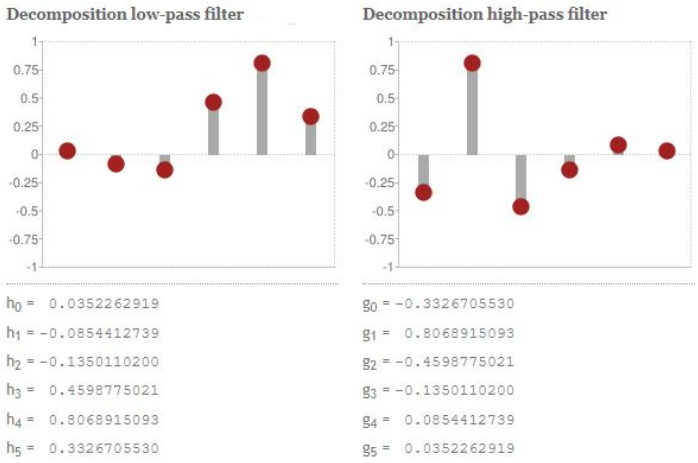

Figure 2.20: Db3 wavelet, taken from [75]

Similar to the Haar wavelet transform, the Daubechies wavelets all have an energy of 1, meaning that it is also a good wavelet when energy conservation is required. It also allows compaction of the signal, making it good for signal compression. [77] Furthermore, the $db2$ and the $db3$ wavelets have some important characteristics, compared to the third property of the Haar wavelet:

1. "*When the signal is (nearly) linear within the support of the $db2$ wavelet, the fluctuation value over all the decomposition levels is (nearly) zero*". [77]

2. "*When the signal is (nearly) quadratic within the support of the $db3$ wavelet, the fluctuation value over all the decomposition levels is (nearly) zero* ". [77]

When looking at characteristic 1 and 2, the $db3$ wavelet will return fluctuation values of a smaller magnitude compared to the $db2$ wavelet fluctuation values. Thus, when compression is the goal, the higher order Daubechies wavelet will be the wavelet of choice. When feature extraction of the signal is the goal, lower order Daubechies wavelets are the best choice as the turning points of the signal can be better represented. [77] Figure 2.21 shows this feature schematically and thus indicates that lower order wavelets are better at indicating the turning points in the signal than higher order wavelets. The largest detailed coefficient value (fluctuation values) are obtained at the turning points of the signal (peaks and valleys). [77]

Thus, when looking at the second Daubechies property defined previously, the higher order dbN wavelets will produce larger numbers of fluctuation values when applied on higher order polynomi-

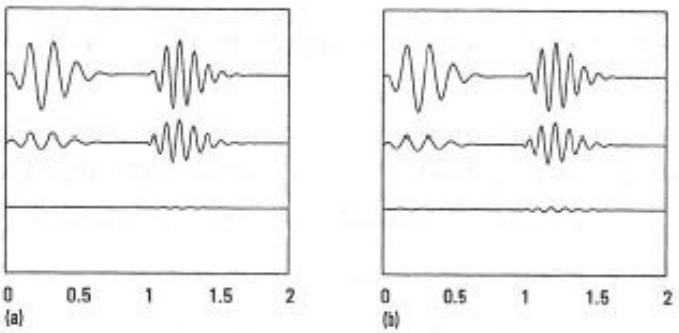

.

Figure 2.21: (a) The top signal shows the original signal, the middle signal represents a $db2$ 1-level transform (scaled by a factor of 1000) and the bottom signal represents a $db3$ 1-level wavelet transform (scaled by a factor of 1000). (b) The top signal is the original signal, the middle signal is a $db2$ 3-level decomposition (scaled by a factor of 30) and the bottom is the $db3$ 3-level decomposition (also scaled by a factor of 30). Figure taken from [77]

als. So, the higher the amount of fluctuation numbers during the wavelet transform, the better the wavelet is at signal compression (and noise removal). [77] This can be formulated as:

3 "*When the signal is (nearly) the same as a polynomial of an order less than $N/2$ within the support of the dbN wavelet, the fluctuation value over all the decomposition levels is (nearly) zero*". [77]

Coiflet wavelet

The Coiflet wavelet, abbreviated as $coifN$, is a family of wavelets which are compactly supported (over $6N-1$ time units), orthogonal, has $6N$ coefficients and consist of $2N$ vanishing moments. The latter characteristic means that the wavelet has a good compression ratio and is the main characteristic why it differs from the Daubechies wavelet. [77] The wavelets are not fully symmetrical, but are near symmetrical and represented as

$$\psi(t) = \sum_{n} 2g[n]\varphi(2t-n), \tag{2.33}$$

in which $g[n]$ is the wavelet coefficient. The application of the Coiflet wavelet is mostly in image compression, signal processing and computer visualization. [58] The family of wavelets is shown in Figure 2.22.

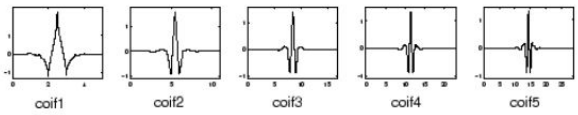

Figure 2.22: Coiflet wavelet family, taken from [73]

The Coiflet wavelet family, of which all the wavelets are similarly defined, is particularly good at following the trend of the original signal. This means that the approximation coefficients, obtained due to the scaling coefficients, are good at following the original signal. As for the Haar and Daubechies wavelet, the Coiflet wavelet also has an energy conservation characteristic being a value of 1. This is due to both the scaling and wavelet coefficients having similar energy of 1. [77] The scaling and wavelet coefficients for the $coif1$ wavelet is given in Figure 2.23.

The Coiflet wavelet is especially good in approximating the original (analog) signal when compared to the Haar or Daubechies wavelet. This means that the Coiflet wavelet has a higher degree of accuracy in the trend (approximation) coefficients than that of the Haar or any Daubechies wavelet. [77]

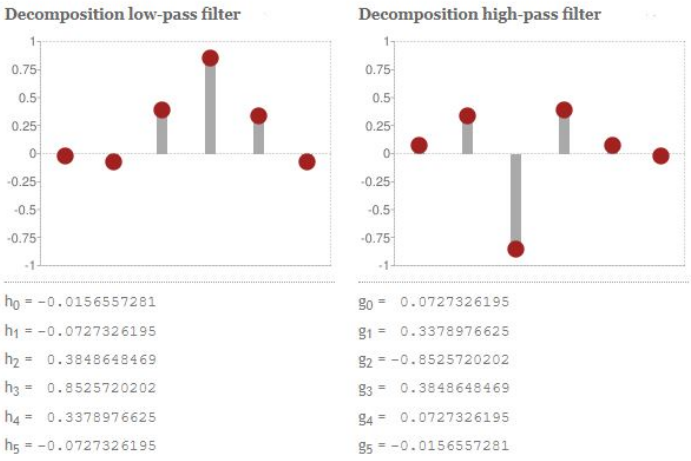

Figure 2.23: Coiflet1 wavelet, taken from [75]

Symlet wavelet

The Symlet, also defined as the $SymN$ wavelet is a family of anti-symmetric wavelets. As the schematic representation of the wavelets in Figure 2.24 already do suggest, is that they are similar to the Daubechies wavelets. The $Sym2$ wavelet is also known as the 'Daubechies least asymmetric wavelet'. [58] Due to the similarity to the Daubechies wavelet, the Symlet wavelets have the same characteristics as the Daubechies wavelet, such as energy preservation, its applicability in both the CWT and DWT, the amount of compact supported units $(2N-1)$, number of vanishing moments (N) and the wavelength FIR filter coefficients $(2N)$. Applications of the Symlet wavelet are in signal analysis, load forecasting, denoising of signals, speech and temperature data, image processing and the compression of images. [58]

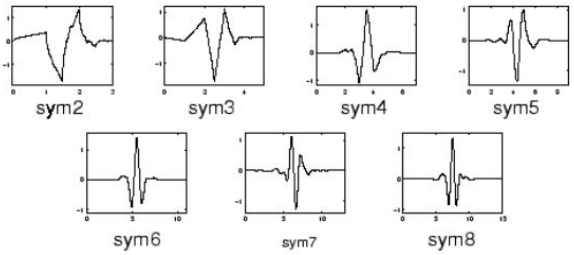

Figure 2.24: Symlet wavelet family, taken from [73]

Morlet (Gabor) wavelet

The Morlet (or Gabor) wavelet is a complex continuous wavelet (applicable for CWT) which can be ideally used when good localisation in frequency and time is required in the analysis. It is a combination of a sine function included in a Gaussian window, [58] defined in the frequency domain. [66] This leads to the wavelet shown in Figure 2.25. The wavelet is represented as a function of a complex sine function within a definable Gaussian window, defined as

$$\psi(t) = e^{(2i\pi ft)} e^{(\frac{-t^2}{2\sigma^2})} \tag{2.34}$$

in which f is the frequency in Hz, i is the imaginary part defined as $i = \sqrt{-1}$, t is the time in s and σ is the Gaussian window defined as $\sigma = \frac{n}{2\pi f}$. In the Gaussian window, the factor n defines the number of cycles of the wavelet. [80] This wavelet is special, as it does not meet the requirement of the mean value being zero, as stated in equation 2.17. It is made nearly zero by making the center frequency and the bandwidth of the wavelet large enough. [66] The Morlet wavelet is mostly used for analyzing sound patterns, but is also used for heart beat analysis and other non-stationary signals. [58] The Morlet

wavelet can also be used for source localisation of an impact. [63] One must take two assumptions into account when using the complex Morlet wavelet. The first assumption is that the analysed signal must be a sine like function. The second assumption is that the analysed signal must be stationary within the non-zero energy part of the wavelet. If both assumptions are not met, the obtained signal will be difficult to interpret. [80] The wavelet is a short burst, with values in the negative and positive x-axis, meaning that this is a non-causal wavelet by the definition given in this section. [58] This wavelet has the best resolution in both the time- and frequency domain, as the wavelet has a decay that is exponential in both the time and frequency domain in the $L^2(\mathbb{R})$ space. [66] This has to do with the uncertainty principle, earlier referred to as the Heisenberg inequality. One must take into account that the wavelet is symmetric on the y-axis, where the sensor signal response is not symmetric.

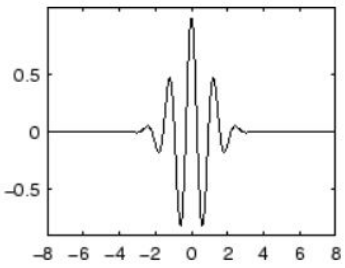

Figure 2.25: Morlet wavelet, taken from [73]

Meyer wavelet

The first generation Meyer wavelet is also a real continuous wavelet with a orthonormal basis, applicable for the CWT, which is symmetric and decays fast. It is not compactly supported and is infinitely differentiable. [58] The Meyer wavelet is shown in Figure 2.26a and it is primarily used in processing and recognition of images, processing and filtering signals and compression of signals and images.

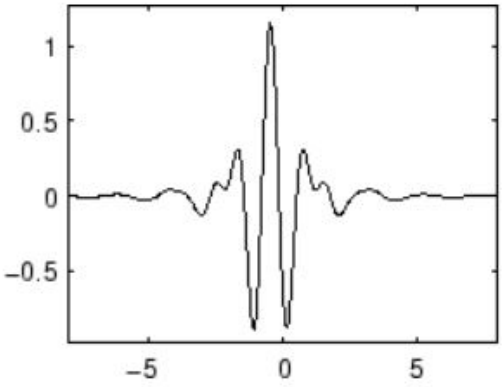

(a) Meyer wavelet, taken from [73]

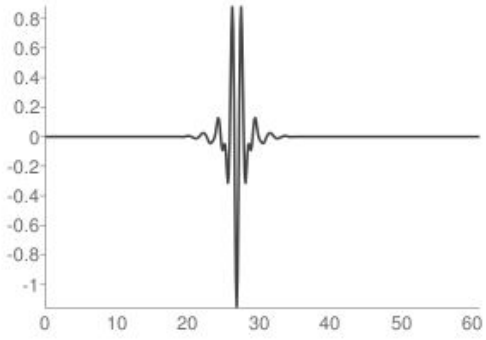

(b) Discrete Meyer wavelet, taken from [75]

Figure 2.26: Meyer wavelets

As the Meyer wavelet is not capable of discrete wavelet analysis, due to its continuous properties. The discrete Meyer wavelet can offer this capability. This wavelet (Figure 2.26b) is obtained by applying the finite impulse response (FIR) filter to the Meyer wavelet, making it an approximation version of the original Meyer wavelet. This allows for the discrete Meyer wavelet to be orthogonal and compact supported. [81]

Biorthogonal wavelet

As stated previously, biorthogonality has a particular advantage over orthogonality. It both constructs a wavelet and scaling function pair for both the decomposition as the reconstruction, resulting in the possibility to reconstruct and decompose at the same time. [58] The wavelets are compact supported

and can thus be used in both the CWT and DWT analysis methods and they are symmetric. [82] It is represented as

$$\psi^d_{jk}(t) = 2^{\frac{-j}{2}}\psi^d(2^{-j}t - k), \tag{2.35}$$

in which ψ^d represents the duality of the basis wavelet ψ_{jk}. The family of wavelets is shown in Figure 2.27. The biorthogonal wavelets allow for different filter widths, resulting in excellent coding of images, but may cause signal degradation due to the slight offset of the filters. In most cases, an orthogonal wavelet can also satisfy the biorthogonal characteristics, but only if this particular wavelet is not symmetric. The biorthogonal wavelets are shown in Figure 2.27.

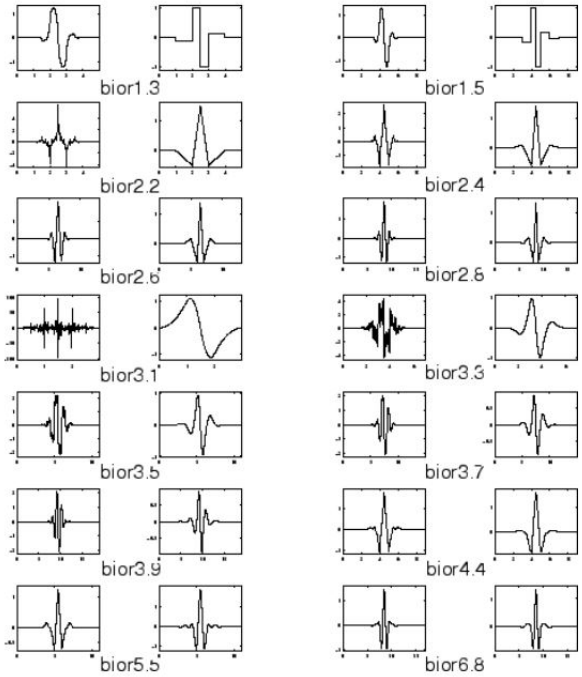

Figure 2.27: Biorthogonal wavelet family, taken from [73]

Shannon wavelet

The Shannon wavelet is a continuous wavelet, as shown in equation 2.36. This makes this wavelet very useful for the continuous wavelet transform, but the downside is that this wavelet does have a poor time localisation. Due to their discontinuity in the frequency domain, the wavelet spreads out in the time domain. [58] The wavelet is compact supported in the frequency domain and due to its continuity, it has a very poor attenuation in time. [66] The continuity of the wavelet is shown in Figure 2.28.

$$\psi(t) = \frac{sin(\frac{\pi}{2}t)}{\frac{\pi}{2}t}cos(\frac{3\pi}{2})t \tag{2.36}$$

The Haar and the Shannon wavelets are the most extreme examples of wavelets due to their characteristics. The Haar wavelet is compactly supported in the time domain, resulting in a poor decay, thus resolution in frequency. The Shannon wavelet is compactly supported in frequency, but therefore has a poor decay in time. Most other wavelets are within these two extremes. [66] The application of the Shannon wavelet is best in determining radar cross section analysis, but can also be useful for signal analysis and reconstruction engineering problems. [58]

Mexican Hat wavelet

The Mexican Hat wavelet is a symmetric, real and even valued wavelet, but not compact supported and not orthogonal. The wavelet has been widely used in 2D image processing, but is also used for

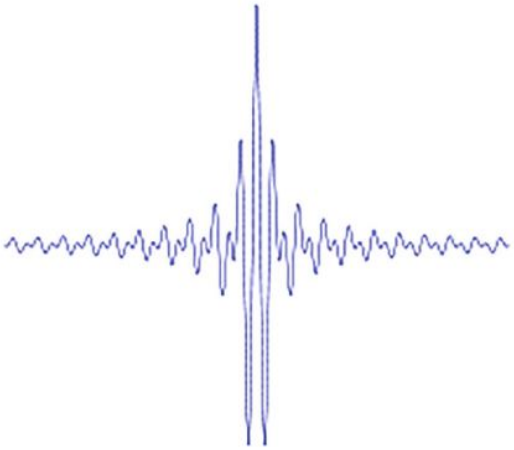

Figure 2.28: Shannon wavelet, taken from [58]

approximation of non-linear functions. The Mexican Hat wavelet is especially good at denoising signals with a low signal-to-noise ratio (SNR). [58] The wavelet is shown in Figure 2.29.

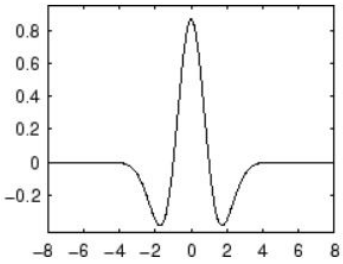

Figure 2.29: Mexican hat wavelet, taken from [73]

A short summary of all the above described wavelets is given in Figure 2.30. For clarity, some definitions of the properties are given in Table 2.4.

Other wavelets

Besides the previously described wavelets, their are countless more. Wavelets that primarily originated from first and second generation wavelets, are the Pet Hat, Berlage, Spline, Lemarie-Battle, Mallat, Poisson, Mathieu, Stromberg and many more. They will not be further discussed, as they are not used in signal analysis. As previously described, the complex wavelets are third generation wavelets, which are wavelets that have a zero value when the Fourier transform is applied with negative frequency values. [67] Examples of complex wavelets are for instance the generalized Morse wavelet, analytic Morlet (Gabor) wavelet, Bump wavelet and the complex frequency B-spline wavelet. [84] As researched by Ciampa and Meo. [63] the complex Morlet wavelet is typically good at separating the frequency from the time component and is able to better localize frequencies from signals having large oscillations in time. Primarily, these wavelets are used in CWT analysis, in which scalograms are the result. These scalograms represent a similar result as the STFT, but then with both good resolution in frequency and time. Besides the well known wavelets, there is also a possibility to make new wavelets. They can be fully adjusted to the application for which it is attended for.

2.7. Summary

This Chapter described the basic theory and knowledge required for the thesis subject. Relevant decisions such as the use of guided waves, focusing on passive SHM applications and the use of PZT and FBG sensors and have been made, to narrow down the thesis scope. Also, different time, frequency and time-frequency domain analysis methods have been discussed, describing the advantages and

Properties	Morlet (morl)	Mexican-hat (mexh)	Meyer (meyr)	Haar (Haar)	Daubechies (dbN)	Gaussian (gaus)	Symlet (symN)	Coiflet (coifN)	Biorthogonal wavelet pairs (biorNr.Nd)
Regularity	Infinitely	Infinitely	Infinitely	No	Arbitrary	Infinitely	Arbitrary	Arbitrary	Arbitrary
Compactly supported orthogonal	No	No	No	2	2N − 1	No	2N − 1	6N − 1	$2^{Nd} + 1$
Symmetry	Yes	Yes	Yes	Yes	Asymmetry	Yes	Near symmetry	Near symmetry	Yes
Number of vanishing moments	—	—	—	1	N	—	N	2N	Nr − 1
Existence of scaling function	No	No	Yes	Yes	Yes	No	Yes	Yes	Yes
Orthogonal analysis	No	No	Yes	Yes	Yes	No	Yes	Yes	No
Biorthogonal analysis	No	No	Yes	Yes	Yes	No	Yes	Yes	Yes
FIR filters (length)	No	No	No	2	2N	No	2N	6N	Yes
Fast algorithm	No	No	No	Yes	Yes	No	Yes	Yes	Yes
CWT	Yes	Yes	Yes	Yes	Yes	Yes	Yes	Yes	Yes
DWT	No	No	Yes	Yes	Yes	No	Yes	Yes	Yes
Explicit expression	Yes	Yes	No	Yes	No	Yes	No	No	For splines

Figure 2.30: Summary of characteristics of the previously described wavelets, taken from [83]

disadvantages of every method. With these decisions and relevant knowledge, a sufficient theoretical foundation has been formed to understand the research topic. This basis will be further expanded with a state-of-the-art literature review about the thesis subject in Chapter 3.

Table 2.4: Wavelet property description summary

Wavelet property descriptions	
Property	**Description**
Redundancy	Possibility to have multiple decomposition within one analysis.
Regularity	The amount of continuous derivatives the function contains, also known as the smoothness of the signal. Feature extraction in smooth data requires a wavelet with a high smoothness. The higher the amount of vanishing moments, the smoother the wavelet most often is. [84]
Small fluctuation feature	The signal magnitudes of the original signal are larger than those of the fluctuation sub-signal.
Compact supported	Defines that the wavelet is finite and has a limited support size, containing non-zero values in the basis function (giving the localized features).
Support size	Indication of the FIR filter length in (time) units.
Orthogonal	Orthogonality means perpendicular and is met when the integral of the inner product of a set of functions over time is zero.
Orthonormal basis	An orthonormal basis is formed when the vectors used are unit vectors(length of 1) and they are all orthogonal.
Biorthogonal	Besides decomposition wavelet and scaling coefficients, biorthogonal wavelets provide reconstruction wavelet and scaling coefficients.
Symmetry	Defines if the wavelet filters have a linear (symmetric) or non-linear(non-symmetric) phase. Linear filters decay the frequency components by the same value containing the original signal shape, whereas the non-linear phase filters do not decay by the same value.
Vanishing moments	Factor of how fast the wavelet decays to a value of zero and defines the amount of oscillations a wavelet has.
Extremal phase	A wavelet has an extremal phase when the filter coefficients are within the unit circle of the complex plane, resulting in a non-linear phase. These wavelets have high energy values at the low valued intersections on the x-axis.
Scaling function	Provides the scaling coefficients (LPF).
Wavelet function	Provides the wavelet coefficients (HPF).
FIR filter	Filter with a finite length.

3

Literature study

This Chapter contains the literature review, in which the state-of-the-art literature regarding impact damage detection and quantification is described. First, the impact damage quantification and identification methods will be discussed, together with some applications. It has been chosen to not describe any impact damage detection methods on their own, as the damage is detected when quantification is applied. Also, this section will not be limited to only passive SHM and FBG sensors, to broaden the methodology possibilities. This literature study will be concluded, in which the found gaps in knowledge are described. Finally, these gaps in knowledge are used to define the research questions and objectives, forming the basis of this research.

3.1. Impact damage detection and quantification

The goal of this section is to explore the impact damage quantification and identification research field, to find the research possibilities for passive SHM in aerospace structures. This section will focus on the research done in quantifying and identifying damage, induced by an impact. The main focus is to research the passive SHM field, but active SHM will also be part of this section, to broaden the scope. Again, the focus will not only be on optical sensors, as other types of sensors have been used for this application and can be relevant for this thesis. Finite element modelling (FEM), artificial neural networks (ANN), damage parameters (DP), auto-regressive modelling and wavelet transform (WT) analysis are key topics and are further discussed with their applications in the following paragraphs.

Inverse finite element method (iFEM)

The inverse finite element method (iFEM) is a numerical approach, which has been proven successful for shape sensing as it is fast, robust and accurate. [85] Recently it is shown that it is also a valid method to use for SHM. [86] This method is based on the displacement and strain fields, allowing the monitoring of the structure without baseline knowledge of the material or even the load conditions of the structure. By knowing the structure, boundary conditions and using a known strain sensor grid, the displacements of the nodes can be calculated. This method requires a limited amount of computational power and is therefore convenient for real time monitoring. The iFEM can be used with triangular, quadrilateral and curved shell elements. [86] The algorithm, as described in [86], uses a quadrilateral four-node shell element. By implementing local strains, the algorithm allows for calculation of global strain fields based on applicable boundary conditions and of course the dimensions of the structure. The least-square method was used to optimize the difference in strain between the computed and input strain. A geometrical difference, for instance induced by a damage, can be detected in the model and the real structure. This will eventually lead to a deviation in the displacement field which the model reconstructs. This difference can be linked to some sort of damage.

Colombo et al. [86] used the iFEM method to identify damages in composite panels. They found that previous research had only focused on isotropic materials. In this study a damage index, referred to as the anomaly index (AI), was defined as being a load and material independent index. It enabled the definition of a load adaptive baseline of the pristine structure. They used this method on a unmanned

aerial vehicle (UAV) composite stiffened structure in which an impact was initiated for damage introduction. The model was built with iQS4 (quadrilateral) elements with a meter long FOS network for constant monitoring of the structure. By fatigue testing, the damage in the structure could be identified. This paper prove that this method is effective in identifying damage in composite structures, but the application used in this paper was fatigue testing, which is outside the scope of this literature review.

Artificial neural network

An artificial neural network (ANN) is an inverse machine learning (ML) optimization technique, which is one of the six existing artificial intelligence (AI) methods. [87] The basic working principle of ANN is to identify connections between a series of input and output parameters. It is a statistical (learning based) computational model, which runs parallel to the physical structure, learning from experience, calculating and identifying unknown results without knowing the initiator of the event. This allows for ANN to calculate non-linear multidimensional structural problems, generating information on damage being present or not. Its knowledge comes from a data-set which is based on know parameters, allowing for calculations of damage being present in the current state by approximating the frequency response function of a dynamic system. [20][23][88] Typically, the difficulty of using ANNs is that they most often require data of the structure in pristine and damaged state, meaning preliminary tests on the structure have to be done. Sometimes there is no structural information of the damaged state, meaning no data is present and the ANN cannot be used. This can be overcome by using the validated (numerical) finite element method (FEM) to obtain the information required in damaged state. [87] Also, besides having to be successful in impact damage localisation, ANN is still vulnerable with measuring stable inputs, has challenges with noise and outliers, no balance between pristine and damaged structure data, a necessity for generalisation in unfamiliar environments and having solution convergence difficulties. [20][89]

Summarized from other research in the review paper of Su et al. [23], ANNs have been used for identifying adhesive de-bondings of joints, cracks, through the thickness holes in cylinders and delaminations in CF/RP panels. Although this method was successful in identifying the type of damage, ANN is limited to one specific type of damage, confined structural and geometrical properties and limited amount of loading and operating conditions. Making one ANN to broaden the application, requires excessive research meaning that for now multiple ANN algorithms should be implemented to identify multiple types of damages in a broad mixture of structural and operational conditions. ANNs also require excessive training for effective results. [21] More recent research shows that ANNs can be used to detect and identify damages in structures due to impacts. Doan et al. [90] showed that ANNs accuracy for damage identification in reinforced concrete (RC) can be increased by presenting automatic hyperparameters from GAs and particle swarm optimization (PSO) . The strategy was further optimized by including a stepwise gridsearch (SG) method with a nested cross-validation (NCV) to further define the optimal parameters required for the ANN. Califano et al. [91] could detect damages in CF/RP plates by means of an ANN method, where in situ strains were used to train the ANN model. This research showed that ANNs do not necessarily require a reduction of the data by means of data reduction procedures and do not have to be linked to certain damage patterns. This means that this method requires less processing time and limited computational cost.

Auto-regressive modelling

Auto-regressive (AR) modelling is a data fitting method, which represents time series data. The model has its origin from econometrics, but has found to be useful for SHM applications. [92] The value given, is based on a linear and finite group of values including a random error. By using methods such as the least-square or Yule-Walker method, unknown values in the AR equation can be computed. This method can be adopted for SHM applications by a residual error method or by using the computed AR parameters, which are included in the response time series equation. The latter method requires structural information of both the pristine and damaged structure. By means of this data, damage can be classified during its in surface life time. As this method is a time-fitting model, one must decide which order of model is required. Higher order models fit the data better, but limit its use to a specific application. Lower order models have lower data fitting capabilities, but do allow for better representation of the structure damage dynamics. To help determine the required order for the model methods such as Akaike's developed Information Criterion (AIC) and Final Prediction Error (FPE) . Root Mean Square

(RMS) and Partial Autocorrection Function (PAF) methods can also be used. [93] The downside of the previous methods, is that they require estimations of the AR model parameters. This lead to methods based on the Singular Value Decomposition (SVD) technique, which do not required these estimations of the parameters. [93]

In the same paper of Nardi et al. [93], the AR method is used for low velocity impact damage detection on CFRP structures. They used the time history of the response signals (measured with PZT sensors) from these undamaged and damaged CFRP specimens and used them in the AR model. They found that the specific order of this model should be 45, thus defining this as the amount of parameters required in the model. By then using pattern recognition techniques and classification operations they were able to identify delaminations in the specimens.

Damage parameter

The damage parameter (DP) is another effective method to detect and characterize damage, both on a passive and active SHM manner. [94] This method can both be used for low and high impact damage events, of which low speed impacts are mostly affected by the applicable boundary conditions and high speed impact events are dominated by the induced waves. The damage parameter (DP) is defined as an equation in which the extent of the damage is defined as a arbitrary parameter (the DP). The variables are set to unity. [94] Different DPs can be defined with different variables, as will be shown in the following state-of-the-art articles.

Zamorano and Elvin [94] have researched a passive SHM method to quantify and characterize damage induced by high speed impact events on a fibre glass composite panel, in which PZT strain sensors are embedded in the first ply for signal detection. The high speed impacts were simulated by a 5.56 mm projectile of 1.1 gram. For damage characterization, the induced damage due to these high speed impacts were validated by C-scan NDT. The proposed DP includes the attenuation parameter of the fastest anti-symmetric Lamb wave mode and is related to the energy of the impact. The time history of the wave is calculated by the passive PZT sensor network. The proposed DP and delamination radius and area is related, making it possible to use the DP as a damage indicator. Limitations of this specific research is that (1) impacts close to the sensors result in a non-valid DP and (2) fibre orientation and the angle of the impact are not related to each other. Further work should include these factors. De Luca et al. [95] used a DP on a glass fibre composite complex winglet structure for real-time damage detection by means of PZT sensors. Jang and Kim [59] used 5mm long FBG sensors for real-time low-velocity impact induced delaminations in a CFRP panel with 180 x 180 x 5.1 mm dimensions. All four edges of the panel were fully clamped. Impacts were induced by a 12.7 mm diameter hemispherical impactor. Signals were interrogated by a commercial high speeds interrogator, capable of sampling at 100 kHz. The damage index used for delamination detection uses the D_1 aspect of the wavelet transform (which will be discussed in the next paragraph) in the time-frequency domain. It was shown that the D_1 component has a large noise portion in the signal, which can affect the damage characterization results. This research could not find the precise results of damage being present as validated NDT methods can do. But considering the system was monitoring a large area with a simple system, makes this method suitable for delamination detection in composite panels.

Wavelet transform analysis

The wavelet transform (WT) is a method which decomposes the signal into coefficients within fixed frequency bands using wavelets. These wavelets are alternative families, decomposed in basis functions represented as a and d components, from the original time-frequency domain signal $f(t)$. [96] This is schematically represented in Figure 3.1, in which is shown that the wavelets are stretched or narrowed signal versions of the main signal $f(t)$. These wavelets allow the limitations of normal STFT analysis to be overcome, such as low resolution and only able to analyse a small section of the spectrum. Also, because the wavelets are both expressed in time and frequency, they can be used as multi-scale band-pass filters. Another big advantage of decomposing the signal $f(t)$ into wavelets is that wavelets show signals in time and frequency, which is invisible in signal $f(t)$. More theory about the WT is given in Chapter 2.

Sung et al. [96] used the WT to detect impact damages and also to characterize the signal deviations due to matrix cracking and free-edge delaminations. The impacts were induced at low velocity on a

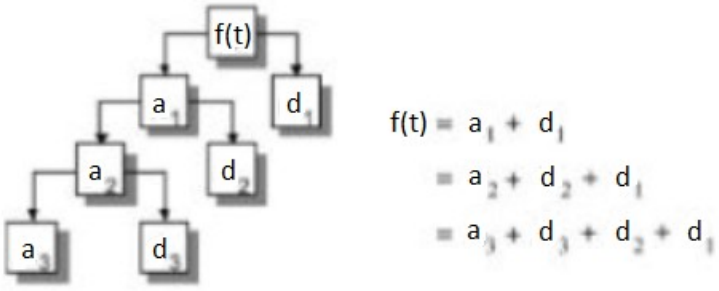

Figure 3.1: Wavelet transform decomposition example, in which $f(t)$ is the response signal, a_i is represents the low frequency components (*approximations*) and d_i represents the high frequency components of the signal (*details)* for $i = 1, 2, \ldots$, modified from [96]

composite laminate, after which the WT was used to identify signal characteristics indicating a certain type of damage. Signals were obtained by means of PZT sensors capable of detecting signals up to 2 MHz. This research showed that matrix cracks were dominantly shown in the d_1 wavelet, as delaminations were predominantly represented in the d_2 wavelet. Jang and Kim [59] used the d_1 wavelet for quantitative evaluation of the signal, as this portion has the highest frequency range. This portion of the signal showed that additional peaks (compared to the pristine signal) are measured at the time of the delamination event in the laminate. In other research of Jang et al. [97], four 5 mm long FBGs were used as sensors. At that time a high speed interrogation method, capable of sampling up to 100 kHz, was used. Impacts were induced between 15 and 30 Joules. First, STFT was used for signal analysis, but this was not accurate enough for damage detection in composite panels. Therefore the researchers chose the wavelet transform, dividing the waves in d_1 to d_4 components. This allowed the researchers to achieve signal references, indicating damage was present. The researchers stated that both at 40 kHz and 100 kHz sampling frequencies are sufficient for (1) impact damage localisation and (2) for detecting damage occurrences, making this an interesting article for the future work done in this thesis.

Conclusion

In the above sections, methods and research articles regarding (impact) damage detection and quantification have been presented and reviewed. Detecting impact damage is easier compared to quantifying the impact damage, especially when focusing on passive real-time SHM methods. For detection, deviations in the signal when compared to the pristine case is one of the easiest ways to detect a damage. No further details of different damages under different environmental conditions are required to understand in full. For impact damage detection, this method is also used within this thesis due to its simplicity. The downside is that pristine signals are required in the database. Quantification methods are more difficult, but methods have been researched by using, for instance, the inverse finite element modelling, artificial neural networks, auto-regressive modelling, damage parameter and the wavelet transform. The iFEM method quantifies damage by using the displacement and strain fields. Due to its limited requirement for computational power, it is a convenient method for real-time monitoring of structures for instance for impact damages. ANNs have been proven effective in quantifying debondings of joints, cracks, through the thickness holes and delaminations, but they require excessive training and is thus not the method chosen for the thesis. AR modelling is a time-fitting model of which the order of the model should be chosen. The higher the order of the model, the better the fitting but limits its application possibilities. Lower order models have lower data fitting accuracy, but represent the dynamics of the structure damage better. The DP is used in both passive and active (low and high velocity) impact damage detection applications. The DP is a specific predefined equation of which the variables have been set to unity. Due to its simplicity and the possibility of monitoring large areas of a structure, it is a suitable method for delamination quantification in composite panels. The last method, the WT, is an effective method which decomposes the signal by means of wavelets. These decompositions are capable of showing responses in the signal which are not visible in the original signal. This makes it an potentially effective method to detect and to link the signal response to a specific type of damage. As no reference signal is prerequisite, but does make it more easy for signal analysis, this method will

be the chosen method for damage quantification.

The fact is, that more guided wave case studies must be researched and developed to broaden the passive real-time in-service damage detection and quantification. [20] This literature review allowed for a brief and clear overview in the relevant theory and the state-of-the-art regarding (real-time) active and passive SHM. From the presented literature with the best ability of the researcher, it can be concluded that the main gaps in knowledge found with this literature review, are that:

- most researchers based their measurements on signal acquisition by means of PZT sensors and other sensor types may contribute to similar or better results;
- PZT sensors are able to sample in the MHz range, but FBG sensors are thus far only capable of a maximum 100 kHz sampling rate and using higher sampling rate interrogators could contribute to better results. Better interrogators can potentially contribute to more accurate damage localisation results and maybe contribute in quantifying damage in composite structures;
- most SHM (impact) damage detection and quantification research focused on simple structures such as panels;
- the majority of case studies on impact damage detection and quantification are based on active SHM, meaning that passive SHM can be further explored to contribute to real-life impact damage detection on composite structures;
- real-life in-service monitoring currently is limited compared to active non-real-time monitoring, meaning that more case studies are required [20];
- quantification of damage with real-time SHM is proven effective by means of acoustic emission. [12]

3.2. Research Question and Objective

3.2.1. Research Questions

Structural health monitoring (SHM) can potentially contribute to a higher availability of aircraft and lower operational costs. Recently, the Royal Netherlands Aerospace Centre (NLR) has acquired the Redondo FBGT-M1200 interrogation system capable of sampling up to 1 MHz per FBG. This possibly allows some of the limitations of current optical monitoring systems to be overcome and can lead to a beyond state-of-the-art development in fibre optic sensing in damage detection, further researched in this thesis. Also, well known PZT sensors will be used for verification. Also, damage quantification is more difficult, for which more case studies and methods need to be developed. Therefore, the contribution to the *gap in knowledge*, is introducing another case study for both simple and complex structures, where damage detection and quantification features are defined. From this literature review, the aim of the thesis is defined in the following main research question:

"*What signal features can be extracted real time from response signals, measured with a PZT and FBG sensor network, after an impact on composite structures and can these features be linked to specific damage types using the wavelet transform?*"

To answer this research question, the following sub questions need to be answered:

1. "*What wavelet transform analysis method and wavelet are suitable for application in a (real-time) impact damage monitoring algorithm?*"
2. "*What signal features in the response signal of a simple composite plate are representative for an impact damage and can these features be related to a certain type of damage being present after an impact event?*
3. "*How do the defined signal features from the simple composite square panel compare to a complex stiffened composite panel and what influence do the measurements over thickness steps and stiffeners have on the damage detection and quantification possibilities of the algorithm?* "

3.2.2. Methodology

The research objective, also referred to as the research goal, is defined as what the researcher is set to achieve during its research. The main research objective of this thesis is to investigate the capabilities of a PZT and a state-of-the-art FBG sensor system for passive impact damage detection on composite panels and complex stiffened composite structures. To achieve this objective, the high frequency sampling interrogation system needs to be validated for damage detection by comparing it with validated sensor types (PZT) and by means of experiments and signal analysis. The research objective will be met when the main research question is answered and signal characteristics can be linked to certain types of damages.

The hypothesis linked to the research objective, is that the signal responses from the PZT/FBG sensors should deviate in a certain frequency band when damage occurs upon impact, when comparing these signals to non damaging impact responses. If this hypothesis is true, this deviation in the signal response could be related to a certain type of damage being present, also referred to as feature extraction.

To achieve this main research objective and to test the hypothesis, the following sub-goals are formulated and achieved in this research project:

- *Literature:* Perform a relevant literature review, consisting of the relevant theory required for the problem and the state-of-the-art research done in this research field.
- *Experimental:* Perform experiments on a composite panel to gather the relevant results from the different types of sensors chosen. These results form the basis of the research questions and objectives stated. If required, tests should be performed on more complex stiffened composite structures.
- *Signal analysis/Feature extraction:* Analyse the obtained experimental signal responses and determine if relevant characteristics can be sustainably related to an impact damage events for potential real-time structure monitoring. If possible, apply this on multiple types of panels.
- *Report writing:* Write a report, in which all relevant theory and results are included. Draw conclusions from these results and do recommendations for future research.

4

Wavelet transform selection

"What wavelet transform analysis method and wavelet are suitable for application in a (real-time) impact damage monitoring algorithm?"

To analyse signals, many analyzing methods have been developed. For this thesis, the wavelet transform (WT) has been chosen to analyse the impact signal on the composite structures. To answer the first research sub-question as shown above, first the wavelet transform method is chosen. This is done by using the theory described in Section 2.5 and applying it to the desired results taking the advantages and disadvantages into account. Secondly, the wavelet is chosen by means of benchmarking the described wavelets from Section 2.6. A conclusion will be formulated, in which the first research sub-question will be answered. The chapter will be concluded with observations and lessons learned.

4.1. Wavelet transform method

As described previously, there are three WT methods being the CWT, DWT and WPT. Each of these methods have their own advantages and disadvantages, making them suitable for certain applications. CWT has the main advantage that it has adaptive windows and good decoupling characteristics, making it possible to extract the damping and frequency characteristics out of the original signal. But, due to its high computational cost and lack of redundancy (single decomposition per analysis), it is less suitable for the real time SHM method being developed in this thesis. For real time applications, the DWT is more applicable, as it does not lack redundancy and the analysis is more efficient resulting in less computational cost being required. More analyses can be performed simultaneously. The DWT is also better in identifying sudden changes in the response signal due to a drop in stiffness (e.g. AE due to damage) or by means of an external event (e.g. impact). As a variance on the DWT, the WPT can also be used. The WPT overcomes the possible lack of resolution in both time and frequency in the high frequency ranges, but therefore also requires more computational cost. The WPT has fixed frequency bands, increasing the resolution in the higher frequency ranges. But, the amount of data which is produced by this method, makes the analysis more difficult. The number of frequency bands increases exponentially with the desired decomposition level. For feature extraction, as desired in this research, this method provides too small frequency ranges, making the analysis more difficult. The WPT can be used when in depth analysis needs to be performed in the higher frequency ranges. For the WPT to work, only orthogonal wavelets can be used.

So in conclusion, the DWT will be used as main analysis method due to its advantages over the CWT. Primarily, due to the computational cost and its impracticality (the way results are displayed), CWT is not suitable for a real-time impact damage monitoring application. As the WPT can give some more information in the higher frequency parts of the signal and could be used as a method for further in depth analysis.

4.1.1. Wavelet selection

Besides the WT analysis method, the type of wavelet is also relevant to choose correctly. To give an indication what type of signals are to be analysed, an example of the FBG data is represented in Figure

4.1. The situation was with a sampling frequency of 937.5 kHz with non-damaging impacts on the panel.

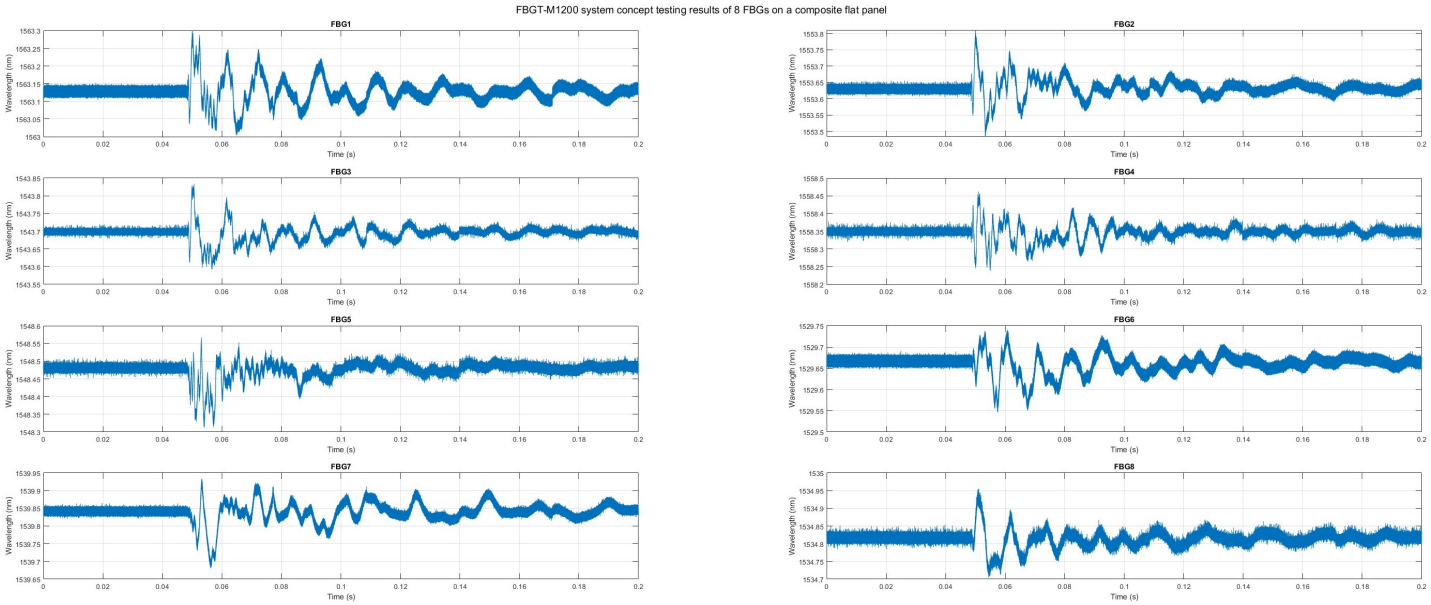

Figure 4.1: Example of FBG response signal taken from the system concept testing at NLR.

Within multi resolution analysis (MRA), wavelets are typically good in feature detection, energy preservation, denoising and signal or image compression. [84] When looking at energy preservation wavelets, wavelets such as Haar, Daubechies, Coiflets and Symlets can be best used. They all have the same characteristics as it comes to the energy preservation property as described earlier. When denoising of the signal is relevant, orthogonal wavelets are the best choice. Wavelets such as the Haar, Daubechies, Symlet, Coiflet and the Bi-orthogonal are the best choice. Signal compression can best be done by Bi-orthogonal wavelets which are compactly supported, as they have both a pair decomposition and reconstruction scaling and translating coefficients. This duality also ensures a better regularity. [84] Bi-orthogonality is also achieved in other wavelets, but only if these wavelets are non-symmetrical. For the application in this thesis, energy preservation and feature detection is the most important property that the wavelet must have. Energy preservation allows for signals to not be lost during analysis. When the signal has features close to each other in time, a wavelet with a small support size is needed. When the features in the signal are further away, wavelets with higher supports are to be chosen. This bench marking leaves the current choice to the Haar, Daubechies, Coiflet and Symlet wavelets.

As the DWT is chosen as the main WT analysis method, the wavelet needs to be compatible with this method. Looking at the Haar, Daubechies, Symlet and Coiflet wavelets, all wavelets are compatible in both the CWT and DWT. Therefore, there is no further benchmarking when comparing it to this characteristic. As the response signals from the sensors are smooth (high regularity), the wavelet should support this regularity. This will allow for detecting abrupt changes in the signal. This means that the Haar wavelet and the db1 (equivalent to Haar) are not suitable for the analysis. The Haar wavelet is also not good at localizing both the frequency and time components, due to the decay of the FT. As it is required to have both good localisation in time and frequency for the real time application, the Haar wavelet will not be further applied. The Daubechies, Symlet and Coiflet all are orthogonal, compact supported and consist of vanishing moments. Here, the Daubechies and Symlets are very similar, as stated in the detailed description of both the wavelets. The Coiflet differs in its compact supported value and its number of vanishing moments. When looking at symmetry, the Daubechies wavelet is asymmetric, whereas the Symlet and Coiflet wavelets are nearly symmetric. This means that the Coiflet and Symlet have linear phase where the Daubechies has non-linear phase, making the Daubechies wavelet less computational costly in theory.

When looking at the original impact signal in Figure 4.1, the Daubechies and Symlet wavelets seem

to have similar wave structures, as where the Coiflet is symmetrical along the y-axis at the highest peak of that Symlet. The original impact signal is not, where the main choice of wavelet possibilities for analyzing the signals, will be the Daubechies and Symlet wavelets. Lower valued wavelets of both the Symlet and Daubechies wavelet are better at feature extraction. These lower order wavelets are orthogonal and compactly supported and thus tend to have good localisation in both time and frequency. In contrast, higher order wavelets (higher regularity) are better at signal denoising and compression and fit smooth signals (with few transients) better. In this work, the impact signal is transient, containing abrupt changes in time after impact and possibly damages due to these impacts. For detecting these signal features, low order wavelets are preferred. Thus, where higher order wavelets most often fit more transient signals better, lower order wavelets are better in detecting abrupt changes in the signal. When also taking computational cost and published literature in consideration, the Daubechies wavelet is a proven wavelet and is the final wavelet of choice for this thesis. A sufficient regular wavelet for this application is the db5 wavelet, containing a FIR filter of 10 data points. It also has a similar form when compared to the signal to be analysed.

4.2. Conclusion

To answer the research question: "*What wavelet transform analysis method and wavelet are suitable for application in a (real-time) impact damage monitoring algorithm?*", a more in depth analysis of this time-frequency domain analysis method and the applicable wavelets has been performed. The sub-question will be answered below, highlighting the main points of interest.

The wavelet transform analysis methods available are primarily the continuous wavelet transform (CWT), discrete wavelet transform (DWT) and the wavelet packet transform (WPT). Their main **characteristics** are basically the same, where they are all time-frequency domain analysis methods, capable of extracting features from signals while taking the Heisenberg inequality into account. By means of convolution, by using a wavelet, the signal features are extracted from the signal. These results have a high resolution in both time and frequency, unlike signal filtering, the FT or the STFT. The CWT uses dilation and translation parameters in its equation. By means of integration over time, the features are extracted from the signal. The DWT and WPT are both discrete variations of the CWT, where these dilation and translation functions are discretized. The DWT and WPT are performed by means of a summation of these discretized results. The **overall advantages** of all three WT methods compared to the other signal analysis methods, is that the resolution in both time and frequency are taken into account (instead of choosing only one parameter with a high resolution). The main **advantages of the CWT** are that it allows for good decoupling of vibration modes in signals, having adaptive windows and allows for modal parameter estimations. The **disadvantages of the CWT** method are that it is computationally costly, impracticability and lack of redundancy. The DWT and WPT overcome these shortcomings. Where the DWT can lead to low resolution in the higher frequency ranges, the WPT has fixed frequency bands in which signal features are represented. The disadvantage of the WPT compared to the DWT (for this application), is that the amount of WT frequency bands increase exponentially when increasing the decomposition level. The higher the decomposition level, the shorter the frequency bands, but the more frequency bands need to be analysed. Therefore, the DWT will be used as main analysis method.

For the WT method, multiple **suitable wavelets for damage detection (and quantification)** have been discussed. For each wavelet, the main characteristics are covered. By means of benchmarking, where literature, wavelet characteristics and signal features are taken into account, the Daubechies 5 (db5) has been chosen as wavelet for the further analysis. It is an asymmetric, compact supported and orthonormal wavelet which preserves energy and has a similar trend as the signal obtained by the impacts tests. It is also a wavelet which is sufficiently regular, can be applied in the DWT.

4.3. Observations and lessons learned

In this Chapter, the WT has been analysed extensively. The WT has been compared to other time-, frequency- and time-frequency domain analysis methods. Also different WT techniques have been discussed, making this an expansion of the literature review done in Chapter 3 Some choices were made taking the future application of the developed algorithm, where real-time structural impact dam-

age monitoring is the goal, into account. For this application, a CWT or a WPT analysis could have been a better option, but computational cost and amount of decomposition results respectively where the main drivers to choose the DWT as method. If the application is sufficient in use, the DWT should be the overall goal. The choice of the DWT obviously means that a compromise has been made with time and frequency resolution of the WT, where the resolution in the higher frequency ranges is less than the resolution at the lower frequency bands.

For the wavelet selection, in total 10 wavelets have been discussed in more detail. This is a small amount when compared to all the possible wavelets. Also, the WT allows for the development of a new wavelet, which can be used for the application. For this research, the choice of wavelets has been based on literature found during the literature review, but also by analyzing the application possibilities of some more wavelets. The final wavelet selection was done by benchmarking it to literature, advantages and disadvantages of the wavelet for this application. The reason why no wavelet has been developed for this application, is due to its complexity. Also, the Daubechies wavelet has been proven in other literature and is the best choice during the benchmarking for this application.

5

Wavelet transform analysis on unstiffened composite structure

"What signal features in the response signal of a simple composite plate are representative for an impact damage and can these features be related to a certain type of damage being present after an impact event?"

5.1. Method

The signal responses were obtained by performing impact tests in the laboratory of NLR. The tests have been performed in a total of 3 days, which has resulted in all the required data to answer this second research sub-question. For the detailed testing procedure, a test plan has been developed which is added in Appendix A. Section A.1 contains all the information required for good execution of the impact tests. In addition, Section A.2 contains extra information why certain choices have been made for the test plan and what the working principle is of certain interrogation systems.

Not all signals are fully reliable due to events such as a sensor or interrogator malfunction. These unreliable signals are identified by means of a detailed analysis on the trend of the unprocessed sensor signals. This data can lead to false conclusions. Therefore, this corrupt data was not used in the analysis. What data is left out of the analysis and for which reason, is represented in Table 5.1 for IL1 to IL6 and in Table 5.2 for IL7 to IL12. The orientation and location of the sensors and the impact locations are shown in Figure 5.1. Taking the values in the Table into account, PZT6 shows the most reliable and consistent data, especially in the higher impact energy regions.

Also, the weight of the impactor has been changed during impacting to achieve higher impact energies. To check if the data is the same for different weights, a short analysis is done. The PZT6 10J impact data from the 1154g and 2356g impactor weight are compared at IL1. The results are shown in Figure 5.2. As can be seen, the sensor data is not identical using different masses for the same impact energy levels. For the first 3 milliseconds, the trend of the signals seem to be identical, of which only the amplitude of the signal changes. After the 3 ms, the signals start to deviate resulting in none identical impact responses. Because the response signals differ between different impact weights and the energy absorption by the panel is different with different masses, only the data obtained with the 2356g impactor will be used for further analysis.

For signal analysis and feature extraction, a specially developed MATLAB algorithm is used. This algorithm is capable of:

- importing data gathered by the sensor systems;
- plotting the signal responses for every given time interval;
- vertical and horizontal alignment of the response signals;
- calculating and visualizing of the STFT results;
- denoising the FBGT-M1200 signal when required;

Table 5.1: Excluded signals for impact locations 1 to 6.

IL (#)	Impactor weight (g)	Signal deviations
1	1154	PZT1 and PZT2 are shifted in time
		PZT3 10J from 7.92 - 7.98 ms spikes in signal
		PZT3 15J from 4.48 - 4.56 ms spikes in signal
		PZT3 20J from 7.95 - 8.00 ms spikes in signal
2	1154	PZT4 45J from 7.11 - 7.16 ms spikes in signal
		PZT4 30J from 8.64 - 8.68 ms spikes in signal
		PZT6 50J vertical jump within noise region from 0.35 ms
	2356	PZT1 65J whole signal corrupt
		PZT1 75J whole signal corrupt
		PZT2 55J with a vertically shifted signal
		PZT2 65J whole signal corrupt
		PZT2 75J whole signal corrupt
		PZT4 60J from 9.40 - 9.44 ms spike in signal
3	1154	PZT1 and PZT2 are shifted in time
		PZT1 30J whole signal corrupt
		PZT2 30J whole signal corrupt
	2356	Slight horizontal shift of 10J signal at PZT1 and PZT2
		PZT1 75J from 5.42 - 5.45 ms spikes in signal
		PZT1 85J from 6.80 - 6.90 ms spikes in signal
4	1154	PZT1 45J from 2.46 - 2.50 ms spikes in signal
		PZT1 45J from 6.78 - 6.82 ms spikes in signal
		PZT5 40J from 4.78 - 4.83 ms spikes in signal
		PZT5 40J from 5.51 - 5.56 ms spikes in signal
5	1154	PZT1 40J whole signal corrupt
		PZT2 40J whole signal corrupt
		PZT4 45J from 7.91 - 7.94 ms spikes in signal
		PZT5 45J from 9.90 - 9.94 ms spikes in signal
6	1154	PZT3 10J from 6.58 - 6.68 ms spikes in signal
		PZT4 40J from 8.50 - 8.55 ms spikes in signal

Table 5.2: Excluded signals for impact locations 7 to 12.

IL (#)	Impactor weight (g)	Signal deviations
7	5504	No bad signals
8	5658	PZT5 170J from 3.47 - 3.54 ms spikes in signal
		PZT5 110J from 4.35 - 4.43 ms spikes in signal
		PZT6 130J from 4.72 - 4.76 ms drop in amplitude, does not recover
		PZT6 170J from 3.44 - 3.45 ms spikes in signal
9	5504	No bad signals
10	5504	PZT1 170J whole signal corrupt
		PZT2 170J whole signal corrupt
		PZT3 170J from 2.60 - 2.63 ms drop in amplitude
11	5504	PZT3 100J from 4.43 - 4.87 ms data loss
		PZT5 100J from 1.48 - 1.74 ms data loss
12	5504	PZT1 170J whole signal corrupt
		PZT2 170J whole signal corrupt
		PZT5 170J data loss during the increase in voltage value

- calculating the CWT for any input signal
- calculating and visualizing of the DWT for any input signal and wavelet, both together and individually;
- quantifying the WT results;
- calculating the damaged area of the ultrasonic NDT scans.

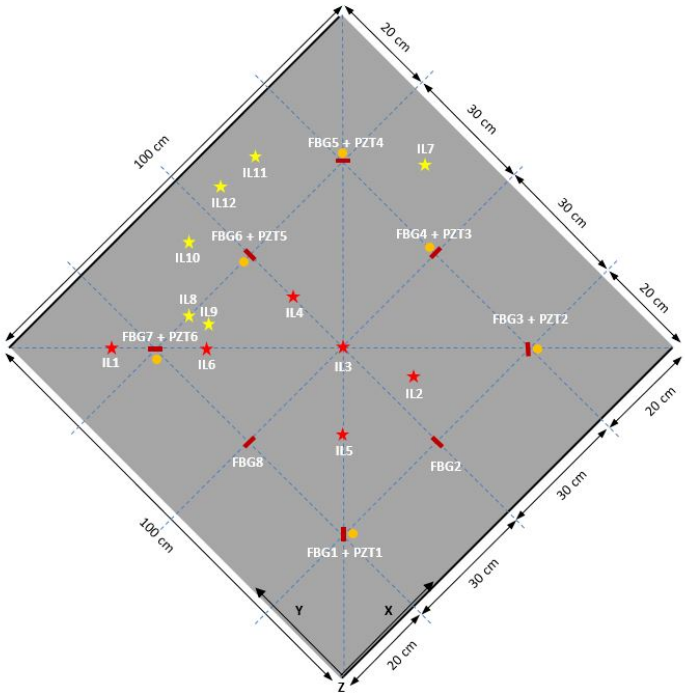

Figure 5.1: Impact locations (⋆ IL) and sensor locations (▬ FBG ● PZT) , Figure not scaled.

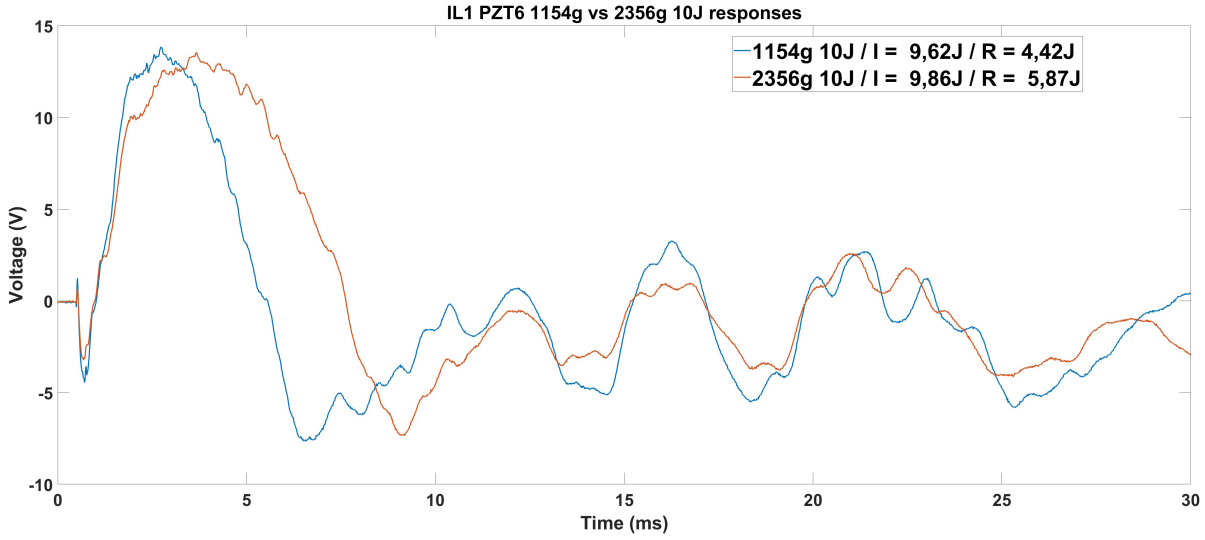

Figure 5.2: Response signals from PZT6 at IL1 of the 1154g and 2356g impactor weight at a 10J impact, with I being the real impact energy and R being the rebound energy.

As stated in Section 2.2.1, the dispersion curves display the different wave modes which propagate through the panel, in this case after an impact. Figure 5.3 shows the dispersion curves of the TenCate Cetex TC1320 composite panel, used during the impact tests. Software from the German Aerospace Center (DLR) is used. [98] The engineering constants used are represented in Table A.3 in Appendix A.2.

For damage detection, it is expected that AE signals will propagate together with the impact signal when a damage event occurs. This additional AE signal should be seen in the response signal, when (significant) damages have been initiated. What damages can be detected depends on the sampling frequency of the interrogations systems. As stated in Section 1.3, AE signals have been measured primarily in the regions from 20 to 100 kHz, but can also have frequencies up to 1 MHz. The PZT

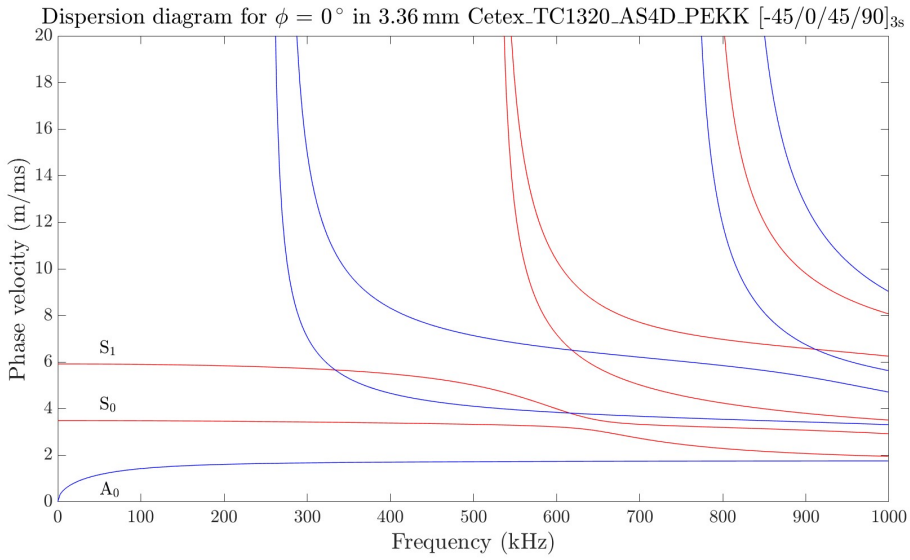

Figure 5.3: Dispersion curve of the TenCate Cetex TC1320 test specimen, calculated from German Aerospace Center (DLR) software based on the GMM. [98]

sensors will sample at 100 kHz during the first impact tests. The full frequency spectrum of these AE responses up to 50 kHz can be detected by the PZT system, when taking the Nyquist frequency into account. During the second impact tests, the sampling frequency is increased to 1 MHz, increasing the detectability of multiple failure modes. The FBGT-M1200 optical interrogation system, samples at 937.5 kHz at each FBG. Again, taking the Nyquist frequency into account, the full signal content that can be measured during the second testing phase will be up to approximately 450 kHz using the FBG and 500 kHz using the PZT. Due to the large amount of data gathered during testing, it was chosen to do a full analysis at one impact location using the data of one sensor. Additionally, some interesting locations will also be further investigated. For all tests, the environmental conditions, relevant for potential FBG compensation, were within the limits described in Section 2.2.2. Therefor no compensation of the signals due to temperature is required.

Due to the different sampling frequency data of the PZT interrogation system, the analysis in this chapter will be divided into two main sections. The first section will focus on impact locations 1 to 6, which have been sampled at 100 kHz for the PZT sensor system. The second section will focus on impact locations 7 to 12, of which the data is sampled at 1 MHz for the PZT sensor system. Both sections will first review the unedited signal responses. Secondly, the ultrasonic NDT results are analysed, including an indication of the damaged area. Thirdly, the STFT results are shown. Finally, this knowledge is taken into account when analyzing the WT. From these results, the sub-conclusions will be formulated.

5.2. 100kHz sampling rate data

For this analysis, PZT data sampled at a sampling frequency of 100 kHz will be used. The chosen impact location for this analysis is IL1 and PZT6. IL1 has the largest area of damage within this test-set, of which the top contains a dent, the bottom is cracked and delamination has occurred in the laminates in between. The most common composite failure modes are present. Also, IL1 is near the boundary conditions, meaning the panel is stiffer at this location. This more closely represents a stiffened aerospace structure compared to the other locations. PZT6 is chosen as sensor, as this sensor is near the impact location, close to two boundary conditions, but also has the most reliable data.

5.2.1. Signal responses

The response signals at IL1 of PZT6, from the impacts with the 2356g impactor weight, are represented in Figure 5.4. The response signals during the first 6 ms are similar and still in phase to one another.

Due to the difference in impact energy, the amplitudes of the signals do differ. After the 6 ms, the signals start to deviate from each other, due to boundary conditions reflections, attenuation and slowness of the signal. This leads to interaction of the original impact signals with the rebounded signals, making analysis harder in this region.

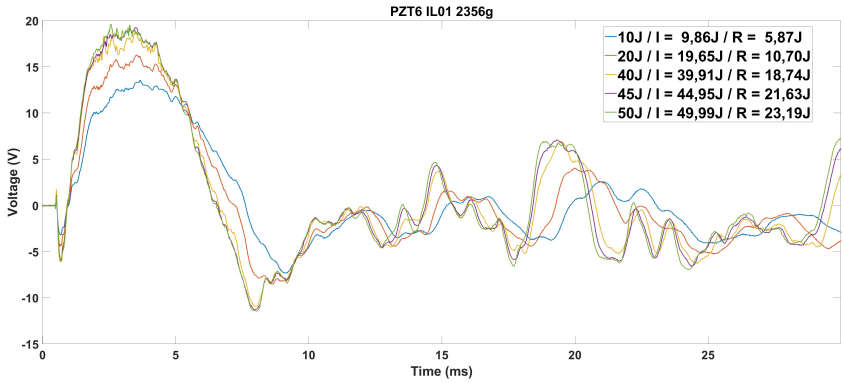

Figure 5.4: First 30 ms of the response signals from the 2356g impactor with multiple impact energies, with I being the real impact energy and R being the rebound energy.

It is also expected that damage characteristics in the signal are present in the first 10 ms after impact when looking at the dispersion curve in Figure 5.3, due to the guided wave speed propagating through the panel. The damage features travel alongside the impact waves, potentially in other frequencies and amplitudes. The longer the time after impact, the more the waves will dampen. The signal will be harder to analyse due to the many interactions of different wave types and reflections in the panel. This is again what is shown in Figure 5.4. In Figure 5.5 the signal in the red box indicates a sudden fluctuations in amplitude and phase at higher impact energies between approximately the 2.0 and 4.8 ms for the $40J$ and $50J$ impact energies. The $45J$ impact energy results do not seem to give similar results when only looking at the unprocessed signal responses. As the FBG sensors are sampled at nearly 1 MHz per sensor and the PZTs at 100 kHz, the FBG sensors are left out of the analysis in this section. The data integrity is also low due to cross-talk between FBGs, data loss and lacking high frequency component data, explained in more detail in Section 6.2.3.

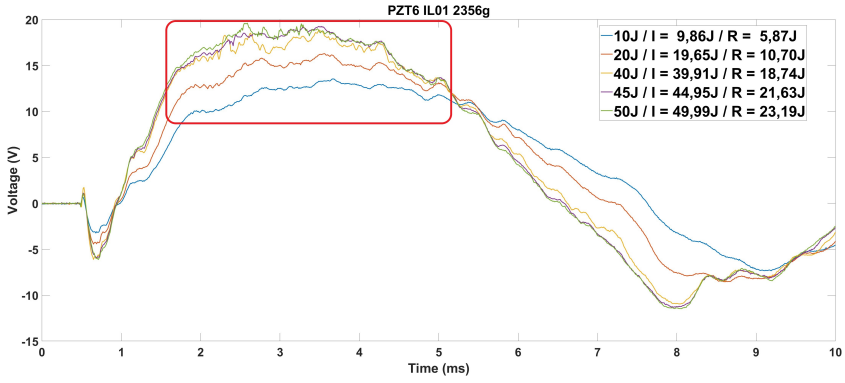

Figure 5.5: First 10 ms of the response signals measured at PZT6 from the 2356g impactor with multiple impact energies, with I being the real impact energy and R being the rebound energy.

These sudden fluctuations in the signal give the initial indication that a damage event has occurred due to the impact, which is also stated in the hypothesis linked to this research.

5.2.2. Ultrasonic NDT results

To determine if damage has indeed occurred due to the impacts, ultrasonic NDT scans obtained by the phased array Omniscan-M-PA16-128, are represented for IL1. These scans were performed after

the first and second impact test sessions. For convenience, the results of all locations (IL1 - IL6) are included in Appendix B. Figure 5.6a shows the ultrasonic NDT results of IL1. Figure 5.6b shows a picture of the damage at 50 J during impact testing.

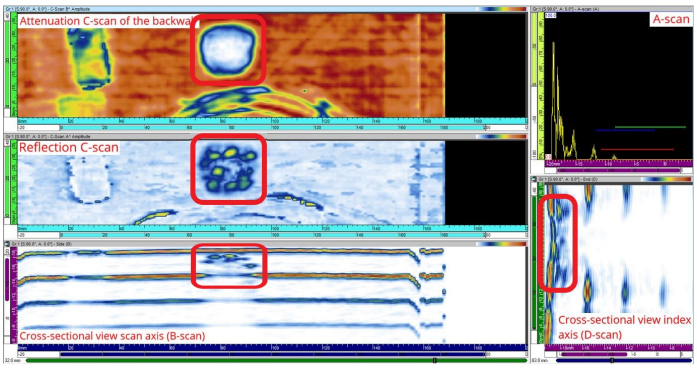

(a) Ultrasonic NDT A-, B-, C- and D-scans of the impact location.

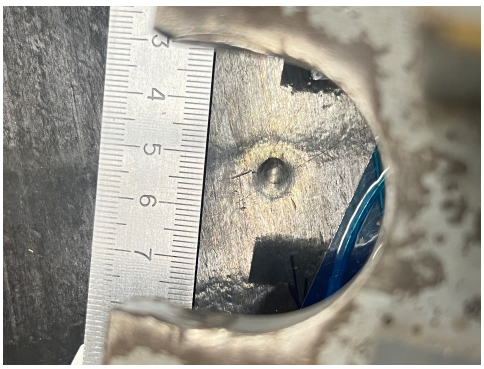

(b) Dent at the impact location.

Figure 5.6: Damage at IL1 at 50J with an impactor mass of 2356g.

The impacts have occurred at the location marked with red boxes, showing the damaged region with an total area of 361 mm^2. The impact location is clearly shown in the scans, of which the backwall reflection marks the dent and the attenuation C-scan marks the damage area within the panel. At the bottom, the attached optical fibres are scanned and do not indicate damage to the panel. To the left of the Figure, a sticker indicating the impact location, has been scanned. These locations may be ignored. The locations marked in the B- and D-scans, represent damages over the thickness of the panel. In this case, the damages are at the upper layer of the panel, recognizable by the high intensity reflection (yellow/red). The blue reflections below these delaminated area's, show the reflections of these damages. These reflections may also be ignored, as they do not indicate any additional damage.

5.2.3. Short-time Fourier transform

To check whether the signal contains any additional frequency components due to the impact damages, the STFT will be used for time-frequency domain analysis. The result of the STFT will be a spectrogram, in which the frequency content is plotted over the signal time. The intensity of the frequency content in time is visualized as the power in decibel (dB). For this analysis, a trade-off between time- and frequency resolution needs to made. This is done by selecting the correct filter of which the settings can be changed for fine-tuning of the spectrogram results. A Kaiser window will be used, as this window allows for the adjustment of the time resolution, window overlap and the leakage settings. The final spectrograms will contain all the information of IL1 and the 5 impact energies.

STFT variable settings

The time resolution is based on the trial and error method, in which the most ideal resolution in both time and frequency is obtained. The higher the time resolution setting, the wider the window size used for convolution. This will lead to a high frequency resolution, but a low time resolution. A small window will create a high time resolution, but a poor frequency resolution. For impact damage analysis, both a good time and frequency resolution is required. Time resolution is important to determine in what time interval frequency components are present due to the damage. To determine if there is damage, the frequency response is important to determine the impact damage characteristics. Setting the time resolution to 0.48 ms, the resolution in both time and frequency were such that a distinction could be made in the signal response. Due to the low computational power required for this calculation, a large overlap percentage of 99% is chosen.

Another setting in the STFT analysis is the leakage. Leakage determines the resolution of the overall plot. Random signals always have leakage, meaning that some energy of the signal will leak into an adjacent signal. The signal components are smeared over the total spectrum, disguising pure signal

features. The larger the setting of the leakage value, the better the resolution of the signal, but the more signal components are being masked due to this smearing. The lower the leakage, the lower the resolution, but the better individual responses are shown. A leakage value of 1 is equivalent to windowing the signal with a rectangular window. Using a value of 0.85 is equivalent to windowing with a Hann window. Lowering the leakage further, decreases the resolution but determines more closely spaced frequency components. For this application, a leakage value of 0.35 is used to limit the resolution loss, but to increase the closely spaced frequency components relevant for impact responses. The frequency limits are determined by the Nyquist value, meaning that all frequency components within the limits of 0 Hz to $\frac{f_s}{2}$ Hz are fully displayed in the spectrum. To increase the readability of the STFT spectrogram, the power limits are limited between the -40 dB and 20 dB. Between these limits, the changes due to the impacts are captured, without values outside of this range disturbing the signals of interest. The final input parameters for the STFT are represented in Table 5.3.

Table 5.3: STFT input parameters.

STFT Input	Value	Unit
Time resolution	0.48	ms
Window overlap	99	%
Leakage	0.35	–
Frequency limits	[0, 50]	kHz
Time limits	[0, 10]	ms
Power limits	[-40, 20]	dB

These setting lead to a time resolution of $t_{res} = 480\mu s$ and a frequency resolution of $f_{res} = 6.0737$ kHz. The value of f_{res} represents the smallest frequency value that can be distinguished in the given time interval for the analysis.

STFT analysis

For a time period of 10 ms, the results are given in Figure 5.7. In the beginning of the signal, where the first wave is measured by the sensor, the signals seem to have slight changes in the energy. These differences are related to the higher impact energy and are marked with a green box. The largest frequency changes are within the first 2 to 5 milliseconds of the signal. These regions are marked with red boxes. The results of the 40 J, 45 J and 50 J start showing additional responses. In contrast to the unprocessed signals in Figure 5.5, the 45 J impact energy results do show some additional frequency response, where this was not evident in the analysis of the unprocessed signal responses in the previous section. These areas are marked with red boxes in the Figure. The 10 J and 20 J impacts do not show these deviations in this extent, other than an increase in energy due to the difference in impact energy. The lack of these changes in spectrum may indicate that after impacts at these energy levels, do not result to damages in the panel. However, this cannot be verified due to lacking phased array scan results at these impact energies. The STFT gives an indication of damage being present, but does not allow for a detailed quantification in both time and frequency. Therefore, the WT will be used for further analysis.

5.2.4. Wavelet transform

As concluded in Chapter 4, the wavelet transform (WT) has a better time and frequency resolution than other frequency analysis methods. For the WT, the db5 wavelet has been chosen for this research and thus will be applied to the impact response data from IL1 and PZT6. Similar to the STFT analysis, the Nyquist frequency determines the frequency limit at which full signal features can be analysed. For this data, this is also 50 kHz.

Applying this wavelet to the data from IL1 and PZT6 gives the results shown in Figure 5.8. It is obvious that, similar to the STFT analysis, the signal response has more energy when higher energy impacts are induced. The difference in energy between the real impact and rebound energy increases, meaning more energy is transferred into the panel. This is seen in the amplitude changes of the signal within (most obviously) the first millisecond, marked with a green box. The peaks in all decomposition levels

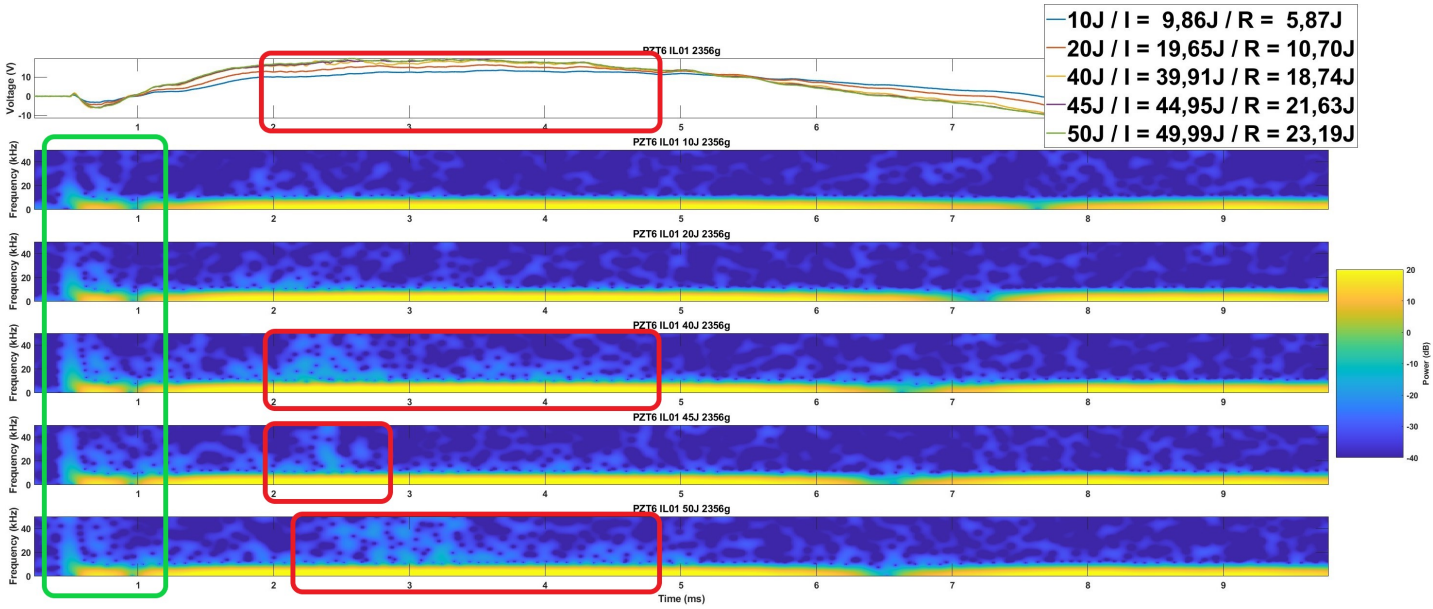

Figure 5.7: Original signals with their corresponding STFT plot for IL1 and PZT6 for 10ms.

are located at the same point in time, while deviating in amplitude from one another. Within the 2 and 4 milliseconds range, deviations in signal responses start to show for the 40 J, 45 J and the 50 J impacts, marked with the red rectangles. These are numbered 2 to 10, in the decomposition levels 1 and 2. These are the higher frequency bands (12.5 - 50 kHz) within the signal. Also the detailed levels 3 and 4 show deviations in the signal, marked locations 11 and 12, but are less evident. Decomposition level 5 does not indicate any significant changes in voltage value due to the impacts, which again shows that the damage characteristics have higher frequency values.

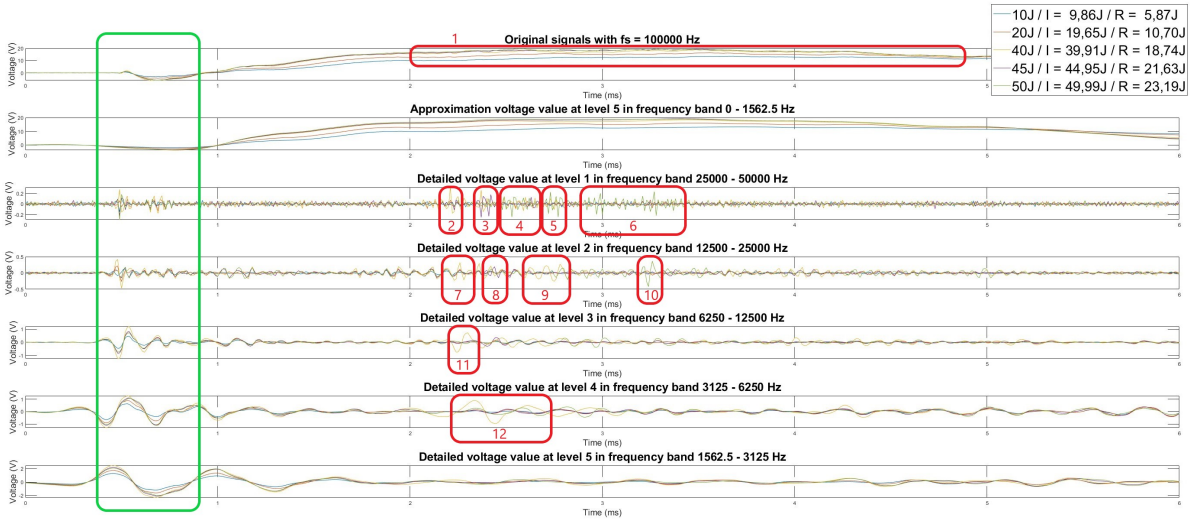

Figure 5.8: Original signals with their corresponding WT plots for IL1 and PZT6 using the db5 wavelet.

In the above analysis, it is hard to detect significant changes in the WT values. Where potential frequency components can be detected, a quantification of this portion is difficult. It is also hard to determine if these additional components are due to the increased impact energy or due to a damage event. Therefore, to visualize the WT values in a more processable way, the cumulative sum of the positive WT voltage values is applied. The time interval is kept the same. By applying this method, sudden changes in the signal will be visible as a gradient change. Energy deviations are visualised by area

changes, whereas energy is trapped within the damaged region and are not transmitted directly into the panel. When comparing these results at each level for each impact energy, a more precise indication of damage initiation is previewed. By normalizing the results, the energy data from each impact level is proportionalised. This makes signal comparison easier. Additional frequency components, for instance due to a damage event, will be visualised by a gradient increase, compared to the pristine case. Due to the levels 1 and 2 containing the largest frequency spectrum and as the largest WT features, only these two levels will be further analysed. The results are shown in Figure 5.9.

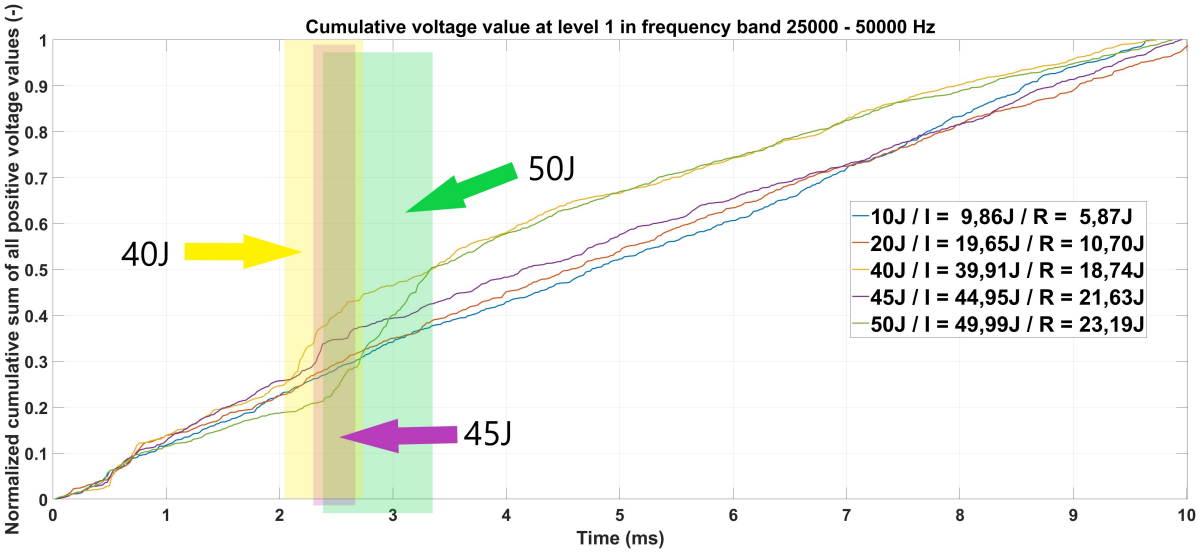

(a) Level 1

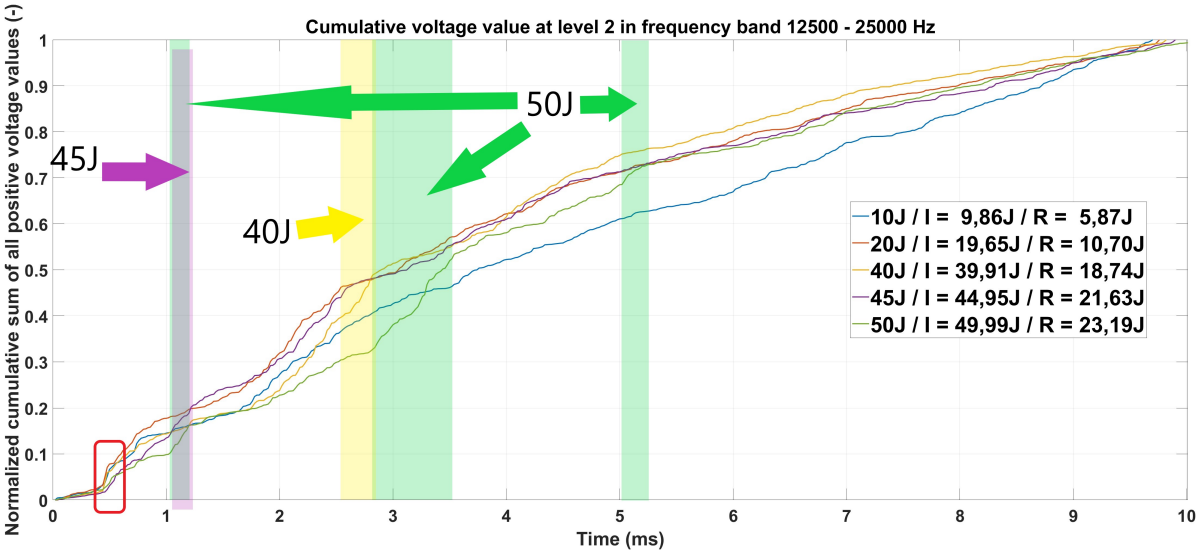

(b) Level 2

Figure 5.9: WT analysis for IL1 and PZT6.

Looking at the level 1 decomposition in Figure 5.9a, the 10 J and 20 J impact energy levels are used as pristine reference signals to which the higher impact energies will be compared. What can be seen, is that the WT results of the pristine cases are nearly similar, both in the trend as in the energy level. Linearity in these pristine cases seem to be present. When looking at the higher impact energies, signal deviations start to show in both decomposition levels. This is the case for the 40 J, 45 J and 50 J impacts. Although, as described in the test plan, ultrasonic NDT scans are only performed after the 50 J impact. This means that a valid statement of damage being present at 40 J cannot be made. But, when the data of the 40 J impact is compared to the 50 J impact, similarities in trend deviations (gradi-

ent changes) are evident. Therefore, it is highly likely that the first damages started at 40 J. Based on these results, the 100 kHz sampling frequency is sufficient for detecting damages in composite panels, induced by impacts.

When looking at the level 2 decomposition, trends in signals are harder to detect. The signals from the 10 J and 20 J lay further apart from each other and lack linearity. Although the 40 J, 45 J and 50 J impacts show deviations in gradient changes, no clear trend can be detected either. The characteristics of the damage are spread more over the time interval, making analysis and thus judgement harder. Because the level 1 analysis contains the largest frequency component, has the most obvious trends of the pristine signals and the level 2 analysis is more separated, the level 1 decomposition will be used for damage detection at this sampling frequency.

The presented results show that sampling at 100 kHz is sufficiently high to detect impact damages. The type of damage is however not traceable from the data. To research if different types of damages can be detected, the peak frequencies from Figure 2.1 are used. Using this as the basis of damage quantification, matrix cracking is the only failure mode that could be detected with a sampling frequency of 100 kHz. As shown in Figures 5.6 and B.1, matrix cracking has occurred at IL1, primarily at the bottom of the panel.

To check if the algorithm does not detect a false matrix cracking failure mode, IL5 is also analysed. The damage is represented in Figure B.5, in which only a dent is visible. Also, no internal damages have been indicated by the phased array scan. This indicates that no matrix cracking has taken part and the WT should not return large deviations for the 45 J impact, when compared to the 10 J and 20 J impacts. The WT results of IL5 and PZT6 are shown in Figure 5.10, in which can be seen that the signal trends for all levels are the same, indicating matrix cracking has indeed not occurred at these impact levels. It has to be noted that the impacts at IL5 are done with a 1154 g impactor weight. Due to the weight being consistent at this impact location, no further compensations have been made.

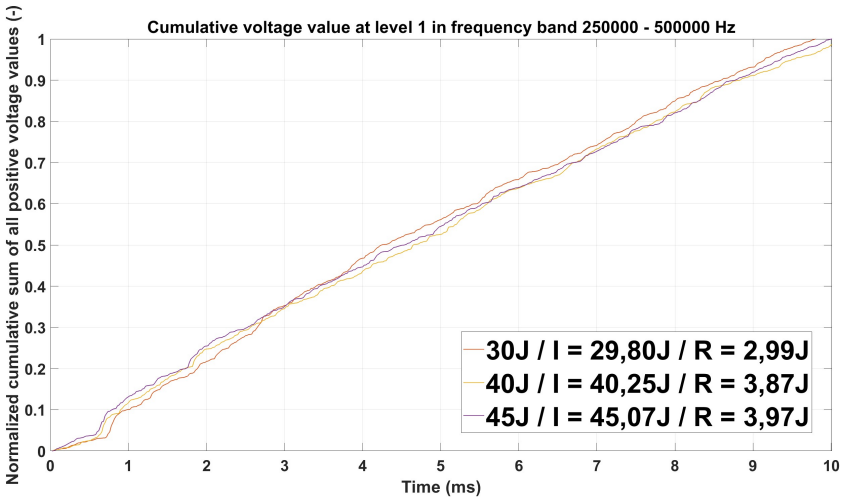

Figure 5.10: WT analysis for IL5 and PZT6

5.2.5. Sub-conclusion

Taking the previous results of the 100 kHz sampling frequency into account, the following sub-conclusions can be made:

- The unprocessed signals indicate damage in the panel, making the hypothesis plausible.
- The use of the STFT has limitations, especially in quantification of the damage. This method does not contribute to damage detection or quantification capability of the developed algorithm and will therefore not be used anymore.

- Damage detection is possible when sampling at 100 kHz. Quantification is limited to matrix cracking due to the Nyquist frequency of 50 kHz and taking the peak frequency responses from Figure 2.1 into account.
- The damage is characterised by a significant gradient change in the WT results when compared to the pristine cases.
- The WT does not return the damage characteristics when the impacted location has no physical and internal damage. This argues the possibility of valid damage detection using the current set-up.
- The higher the impact energy, the longer the WT results deviate from the pristine WT results. As the panel is damaged at the lower energy impact (40 J), the results of the 45 J and 50 J impacts may be affected due to the affected integrity of the panel. The higher decomposition levels also return results with less linearity. The higher the decomposition level, the harder the analysis will be, especially for real-time applications.
- The level 1 decomposition level contains the largest frequency spectrum (25 - 50 kHz), without noise limiting the use of this level. Therefore, the level 1 decomposition level is sufficient when matrix cracking is the failure mode of interest.

Although, a sampling frequency of 100 kHz seems to be sufficient to detect damages, not all damages can be detected due to the specific AE frequency characteristic each different type of damage has. Therefore, additional tests have been performed. The sampling rate has been set to 1 MHz, resulting in fully detecting the frequency components up the the Nyquist frequency of 500 kHz. Now, the FBG data will be used as the sampling frequencies are similar.

5.3. 1 MHz sampling rate data

Increasing the sampling frequency of the PZT sensors, more failure modes in the CFRP should be detectable. Again, basing the peak frequency components of different failure modes on the values in Figure 2.1, damages up to fibre breakage could be detectable. The new tests were on six new impact locations (IL7 - IL12), as stated in the test plan in Appendix A. Due to the large amounts of data, again only one location and one sensor will be fully analysed. Additional analysis will be done on other impact locations for comparison of results. For the full analysis, IL8 is chosen. This location has been impacted gradually increasing the impact energy resulting in much data, but also includes most of the damage modes. For comparison with the results of IL1, PZT6 is the chosen sensor.

5.3.1. Signal responses

As shown in the previous section, the damage characteristics of the signal are primarily in the first 10 ms of the signal. After this, many factors - such as boundary conditions, attenuation and reflections - are influencing the signal and signal analysis will be more difficult. Therefore, Figure 5.11a shows the signals of PZT6 measured from impacts at location 8. Deviations in the signal of the higher energy impacts are marked in the red box. If these deviations are due to damage, first the damage will be confirmed by means of the phased array scan. Second, the WT will be applied for detection and quantification possibilities.

FBGs have also been used for impact response monitoring. In this case, the sampling frequency per sensor is 937.5 kHz, making them comparable to the PZT sensors regarding the data to be measured. The results are given in Figure 5.11b. Unfortunately, the sensor responses do not look similar, but frequency content could be still be available. This will be further analysed in the WT section.

5.3.2. Ultrasonic NDT results

In Figure 5.12 the ultrasonic NDT results, together with a photo of the damage at the top of the panel, is represented. These ultrasonic NDT scans are again obtained by using the Omniscan-M-PA16-128 NDT measuring device. The scan was done after the last 170 J impact, thus showing the damage after all impacts which where increased to the maximum of 170 J at this location. The total damage size is *657* mm^2, containing a dent at the top, internal damages within the outer layers of the skin and a crack

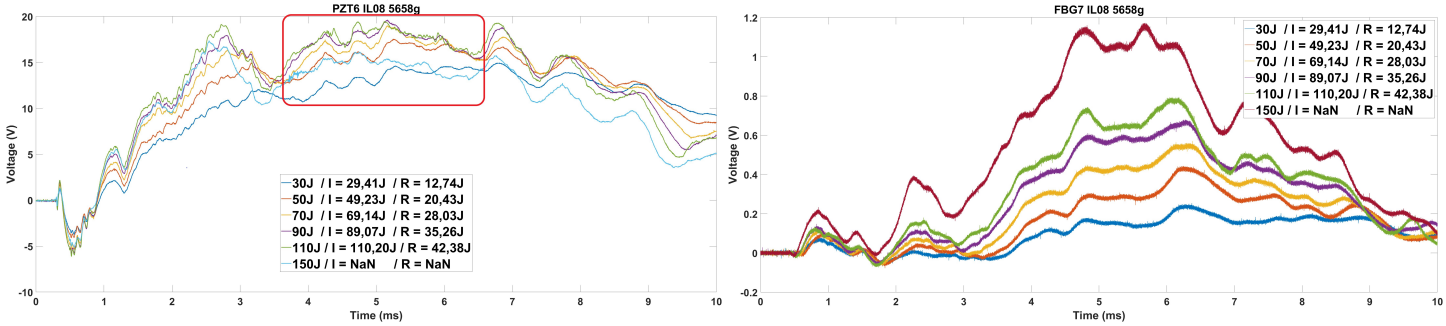

(a) PZT6 IL08 (b) FBG7 IL08

Figure 5.11: First 10 ms of the response signals measured at PZT6 and FBG7 from the 5658g impactor with multiple impact energies, with I being the real impact energy and R being the rebound energy.

at the bottom. Again, the reflection C-scan marks the internal damages, and the attenuation C-scan the damage at the top layer. Comparing the reflection C-scan with the B-scan, it can be clearly seen that internal damages have occurred in the panel, most likely delaminations of the individual plies. The full representation of the damages and the ultrasonic NDT results of all impact locations are shown in Appendix B.

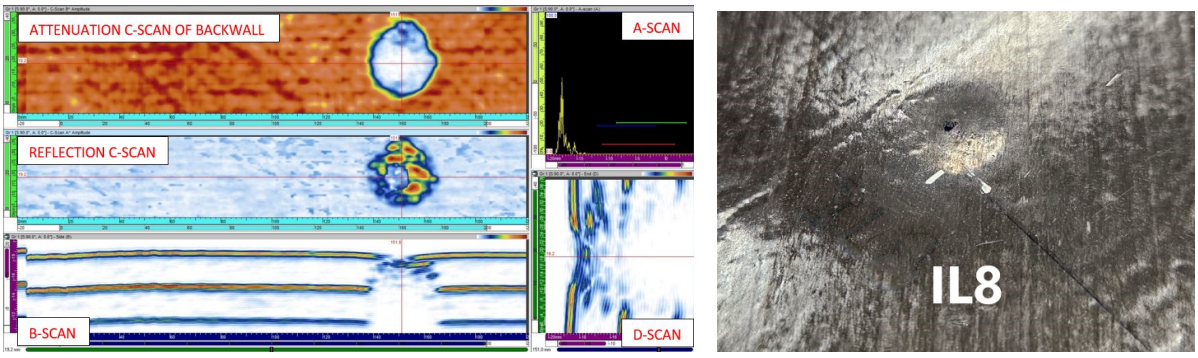

(a) ultrasonic NDT A-, B-, C- and D-scan of the impact location. (b) Dent at the impact location.

Figure 5.12: Damage at IL8 at 170J with an impactor mass of 5658g.

The internal damages at IL8 are similar to the damage at IL1. The main differences are the damage sizes and the surface damages. Due to the very high impact energies applied at IL8, the ultrasonic NDT results return more significant damage than the scans at IL1.

5.3.3. Wavelet transform

Because the sampling frequency of the PZT sensor system is increased compared to the previous results, the decomposition levels of the WT also represent other frequency bands. This also means that the failure mode for matrix cracking is not in level 1, but mainly in the level 5 decomposition. For IL8, the full WT results up to a level 5 decomposition are shown in Figure 5.13. Level 1 indicates fibre failure, level 2 fibre/matrix debonding, level 3 delamination and level 5 matrix cracking, based on the frequency bands in this analysis. Although the level 4 decomposition returns damage characteristics, the frequency envelope overlaps two composite failure modes. This should be prevented as much as possible, due to the difficulty in linking a failure mode to a frequency response. Therefore, in this particular case, only the level 3 and 5 decomposition levels are used. The level 2 decomposition also contains a frequency band in which both delamination and fibre/matrix debonding can be detected. It is chosen to still use this level, as the level 3 analysis is only detecting delaminations. With this knowledge, frequency responses in the level 2 analysis can be linked to delamination or fibre/matrix debonding events.

Looking at the level 1 decomposition, the noise value seems to be the dominant frequency component.

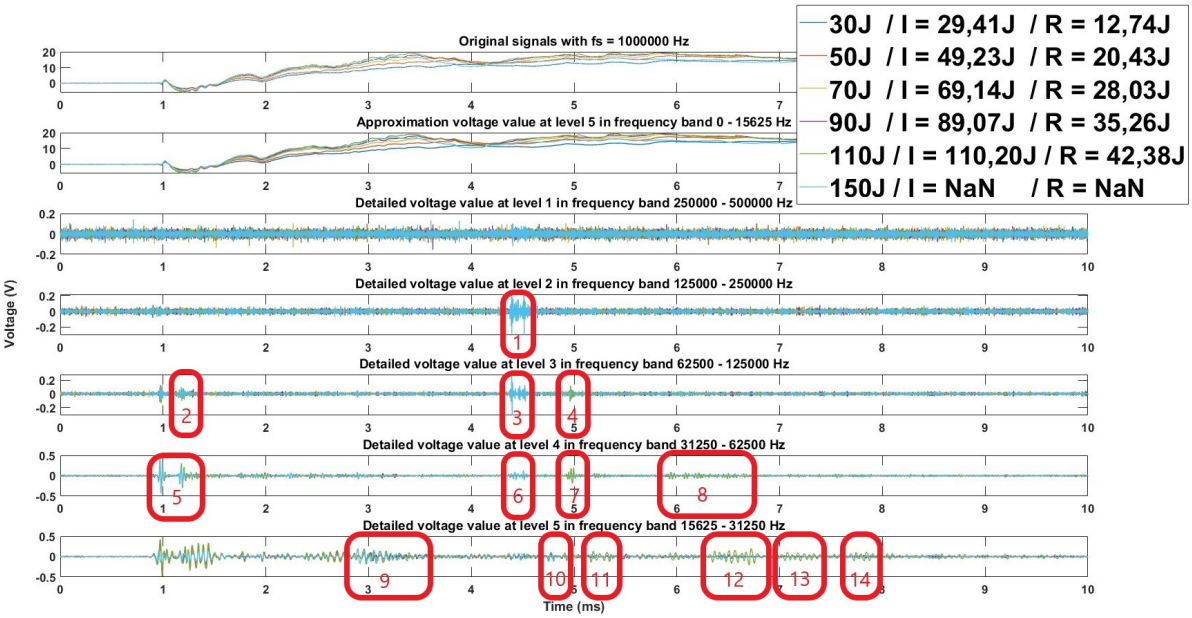

Figure 5.13: Original signals with their corresponding WT plots for IL8 and PZT6 using the db5 wavelet.

Damages that have occurred upon impact, may not have sufficient frequency components and could therefore be masked by the noise level. Another reason no additional frequency components are visible, is that there may not be any damage within this frequency range (e.g. fibre failure). For the lower decomposition levels, noise is still available, but is not the dominant frequency component. Deviations in all levels are marked with the red boxes, indicated by the numbers 1 to 14. Again, these deviations are difficult to compare with the signals of other impact energies. Therefore, the positive values at each level are cumulatively summed up and normalized. For IL8, this leads to the results as shown in Figure 5.14. The highlighted area's in this Figure are colour coded in the same colour to its corresponding impact energy.

As the ultrasonic NDT results are again done after the last highest impact energy test, it is not clear at which impact energy the first detectable damages started to occur. This means that the exact pristine signals cannot be defined. Although this is the case, it can be seen that the signals up to 70J have similar trends. Therefore, the signals of 30J and 50J will be classified as the pristine signal responses, at which no damage has occurred due to impacts. Looking at the level 1 decomposition, where fibre failure should be detectable, no signal features are present indicating this failure mode. Again, this can be due to the noise masking damage features in the signal, or fibre failure has not occurred. The level 2 decomposition shows a strong deviation in slope at around the 4.5 ms after ToA. However, the WT results seem to be present due to an inexplicable response within the original signal. If this is due to a damage, or due to a sensor malfunction, cannot be clarified anymore. Therefore, the WT results of the 150J data will be highlighted, but will not be further used in drawing conclusions. Lacking further deviations in the gradient of the WT in the level 2 decomposition, indicates that fibre/matrix debonding has not occurred with impact energies lower than 150J.

Nevertheless, the 90J and 110J impacts show a deviation in the gradient right after the ToA in the level 3 decomposition. This region is marked with the red box. Also, the 110J impact shows a deviation in the signal at around 5 ms. At this level, delaminations should be detectable, for which the 90J impact energy shows the first evidence of this failure mode. For the 110J impact, additional characteristics are present later in the signal. When looking at matrix cracking in the level 5 decomposition, it is evident that the 110J impact leads to a significant drop in energy right after ToA. The other lower energy signals follow a similar trend, meaning that matrix cracking did not occur at these lower impact energy levels.

For further analysis, other impact locations can be used. IL9 has similar damages as IL8, but is only

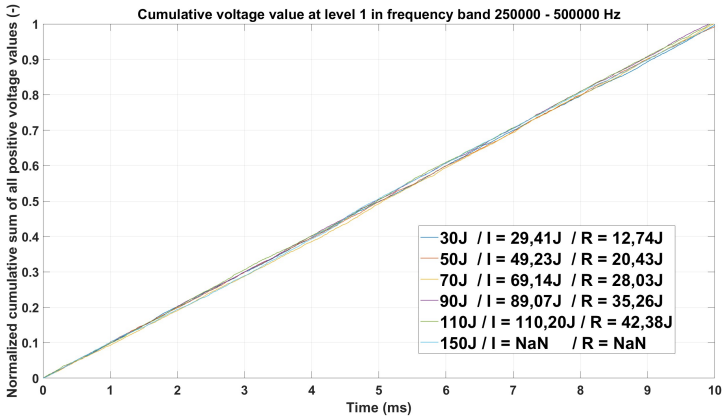

(a) Cumulative voltage value at a level 1 decomposition for PZT6 at IL8.

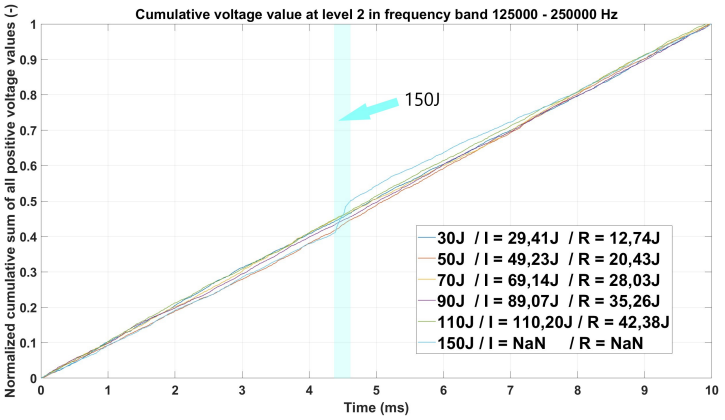

(b) Cumulative voltage value at a level 2 decomposition for PZT6 at IL8.

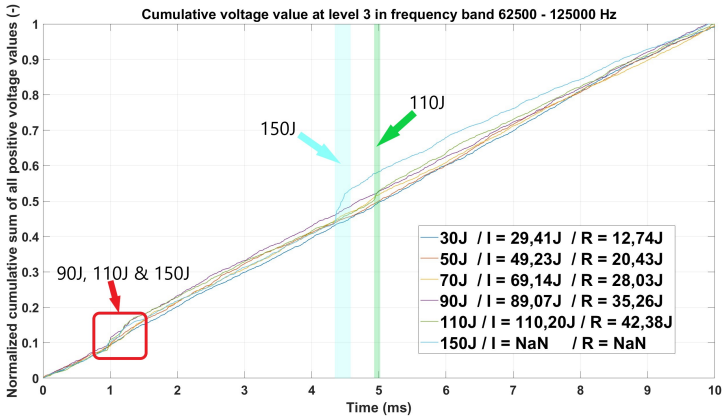

(c) Cumulative voltage value at a level 3 decomposition for PZT6 at IL8.

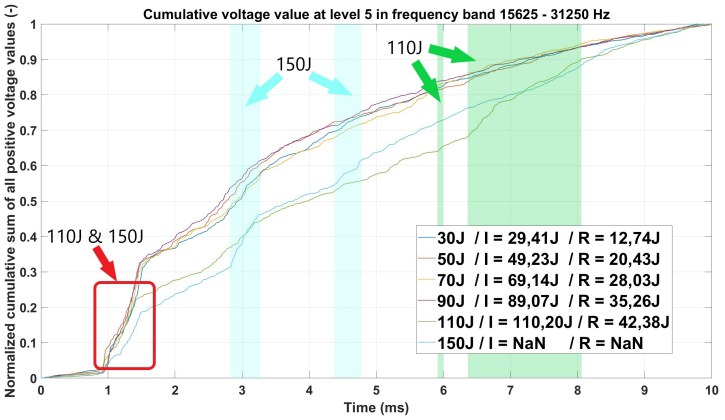

(d) Cumulative voltage value at a level 5 decomposition for PZT6 at IL8.

Figure 5.14: WT analysis for IL8 and PZT6

impacted with 2 impact energies. For larger impact damages, IL11 will be used. IL12 will be further analysed due to the penetration event.

IL9

The physical damage at IL9 can be examined in Figure B.9. The ultrasonic NDT was performed after the 130J impact, for which the damage is confirmed. The 50J impact is considered the pristine impact case. What can be seen, in contrast to the analysis at IL8, is that the level 1 analysis does return two sections in which a slight deviation in the slope is observed. This difference can be explained by two possible outcomes. The first is that due to multiple impacts at IL8, the panel has been damaged step by step, limiting the abrupt damage growth when a sudden high impact occurs. This results in damage growth that is not picked up by the sensors (above the noise level) and thus analysed by the algorithm. The other possible reason is due to the slight stiffness difference between IL8 and IL9. The level 2 analysis shows two regions at which the slope is different compared to the pristine case. Also, right after ToA at the sensor, the energy through the panel at 130J is lower than that of the 50J impact, indicating energy is not propagating through the panel but initiating the damage. At this decomposition level, the detectable failure mode is fibre/matrix debonding. Due to the energy release during the physical debonding, the gradient in the slopes increase during a small time bracket. The level 3 decomposition shows similar results to the level 2 decomposition. This behaviour is also similar to the analysis at IL8, making the damage detection and quantification more plausible. The main difference to the level 2 decomposition, is that the energy drop between the 1 and 4.5 ms is larger at the level 3 decomposition. This indicates that more energy is required for a delamination event to occur. The level 5 decomposition shows a big energy drop just after the ToA at the sensor. Eventually the WT follows the trend of the pristine case, after which many deviations in the gradient of the WT start occurring.

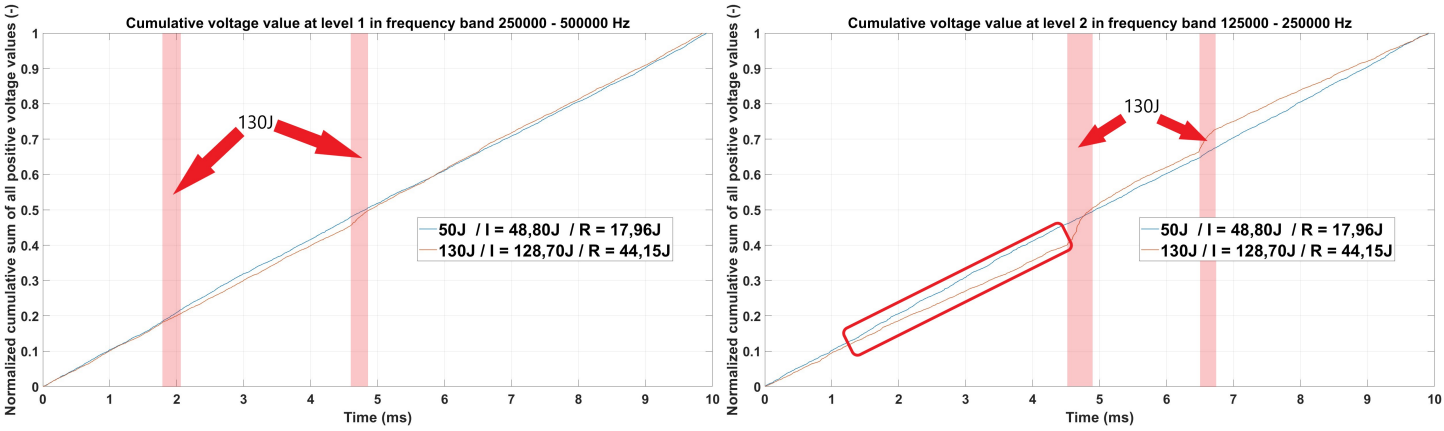

(a) Level 1

(b) Level 2

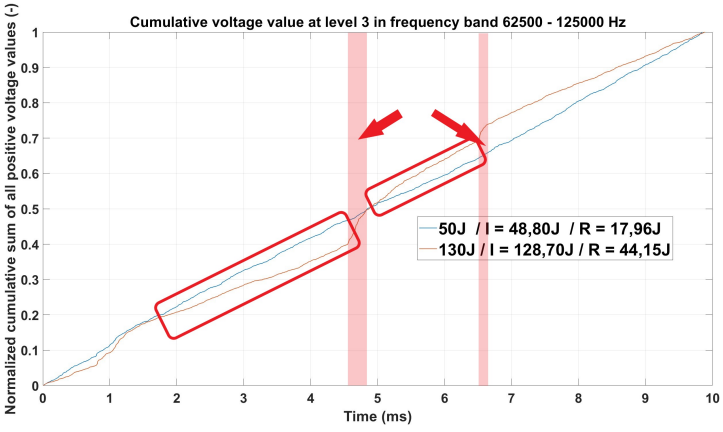

(c) Level 3

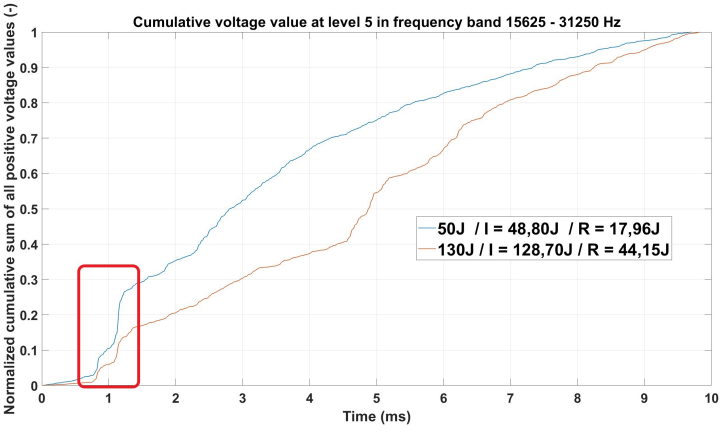

(d) Level 5

Figure 5.15: WT analysis for IL9 and PZT6

IL11

At IL11 the 100J impact has lead to a near puncture near the boundary conditions of the panel. The overall damage of this impact location is shown in Figure B.11. This location consists of at least delaminations, fibre failure and matrix cracking. An impact damage such as this, affects the structural integrity and must be detected by the algorithm. When comparing this damage to the damage of IL8 and IL9, the damage is more significant. The WT decomposition results for IL11 are shown in Figure 5.16. From these results, it can again be seen that in all levels, the algorithm can detect the damage. Also, the trends in the WT results are similar to the IL9 WT results. The big difference, is that the extent of the signal deviations are much larger, especially in the levels 2 and 3, compared to the similar levels at IL8 and IL9. Linking this to the damage size, the amount of damage induced by the impact is visible as larger gradient changes. When only looking at the pristine case of IL11, again a linear trend is shown in the levels 1, 2 and 3, where level 5 primarily deviates in trend. The damage extent of IL12 is larger than that of IL11, to which the trends of IL11 can be compared with.

IL12

IL12 has the largest damaged area of all impact location on the flat panel. The damage is shown in Figure B.12. From both the physical survey as the phased array scan, it is obvious all four failure modes for a composite material have taken place. When looking at the decomposition levels 1, 2 and 3, again there is a linear trend for the pristine cases. When the damage impact occurs, there is a large gradient change in all three levels. The extent of this gradient change is also more abrupt when compared to IL8, IL9 and even IL11. This means that indeed the amount of damage is visible in the WT as abrupt changes in the gradient, as highlighted in Figure 5.17. The level 5 decomposition shows a similar trend between the pristine and damaged case, where the largest deviation in the signal is present right after

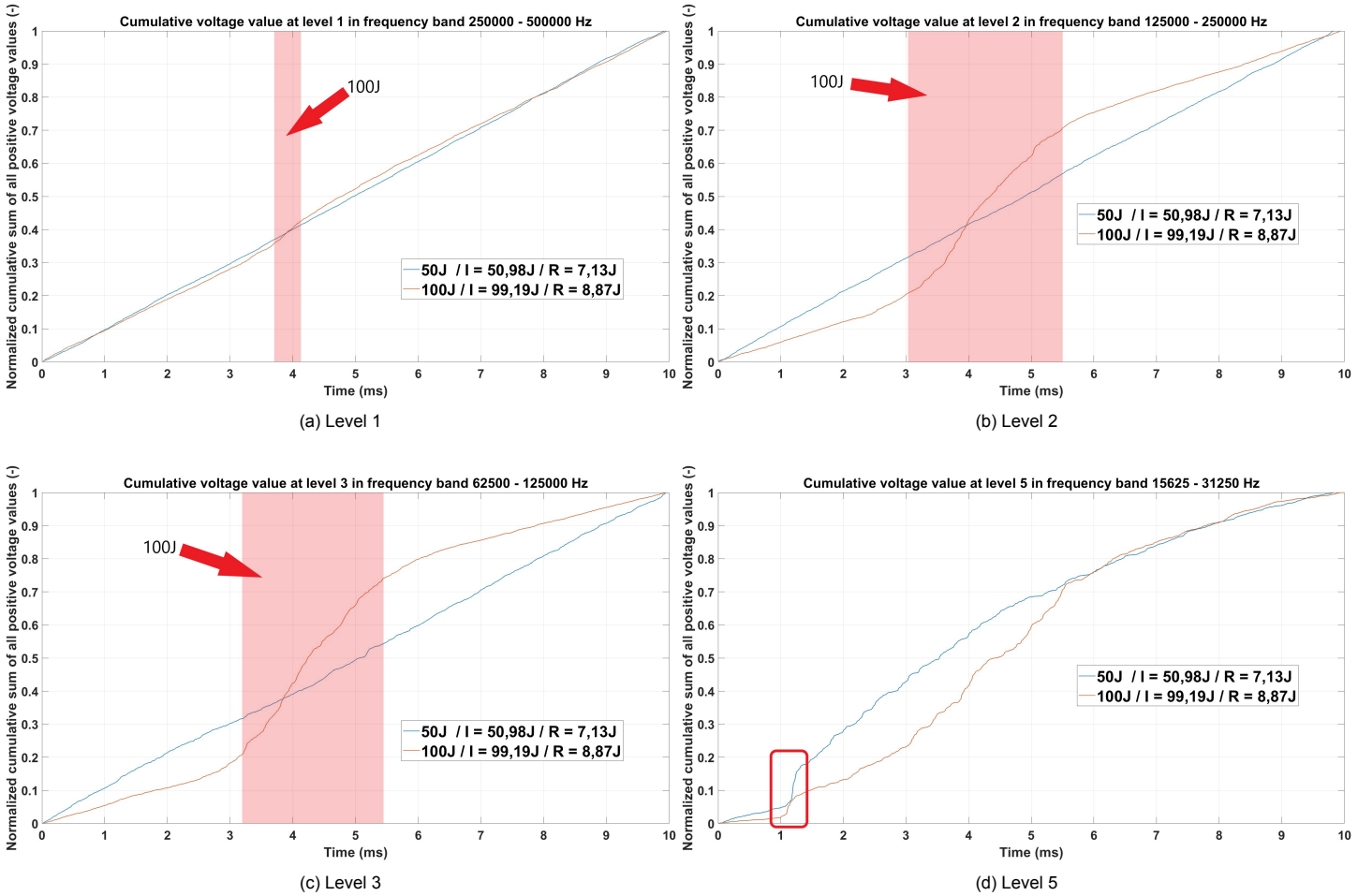

(a) Level 1 (b) Level 2

(c) Level 3 (d) Level 5

Figure 5.16: WT analysis for IL11 and PZT6

the ToA at the sensor. Here, the energy values is lower, compared to the 20J pristine impact. This characteristic is present in all the analysed impact locations thus far. Again, linearity is not present at this level, making it a harder failure mode to detect in a real-time impact damage monitoring system.

Sub-conclusions

From the above analysis, some sub-conclusions can be made. The first overall conclusion, is that for all impact locations, containing only two impacts or multiple increasing impacts, the damage is detectable in each defined decomposition level. This means that the damage detection capability also works for the data sampled at 1 MHz. Although IL8 has gradual increasing impact energies, the analysis lead to limited detectability. Therefore IL9 was also analysed, as this location was near IL8 and had similar damages. IL11 and IL12 were analysed to determine if the extent of damage was also visible in the WT. Per decomposition level, some specific sub-conclusions can be made due to the previous analysis and are discussed below.

Level 1 - Fibre failure Overall, fibre failure seems to be detectable by the developed algorithm, indicated by a gradient change in the WT. Especially in the cases where fibre failure was evident or plausibly available, the algorithm returned clear indications in the gradient of the WT. This counts for the impact locations 9, 11 and 12. When looking at IL8, fibre failure seems less likely and may not have occurred. This is also demonstrated by the WT results up to 110J. These results make it very plausible that this method allows for a reliable damage detection potential when looking at fibre failure mechanisms. Also, the larger the damage size, the more the gradient of the damaged case deviate from the pristine case, making the potential of detection higher. The pristine cases show a near linear trend, beneficial for threshold determination and therefore real-time impact damage monitoring.

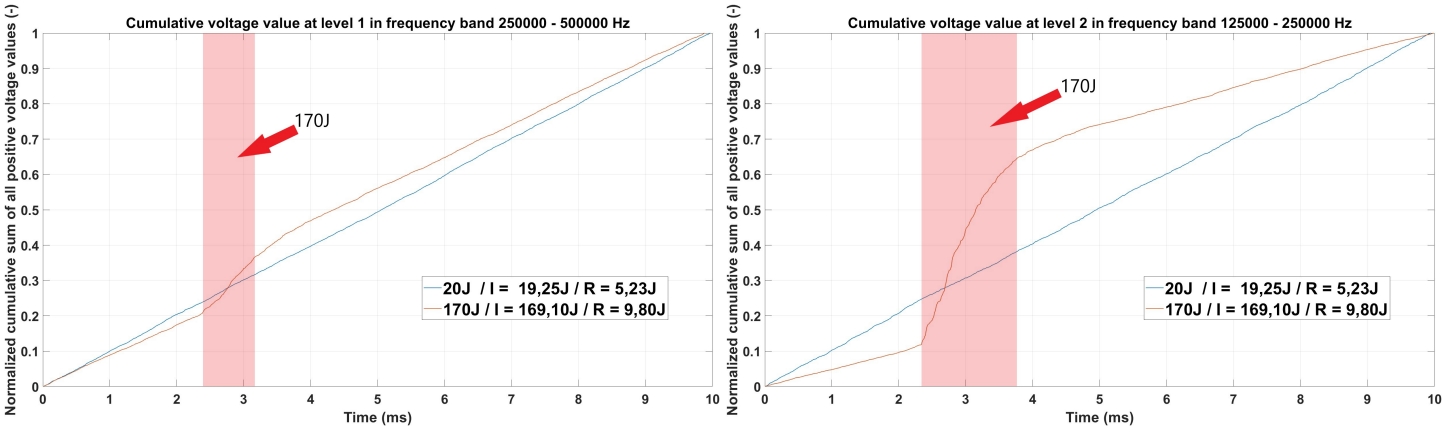

(a) Cumulative voltage value at a level 1 decomposition for PZT6 at IL12.

(b) Cumulative voltage value at a level 2 decomposition for PZT6 at IL12.

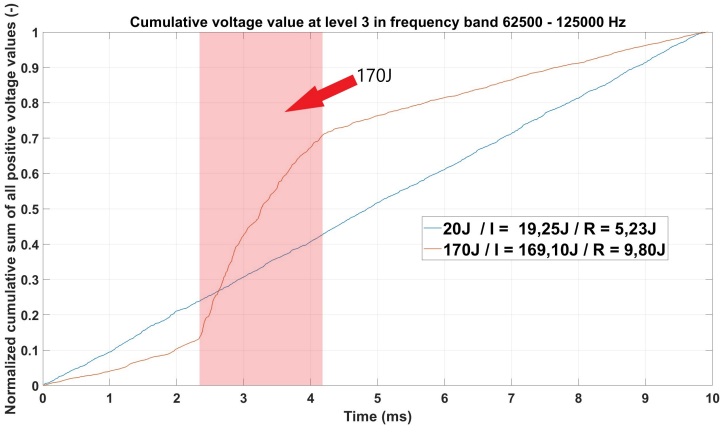

(c) Cumulative voltage value at a level 3 decomposition for PZT6 at IL12.

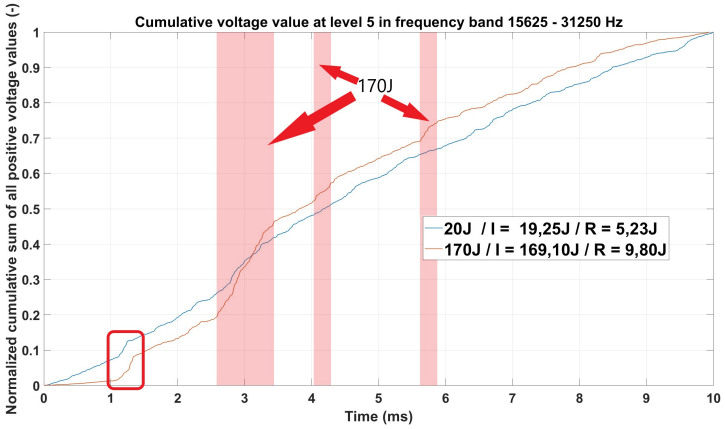

(d) Cumulative voltage value at a level 5 decomposition for PZT6 at IL12.

Figure 5.17: WT analysis for IL12 and PZT6

Level 2 - Fibre/matrix debonding At all previous analysed impact locations, the algorithm detected damage by means of a gradient change in the normalized WT results. The first indication of damage detection within this decomposition level was at IL8, where the origin of the signal response was debatable. How,ever IL9, IL11 and IL12 showed clear gradient changes when compared to the pristine impact cases. The larger the damage size, the steeper the gradient change of the WT. This also means that the damage detectability increases when the damaged area's are larger. Sufficient sensitivity of the sensor systems is thus required to detect certain impact damage events, especially at lower impact energy level. Similar to the level 1 decomposition, the pristine cases show a linear trend.

Level 3 - Delamination The algorithm was successful in detecting delaminations. For IL8, the detectablility was both evident at the beginning of the signal (right after ToA at the sensor) as half the time range analysed. When looking at IL9, IL11 and IL12, the deviations were mainly detectable at around half the time range and had a different trend as IL8. Although the trends from these impact locations are different to the IL8 results, especially at the beginning of the signal, detection of damage was possible in all cases. At all locations, the gradient change in the WT results were signal features relatable to delaminations. Identical to the level 1 and 2 analysis, is that the larger the damaged area, the larger the gradient change of the damaged WT results. At this level, linearity is also still present, but is lesser in amount than in the level 1 and 2 decomposition.

Level 5 - Matrix cracking When looking at the matrix cracking failure mode, the results of all impact locations show clear deviations right after the ToA at the sensor for the damage cases. Furthermore, changes in the slopes are present at all impact locations, where IL8 and IL12 show the most similar trends in the signals. The changes in the gradient of the WT results are therefore also marked with the

coloured boxes. When looking at IL9 and IL11, this trend however lacks, where the only similarity of the signal is present right at the ToA at the sensor. Different from the level 1, 2 and 3 decompositions with these impact locations and method, no statement can be made about the damage area and the detectability of the damage. At this level, linearity is not present at the 1 MHz data, as well as a clear trend over all the impact locations. Determining a threshold for real-time application is therefore difficult. However, the 100 kHz data did show linear behaviour in the WT results.

Overall, the damages induced on this flat panel, with the used test set-up and the applied algorithm, the damages are detectable at all levels. Using the peak frequency responses, the damage can be quantified, leading to detection of specific types of composite failure modes. The lessons identified from the flat panel tests, such as the lack of ultrasonic NDT results and the non-consequent increase in impact energy, will be taken into account for the tests on the stiffened panel, described in the next chapter.

FBG

During testing, the FBGT sensor system was also installed. As stated in the literature review, PZT and FBG sensors should return similar (strain) sensor results. Therefore, the WT of the FBG sensor data should return the same results as the PZT data. To confirm if this is true, the WT of FBG7 at IL8 will be performed. The results are shown in Figure 5.18.

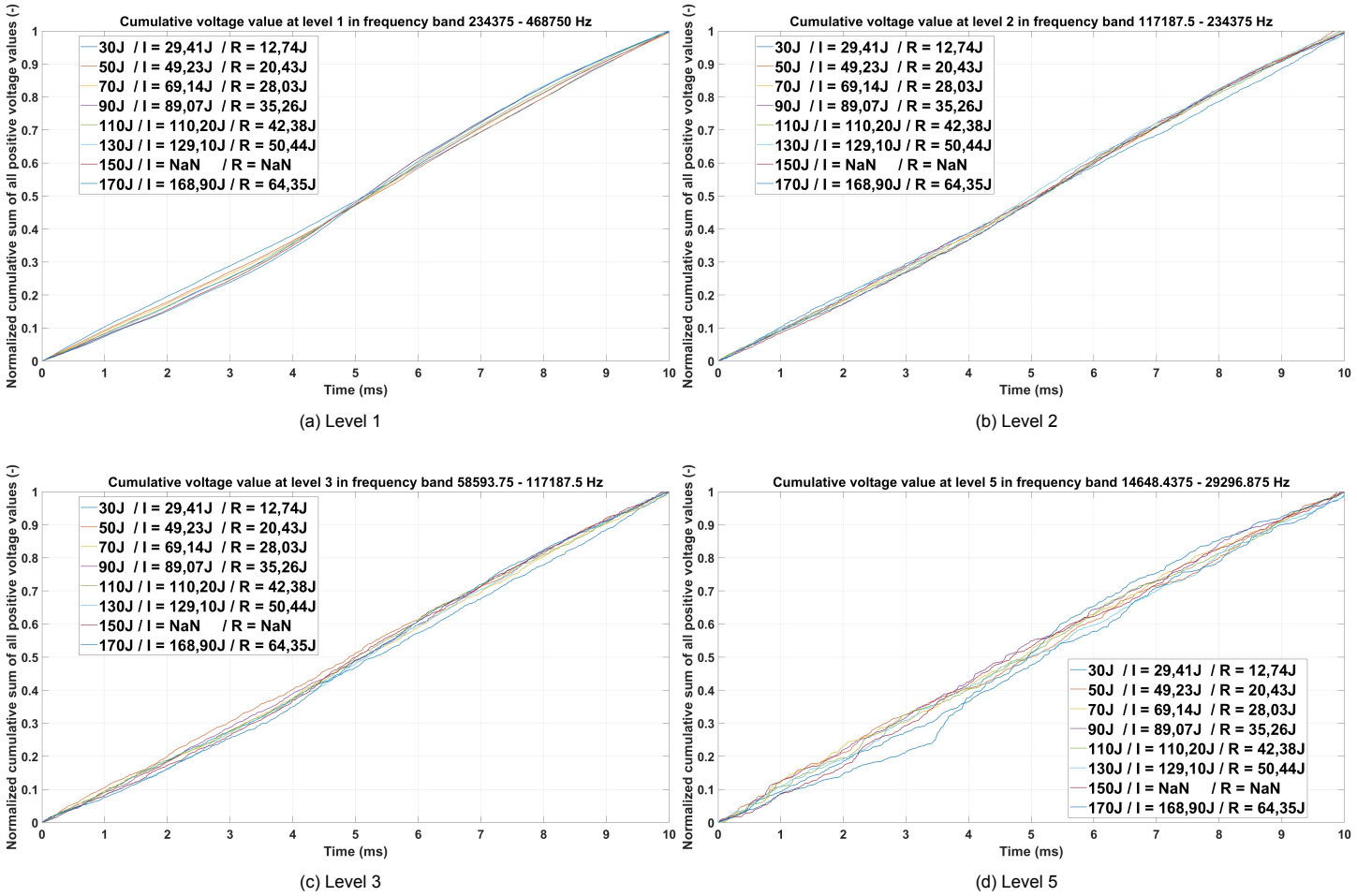

(a) Level 1

(b) Level 2

(c) Level 3

(d) Level 5

Figure 5.18: WT analysis for IL1 and FBG1

Unfortunately, the FBG results do not show any indication for damage. All trends are (nearly) linear and the signal features for damage are missing. Therefore, using the current FBG set-up, damage detection and quantification is not possible. As discussed at the beginning of this chapter, the FBGT

system is not fully developed yet. Data loss during measurements, high noise level and cross-talk of the sensors are problems which need to be solved before additional tests can be performed. More details will be given in paragraph 6.2.3.

5.4. Conclusion

The in depth signal analysis of the flat composite panel, using the WT algorithm, allows for answering the second research sub-question, stated as; "*What signal features in the response signal of a simple composite plate are representative for an impact damage and can these features be related to a certain type of damage being present after an impact event?*". The conclusion, in which the sub-question is answered, is formulated below.

During the performed signal analysis, multiple sampling frequencies of the PZT monitoring system were analysed. Initially, the unprocessed signals were analysed for indications of damage at the higher impact energies. To determine if damage was present, ultrasonic NDT were performed. Taking these results into account, the STFT was used to find the regions in which the frequency spectrum changed due to damaging impacts. These results were not sufficient for decent detection, lacking resolution in time and frequency, but also not clarifying in which frequency regions damage was present. Therefore the wavelet transform has been used to further analyse the signals, with both higher resolution in both time and frequency. Using the DWT with a db5 wavelet, damage detection is possible for both the 100 kHz as the 1 MHz sampling frequency results of the PZT sensors.

For the 100 kHz data, quantification is done by using predefined peak frequency ranges for the most common failure modes in composite materials. Based on this, matrix cracking can be detected in the level 1 decomposition. The **main feature representative for matrix cracking**, is a significant gradient change in the WT when compared to the pristine cases.

For the 1 MHz PZT sampling data, multiple failure modes can be detected. This research has shown that the level 1, 2, 3 and 5 decompositions **return the damage characteristics of respectively fibre failure, fibre/matrix debonding, delamination and matrix cracking** based on their frequency band. For fibre failure, fibre/matrix debonding and delamination, mainly deviations in the gradient of the WT are representative for the damage. The higher the larger the damage, the steeper and more abrupt these gradient changes are. Evidence of energy differences were also visible at regions where the signals diverged from each other. In these levels, the pristine cases showed a linear trend. For matrix cracking, the main feature is a clear drop in energy right after ToA at the sensor, evident by a lower value of the WT voltage value. Also, gradient changes in the signal are present for this failure mode. Linearity however is not present at the decomposition level using the 1 MHz PZT data.

Furthermore, an optical monitoring system has been used, which allows to sample at 937.5 kHz at each FBG. This system unfortunately was not capable of detecting damages. Improvements to the system were made for application on the stiffened panel.

5.5. Observations and lessons learned

In this chapter, the damage detection capability is of the WT is tested on a simple unstiffened composite panel. From these tests, some choices and assumptions have been made. These factors will be briefly discussed in this observation and lessons learned section.

- For these tests, a simple composite panel has been used. This panel is not representative for a skin panel as used in real aircraft. Using this panel, has given multiple insights in understanding the use of different types of sensors, effect of impacting at low and high energies, limitations of the test set-up, boundary condition performance, ultrasonic NDT measurements and understanding the initial indications of damages being present. Multiple tests have been performed on this panel, where the integrity of the panel may have been affected gradually during these tests. This has not been accounted for in the test plan or in the evaluation of the results. Also, lacking the amount of ultrasonic NDT scans has made it impossible to determine at which impact energies the first damages have started to initiate. Therefore, no clear comparison can be made between the WT

values and the ultrasonic NDT results and therefore making it more difficult to draw conclusions. This has to be taken into account during the impact tests on the stiffened panel.

- During the first impact tests, some wrong assumptions about damage in the panel were made. The ultrasonic NDT results did return damage indications, but were not interpreted as such. Therefore, the locations were impact with even higher impact energies, resulting in large damages. Also, during the high impact energy tests, the panel hit the steel table due to the amount of deformation. To prevent this for the following impacts, the panel was lifted slightly and therefore changed the test set-up slightly. This change has not been accounted for in the results.
- As the tests were performed on different days, the set-up has been changed from position multiple times. This may have had effect on the boundary conditions, panel clamping to the steel table and the software/hardware settings (although the latter was mostly kept the same).
- The peak frequencies of composite failure modes have been taken from literature, but have not been verified during testing. The phased array scan has provided insight in damages being present and together with physical surveys, some failure modes are observed. The performance of this algorithm can be improved by doing additional damage characterisation, by means of ultrasonic NDT, where a more reliable statement of damage features can be extracted from the signals. There is thus a uncertainty in the results regarding the damage features, but it does give an initial indication.
- Due to the limitations of the test set-up, multiple weight changes have been executed. This makes results comparison of these different impactor weights more difficult. Weight changes should thus be limited, as less variables in the test set-up increase its integrity. Additional tests can be performed to determine the effect of weight on damage detectability.
- The effects of higher impact masses on the dominant wave modes have not been taken into account in the analysis. Also, no research has been done on identifying which wave modes (symmetric or anti-symmetric) are mainly present in the signal. For this thesis, that has been a well-considered decision, as for impact during service the choice of wave modes is also not defined.
- The FBGT interrogation system has not shown similar results as the PZT measuring system. During the tests on the flat panel, software and hardware issues (both in the interrogator as in the fibres), have lead to these insufficient results. Influence of for instance sensor angles and distances could not be further analysed. After these tests, some improvements in software (LabView) were made, so the system could be used again for the additional tests on the stiffened panel. The FBG sensors have a high noise level, which may mask any damage features that are present. Also, data loss causes many signal to not be usable.
- The damage size calculations of the panel are indications and not exact values. The damage size is determined by the area of damage detected by the phased array scan.
- Only the positive voltage values have been used for the WT classification. Another possible method was to use the absolute values of the WT, incorporating the negative WT values in the analysis.
- IL8 was not the best location for damage detection analysis, but was the only location with multiple impact energies. The 150 J impact energy seems to be unreliable. Therefore, additional impact locations have been analysed, which lead to more comparable and representable results.

6

Wavelet transform analysis on complex composite structures

"How do the defined signal features from the simple composite square panel compare to a complex stiffened composite panel and what influence do the measurements over thickness steps and stiffeners have on the damage detection and quantification possibilities of the algorithm? "

6.1. Method

As defined in the research question, this chapter will focus on the comparison of the flat panel and stiffened panel WT results. To accommodate the comparison, additional tests on an aerospace grade stiffened composite panel are performed. For the tests on the stiffened panel, no test plan has been fully described, but the testing conditions will be briefly discussed in this method section. As the stiffened panel is an aerospace grade structure, this specimen is more representative for a fuselage section of an aircraft. The panel is made of the same ASD4-PEKK material as the tested flat panel and contains two thickness deviations along the length and has three stiffeners over the length. Each ply has a thickness of 0.138 mm. After each thickness step, the lay-up changes. During the impact tests, the panel is clamped between fixed boundary conditions and is fixed on a rigid steel table which provides a steady basis. Between the boundary conditions, the panel is free to move due to the impacts. A schematic overview of the panel clamped in the boundary conditions, is shown in Figure 6.1.

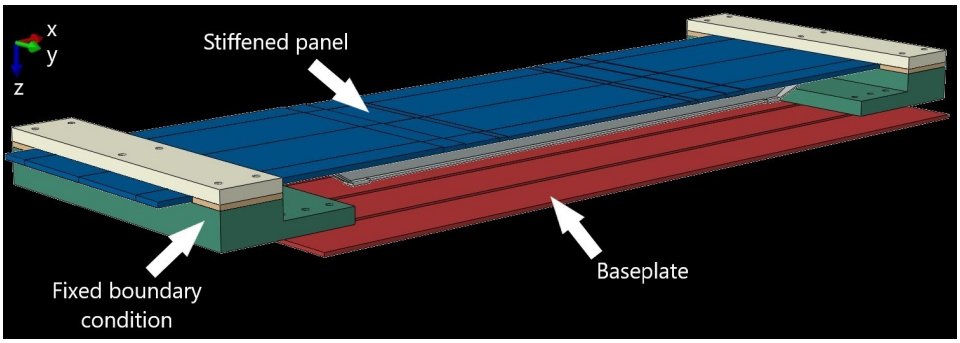

Figure 6.1: Stiffened panel schematic test set-up overview.

To measure the impact responses, two sensor networks were installed on the panel. The first system consists of 6 PZT sensors, sampling at 1 MHz for each sensor. The second sensor network consists of 8 FBG sensors, sampling at 937.5 kHz for each sensor. The interrogators, hardware and software have been kept the same as those of the flat panel tests. The software settings have been slightly adjusted for good measurements. The impact locations have been thoughtfully chosen, of which five locations have been impacted. The first impact location (IL1) is in the center of the panel, within two stiffeners.

This location allows for a good analysis of how the signals react propagating through different thicknesses of the panel. Also, due to the selected sensor position, the effect of stiffeners can now be easily analysed. The second impact location (IL2) has been chosen to impact on a stiffener. The third impact location is at the center of the first thickness drop, which allows the gathering of information on how these regions react to impacts. The fourth impact location (IL4) is in the center of a thicker part of the panel, also making it possible to analyse propagation through different thicknesses. The last impact location (IL5) has been chosen as a location to fully damage the stiffener, impacting it at its weakest spot. The impact and sensor locations, including the sensor orientation, is shown in Figure 6.2. The locations in the defined coordinate system are shown in Table 6.1.

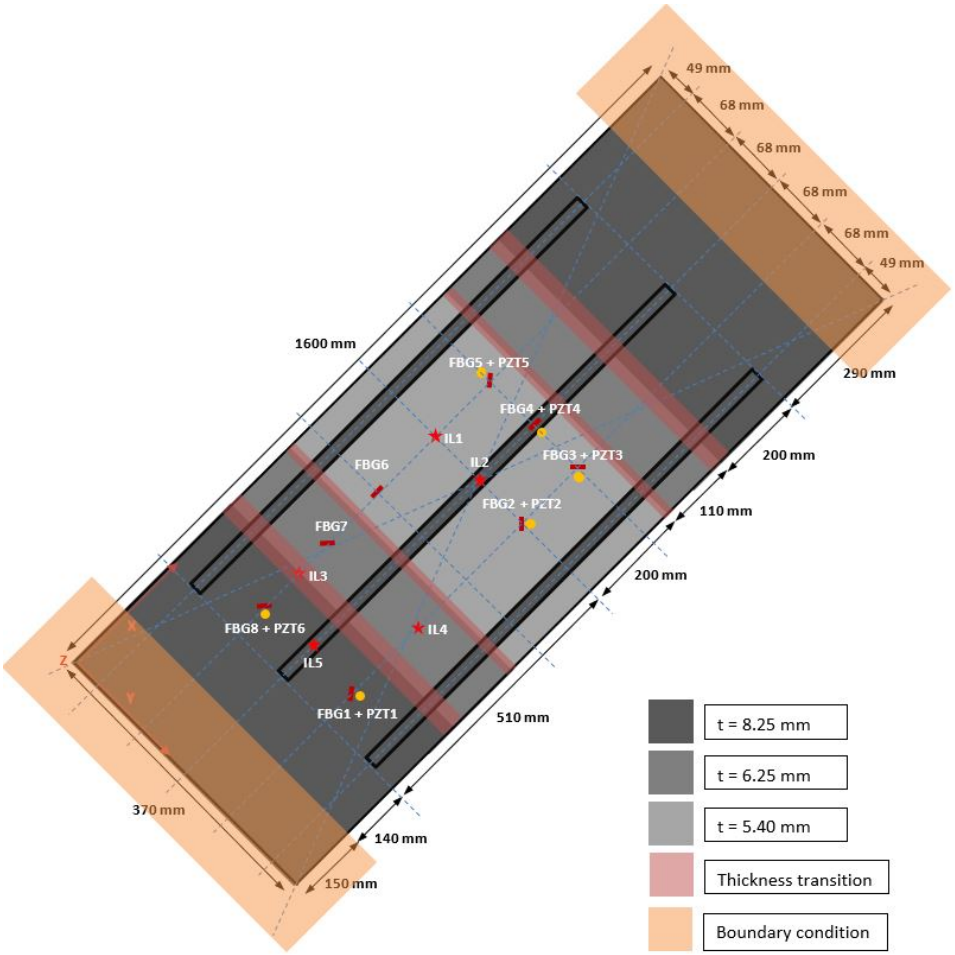

Figure 6.2: Stiffened panel impact test, schematic overview.

To quantify the damage after every impact, an active phased array scan is performed at every location. The steps in impact energy increase is 5 J. This has been done for IL1 to IL4, up to 60 J. This data allows for a valid distinction of damaged and undamaged sensor data. As defined in Section 5.3, four levels in the wavelet transform will be used for damage detection and quantification. For quantification the peak frequencies of Figure 2.1 are again used as basis for damage quantification. This means that level 1 shows fibre failure features, level 2 an overlap between fibre-matrix debonding and delamination, level 3 delamination and level 5 matrix cracking. The level 4 decomposition is again not used, due to the overlap in frequency of two failure modes.

To answer the research question, IL1 is chosen for the in depth signal analysis. Due to the sensor positioning and impact location definition, some additional analysis on signal features can be performed. First PZT5 will be used, as the signal has the least amount of obstacles during propagation towards this sensor. The sensor is placed on a section with the same thickness as the impact location and is

Table 6.1: Sensor and impact locations for stiffened panel.

	x-location (mm)	y-location (mm)	Sensor angle (degrees), angle measured from x-axis	Nominal wavelength FBGT (nm)	Channel number FBGT
FBG1	*420*	*428*	*-45*	*1514.16*	*11*
FBG2	*810*	*245*	*-45*	*1519.47*	*8*
FBG3	*955*	*244*	*45*	*1543.76*	*3*
FBG4	*947*	*197*	*0*	*1548.40*	*7*
FBG5	*953*	*130*	*-45*	*1553.49*	*2*
FBG6	*687*	*123*	*0*	*1558.22*	*6*
FBG7	*555*	*123*	*45*	*1563.02*	*1*
FBG8	*420*	*130*	*45*	*1568.37*	*5*
	x-location (mm)	**y-location (mm)**	**Sensor angle (degrees), angle measured from x-axis**	**Channel number PZT**	
PZT1	*428*	*255*	*-45*	*CH1*	
PZT2	*818*	*252*	*-45*	*CH2*	
PZT3	*945*	*250*	*45*	*CH3*	
PZT4	*945*	*187*	*0*	*CH4*	
PZT5	*945*	*125*	*-45*	*CH5*	
PZT6	*427*	*125*	*45*	*CH6*	
IL1	*816*	*124*	-	-	
IL2	*818*	*182*	-	-	
IL3	*491*	*123*	-	-	
IL4	*559*	*252*	-	-	
IL5	*428*	*188*	-	-	

also closest to the impact location. This analysis will be classified as the baseline analysis, after which the influence of thickness steps and a stiffener can be compared. PZT6 is used for the thickness step analysis, as the signal passes through two thickness step regions in the panel before arriving at the sensor. The effect of the stiffener is analysed by using PZT2. Here, the stiffness of the stiffener has a direct effect on the wave propagation towards this sensor. To determine what effect impacts have on stiffeners, IL2 is the chosen location. IL2 is directly at the center of the panel above the central stiffener. The chosen sensor is PZT4, also directly placed on the stiffener. Because after each impact a phased array scan is performed, pristine signals can now be exactly determined. For IL1 the 40 J and 50 J impact energy signal responses are classified as undamaged. At IL1, the first damage found by the phased array scan was at 55 J, which means that this impact energy will be classified as the damaged signal. IL2 shows its first internal damage after a 70 J impact. Therefore, this impact energy is classified as damaging. The response signals of the 30 J and 40 J signals are defined as undamaged reference signals, based on the phased array scans. In Appendix B.2, the phased array scan results, together with the damage sizes, are shown for IL1 to IL4.

During the data processing, some data has not been taken into account due to measurement errors or sensor failures. These signals are excluded from the analysis, of which the details are given in Table 6.2

6.2. Results

This Section will describe the obtained results including the impact damage detection and quantification analysis. First, IL1 is analysed taking three structural features into account for impacts occurring on a skin section. This being signal propagation in equal thickness skin, propagation through thickness steps and the effect of a stiffener. Also, higher energy impacts are discussed. After this analysis, IL2 is discussed, at which the effect of impacts on a stiffener is analysed. These two sections are based

Table 6.2: Corrupt signals from the impact tests on the stiffened panel.

IL [#]	Impactor weight (g)	Signal deviations
1	2328	PZT1 to PZT6 65J whole signal corrupt
2	2328	PZT1 to PZT6 55J whole signal corrupt PZT5 30J whole signal corrupt
3	2328	PZT6 60J whole signal corrupt
4	2328	-
5	2328	-

on PZT data. The last analysis is done using the FBG data.

6.2.1. Damage detection and quantification on a skin section

Baseline analysis

For the analysis of the signal propagation through unchanged skin thickness, the plots in Figure 6.3 will be used. Figure 6.3a shows the response signals of the pristine impacts (40 J and 50 J) and the damaging impact at an energy of 55 J. About 1ms after the ToA of the impact signal, the gradient of the signal has a slight shift, indicating additional frequency responses compared to the pristine cases. This level 1 analysis shows the fibre failure mode. Although the intensity (energy) of the 55J impact within this region is limited, there is a clear indication of damage. The lower intensity of this damage, has to do with the frequency range. High frequency waves have a higher attenuation and are lower in energy than lower frequency waves. The level 2 analysis is plotted in Figure 6.3b and has two clear regions in which the change in the gradient of the slope is evident. This region is within the peak frequency range of delaminations (50 - 150 kHz) and fibre/matrix debonding (200 - 300 kHz), making the distinction between delamination and fibre/matrix debonding difficult. The level 2 decomposition shows two clear gradient changes, again indicating that damages are induced with the 55 J impact. A delamination event can however be detected by the level 3 decomposition, plotted in Figure 6.3c. This plot shows a clear deviation in the pristine signals and the damaged signal where the energy of a delamination event is much higher than a fibre/matrix debonding from level 2. Also, the two gradient changes in the signal are also present in the level 3 decomposition. This feature allows to distinguish the delamination characteristics from fibre/matrix debonding. It is evident in the level 3 decomposition that the initial gradient (between 0 and 1.6 ms) is shallower, indicating less energy. As stated in the literature review, delaminations cause a drop in energy, due to the waves being trapped within the damaged area. This indicates that level 3 analysis indeed complies with the delamination failure mode. Finally, the level 5 WT decomposition shown in Figure 6.3d represents the fibre cracking failure mode. When looking at the top layer of the panel, matrix cracking has indeed taken place at the 55 J impact. The gradient change in the 55 J is different from those of the pristine cases. This means that also matrix cracking, occurring within the frequency range of 0 to 50 kHz, can also be detected by this sensor network. When looking at the WT intensity over all decomposition levels, the level 3 decomposition has the largest response. This indicates that detecting delaminations is easier than fibre failure or fibre/matrix debonding. Due to the higher frequency components containing less energy, deviations in the WT energy are therefore also lower. Detectability is therefore harder and sufficient sensor sensitivity is required.

Similar to the flat panel responses, the higher level decompositions (from level 4 and higher) show a non-linear trend for the pristine impact signals. This makes analysis, but also the implementation of a threshold for automated real-time damage detection, more difficult.

Thickness change influence

Detecting damages in a section where the sensor and the impact location are within the same thickness area, is possible using the WT method. In aerospace structures, thickness variations are unavoidable. In some structures, it is not possible to place the sensor at locations where the thickness deviates due to lacking room or applications options for the sensor. Therefore, this thesis will also look at the influence of thickness variations in the panel coherent to the WT results. To determine this thickness change influence, the responses of PZT 6 for IL1 will be analysed.

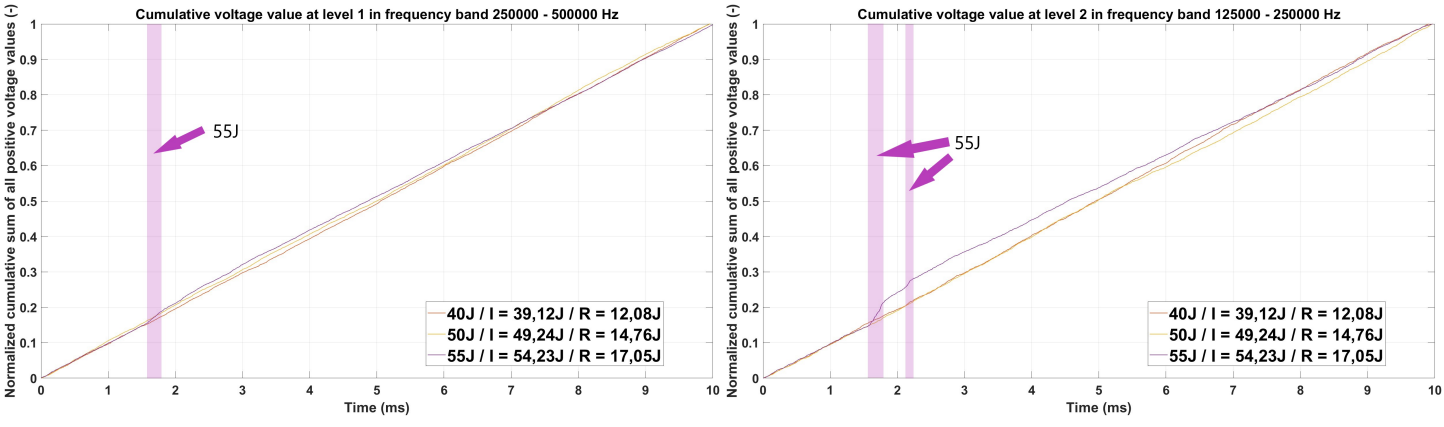

(a) Level 1

(b) Level 2

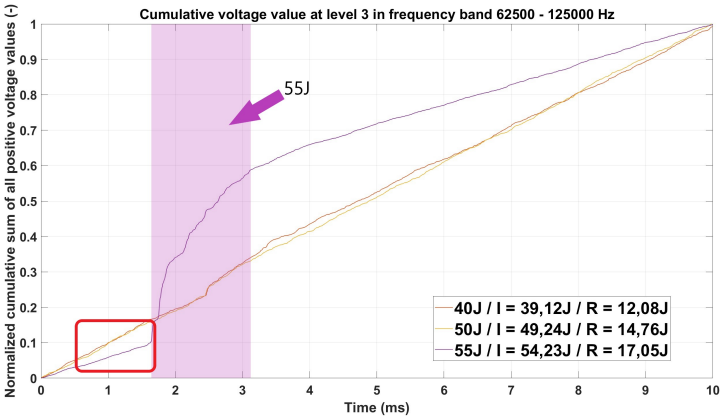

(c) Level 3

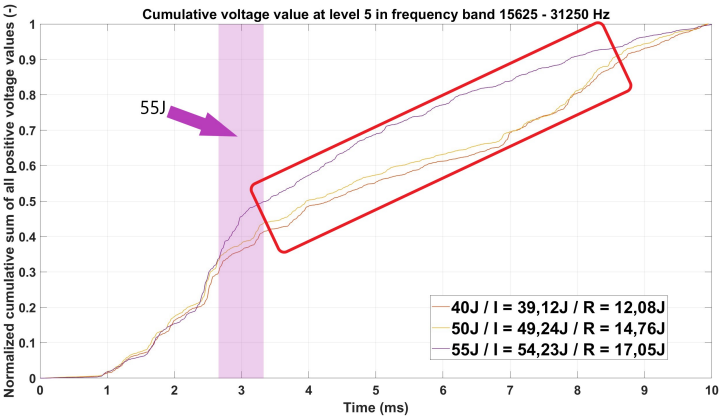

(d) Level 5

Figure 6.3: Baseline analysis for IL1 using PZT5

Upon signal arrival at PZT6, the signal has passed through 2 thickness steps and therefore also three different panel thicknesses. The same impact energies will be used for the analysis as done for the previous baseline analysis. The results are represented in Figure 6.4. When looking at the level 1 and level 2 decomposition levels, the intensity (energy) of the signal is less evident as compared to the results from Figure 6.4a. Regardless of this phenomena, the level 1 and the level 2 detection possibility is still relevant, as the gradient of the WT value is present at around the same time period compared to the previous analysis. When looking at the level 3 analysis, the time period at which the detection of damage is present, is smaller than that in Figure 6.3c. Also, the energy loss at the beginning of the signal is smaller, having to do with the longer distance the signal has to travel to PZT6. The level 5 analysis does show a different behaviour than the level 5 decomposition shown in Figure 6.3d. In Figure 6.4d an evident energy drop is present (marked with a red box), which is not shown in the analysis done in the previous section. Also, the thickness steps along the propagation length of the signal seem to have influence on the time interval at which matrix cracking should be evident. Where the results of the PZT5 data show clear damage features at around 2.7 ms, the PZT6 data already shows deviations from the pristine cases at around 1.8 ms. Comparing this to the baseline results, the levels 1, 2 and 3 shown similar WT results. The results show that higher frequency signals show (near) linear behaviour. The level 5 analysis shows no similarity in this trend. These differences are explainable as attenuation and slowness of the signal have more effect when the propagation distance is longer and changes in the panel dimensions occur. In this thickness change case, the energy of the signal dissipates into voids and more layers. The higher frequency components in the signal evident from level 1 and level 2 signal are less sensitive to these attenuation and slowness factors as the lower frequency components from level 3 and level 5, as described in the literature review..

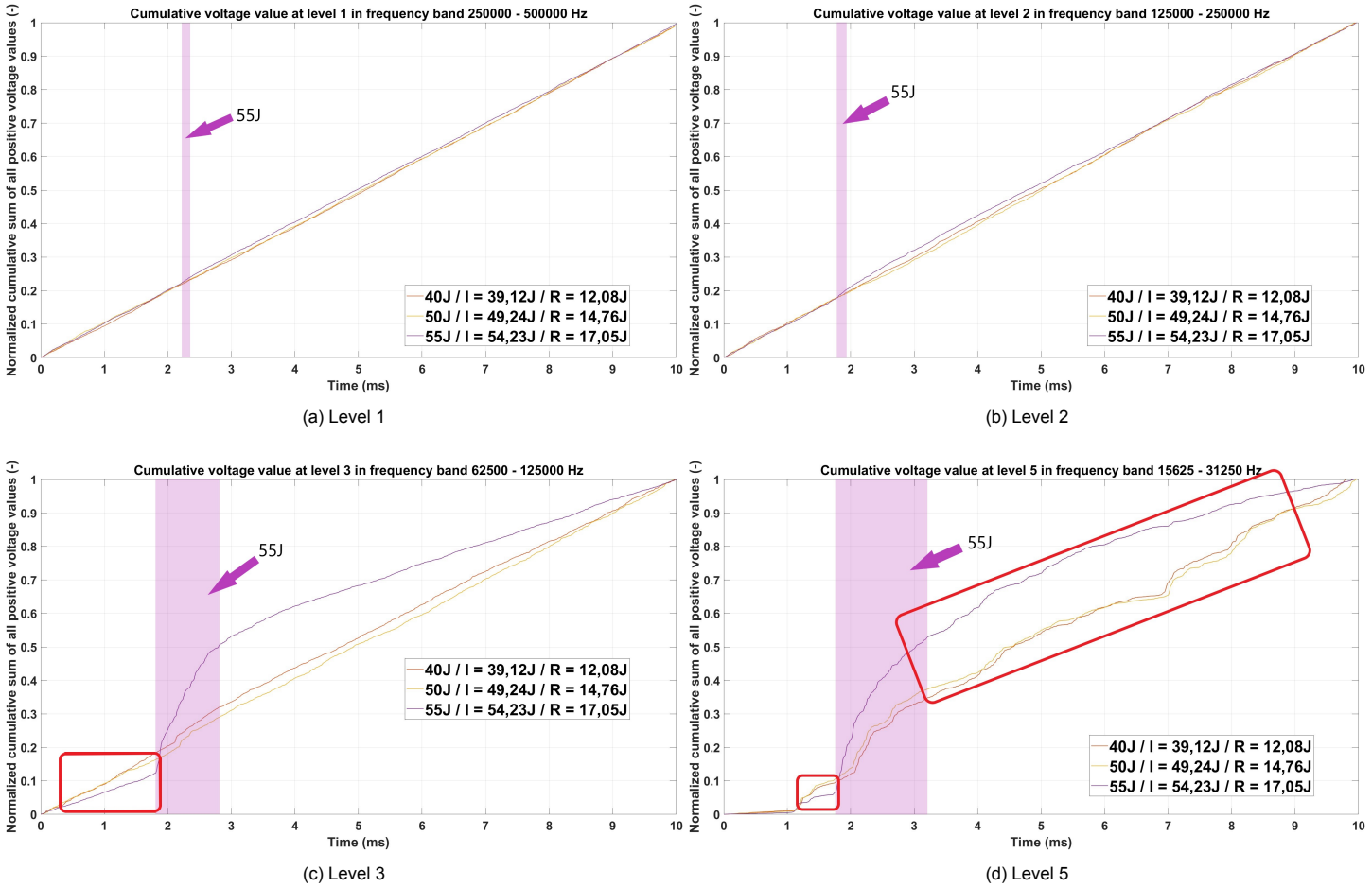

(a) Level 1

(b) Level 2

(c) Level 3

(d) Level 5

Figure 6.4: Thickness change influence for IL1 and PZT6

Stiffener influence

Besides thickness changes, stiffeners are also primary construction features of fuselage skins. The location at which the stiffener is mounted, becomes locally stiff, limiting the vibrating capacity compared to a skin section between stiffeners. This stiffness difference for a skin section in between stiffeners and a skin section on which a stiffener is applied, may result in additional damping features of the impact and damage signal propagating through a stiffener section. To verify if a stiffener has a significant influence on the propagating wave, the data from IL1 will be analysed by means of the data from PZT2. This sensor is on the other side of a stiffener from where the impact occurs, meaning that the stiffener influence can be measured here. These WT analysis results are shown in Figure 6.5. Again, the WT results for the level 1, 2 and 3 decomposition are similar to the baseline results. The main similarity to the baseline signal is that the damage features are present in the same time regions as shown in Figures 6.5a. 6.5b and 6.5c. The biggest difference to the baseline signal is that the intensity of the signal is smaller, meaning that less energy is captured by the sensor. In this case also due to attenuation and slowness of the signal, but now primarily due to the stiffener in between the impact location and the sensor. The level 5 decomposition shows similar deviations to the baseline as described in Section 6.2.1, meaning there is an energy drop just after the ToA at PZT2 and the trend of the signal deviates. In this case, the higher frequency components are affected in lesser amount by the stiffener than the lower frequency components.

When comparing the results with Figure 6.4a, Figure 6.4b and Figure 6.4c, the same trend in both pristine and damaged cases is present. Nevertheless, in all levels it is possible to determine deviations in the signals due to impact damage events when compared to the baseline signal. In summary, the stiffener has more effect on the lower frequency portions of the signal, but do not hinder the possibility to detect the different damage features from the signal using the WT. Overall, the stiffener has less

influence on the energy of the signal than the thickness changes do.

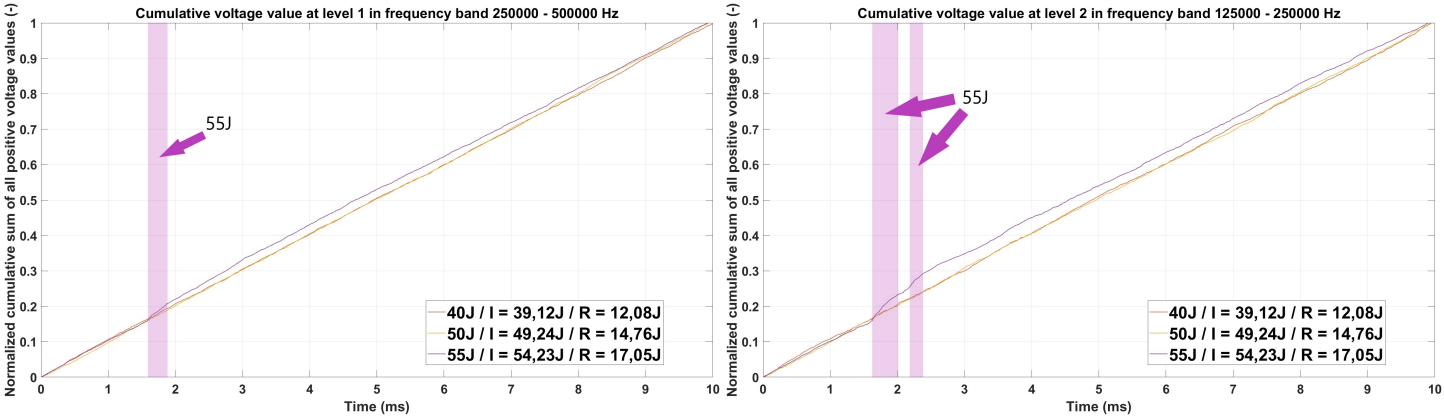

(a) Level 1

(b) Level 2

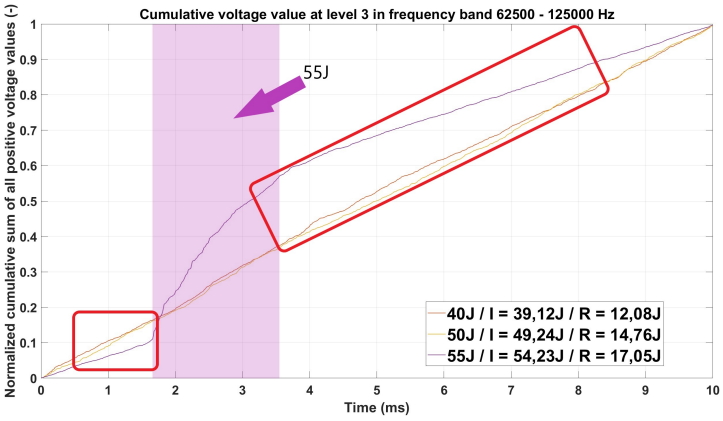

(c) Level 3

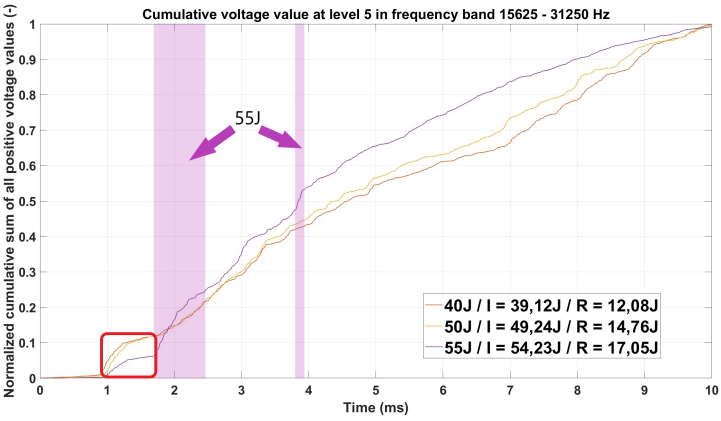

(d) Level 5

Figure 6.5: Stiffener influence for IL1 using PZT2

Damage detection for higher impact energies

In the previous three analysis steps, the influence of the skin, thickness steps and a stiffener are described. This is done for the first impact that has lead to damage in the skin of the composite panel. During the analysis of IL1, the results of even higher impact energies deviated from the 55 J impact. This was not expected, so therefore a further step in the analysis was performed, namely by analyzing the WT results of the higher impact signals. For a clear representation of the higher impact energy results, the 50 J impact energy is used as the pristine case after impact. The 55 J impact signal was used as a reference signal where the first damages have occurred. The results for the 60 J and 70 J impacts are included in this part of the analysis, defined as the higher impact energy levels. The ultrasonic NDT results for these are shown in Figure 6.6. In this Figure, it can be seen that for the 55 J impact the damage area increases significantly when compared to the pristine case (50 J). The area also increases when the panel is impacted at an impact energy of 60 J, but does not significantly increase when impact at 70 J.

To compare the data with the previous baseline analysis, PZT5 is used as sensor. This sensor also captures the first impact and damage signals encountering the least effects of thickness steps and stiffener interference within the first milliseconds of the signal. The level 1, 2, 3 and 5 decompositions are shown in Figure 6.7. In the level 1 analysis, it can be seen that the 60 J impact energy still shows a gradient change compared to the pristine signal. This indicates that the damage induced is sufficient enough to be detected by this algorithm. For the 70 J impact however, the results are not distinguishable from the pristine case (50 J). The trend and slope of the signal is similar for the whole 10 ms analysed. This indicates that the change in damage size from the 55 J or 60 J to 70 J is too minimal for this method to

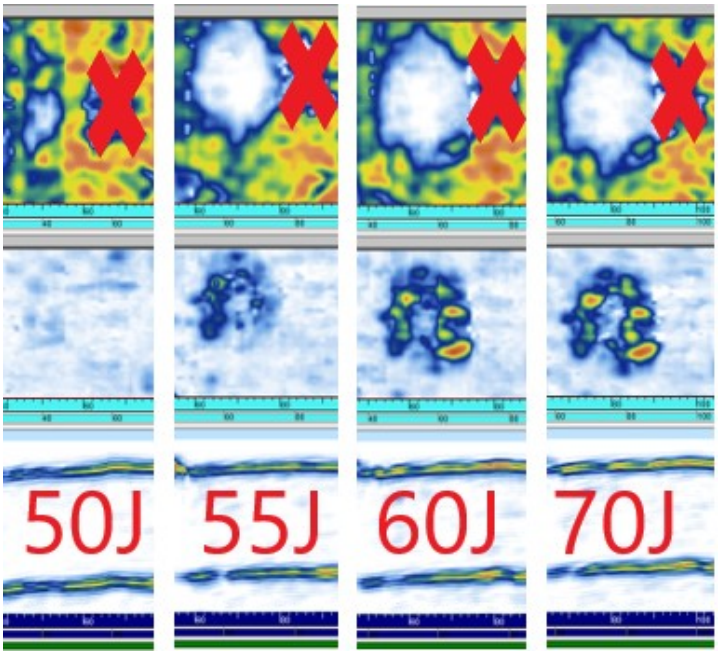

Figure 6.6: ultrasonic NDT scans of the pristine case (50J), initial damage case (55J), first higher impact energy (60J) and the highest impact energy (70J). The red crosses are the location of a sticker placed on the panel, which is no damage.

detect any additional damage. Similar results are shown in the level 2 and 3 decomposition. The level 5 decomposition shows very different trends in all the signal levels, making it hard to draw conclusions about damage being present. Again, the 70 J impact energy WT results show the largest deviations from the pristine signal, but also from the 55 J signal (at which the initial damage has started to form).

Overall, the levels 1, 2 and 3 decomposition levels show very promising results for both damage detection and quantification for both the 55 J and 60 J impact energies. The level 5 analysis shows large deviations between the signals, whereas damage quantification is more difficult. When looking at the increase in damage size, the change from 50 J to 55 J and from 55 J to 60 J are significant enough for the algorithm to detect damages. The difference between the damage size from 60 J to 70 J is minor and therefore not detectable as a damage event using this algorithm. This phenomena can be explained by the energy dissipation through the panel upon impact. When a pristine panel is impacted, all the energy absorbed by the panel can be propagated through the intact fibres and matrix. The signal will therefore also follow a path of low resistance, allowing for steady and comparable signals, even though the impact energies are higher. When the first damage event occurs, the energy is trapped within these damaged zones, making it harder to propagate through the panel. This has been shown especially for delamination and matrix cracking failure modes. Eventually, this leads to the signal deviations as shown in all previous analyses. When the panel is impacted again at that similar and already damaged location, the energy from the impactor cannot be ideally transferred into the panel and is again trapped in the damaged zone. This leads to a drop in the rebound energy of the impactor. As this energy is not fully transmitted through the panel as in the initial damage cases, the damage is not growing significant and not emitting any detectable signal features using this method. When the impact energy is again increased significantly and the damage size also increases, the signal starts to deviate again from the pristine cases, making it possible again to detect the damages.

Sub-conclusions IL1

Based on the results from IL1 and the PZT sensors 2, 5 and 6, some sub-conclusions can be made. These conclusions are based on the acoustic emission peak frequency CFRP damage modes as visualized in Figure 2.1.

Level 1 - Fibre failure The baseline analysis shows that a gradient change from a 55J impact is evident at level 1. This indicates that fibre failure modes can be detected with high sampling frequency sensor

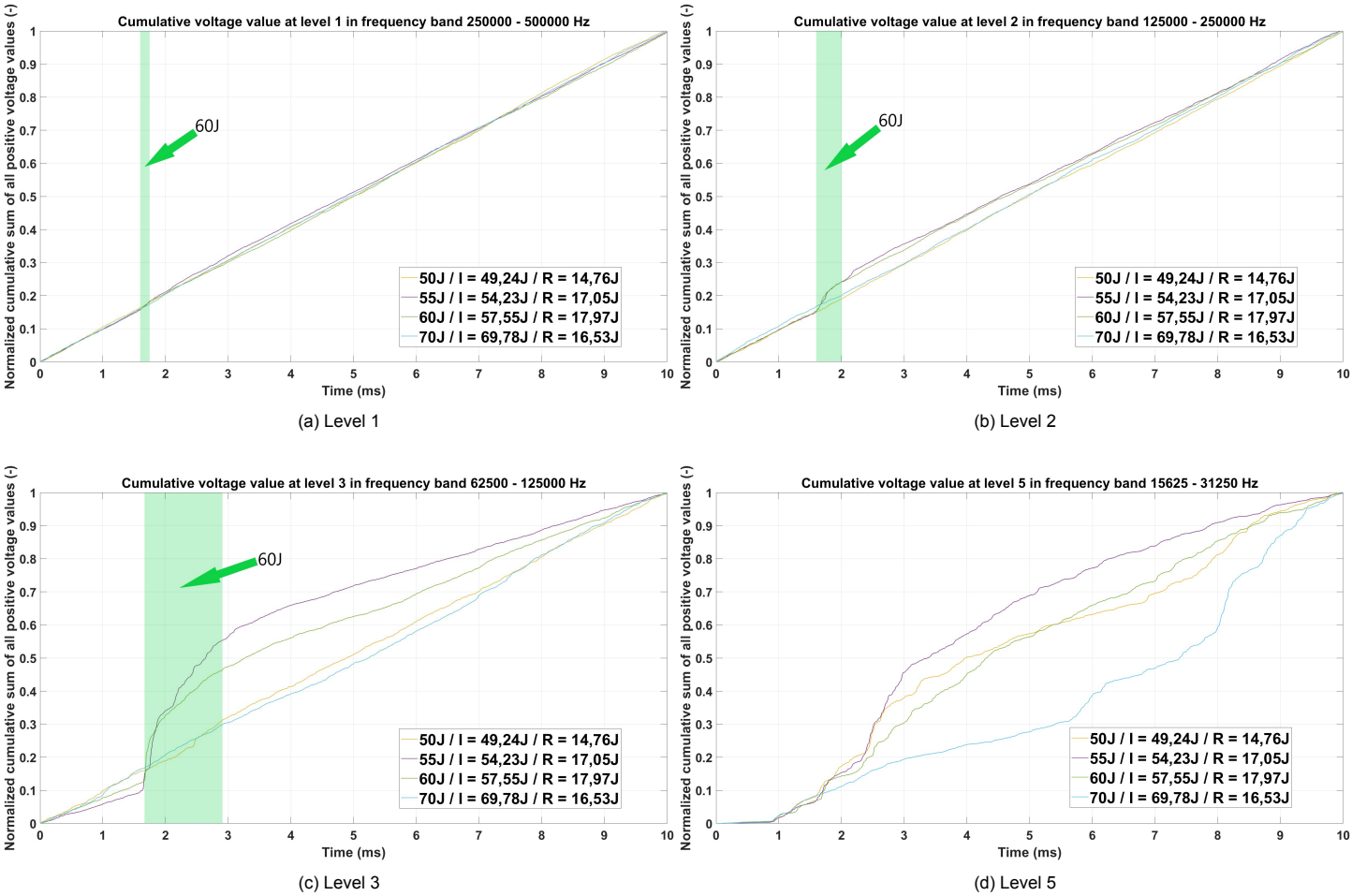

(a) Level 1

(b) Level 2

(c) Level 3

(d) Level 5

Figure 6.7: WT results for higher energy impacts, after initial damage has occurred for IL1 using PZT5.

networks and its feature is visible as gradient change within the first two milliseconds of the signal (after ToA at the sensor). The influence of thickness changes and stiffener interaction are present, but still leads to a positive indication of a damage initiation upon a 55 J impact. The differences to the baseline signal can be explained by attenuation and slowness of the signal, due to longer distances to the sensor and changes in shape or construction of the panel. The effect is limited due to the high frequency of the decomposed signal portion, but also due to the expectation that limited fibre failure has occurred at this impact energy level.

Level 2 - Fibre/matrix debonding The energy dissipated by means of fibre/matrix debonding is higher than that of fibre failure, evident in the level 2 baseline analysis. This damage feature is visible in the WT level 2 decomposition as two steep gradient changes of the 55 J impact within the first two milliseconds after ToA at the sensor. Thickness changes in the structure have significant influence on the WT coefficients, but are still characterised by means of gradient changes within the same time interval. The stiffener has less influence on the level 2 WT coefficients, making it also possible to detect fibre/matrix debonding with a sensor located behind a stiffener in reference to the impact location.

Level 3 - Delamination A delamination event is clearly recognisable in the level 3 WT decomposition. Due to the energy being trapped within the layers of the panel due to delamination, less energy is dissipated through the panel, leading to an energy drop at the beginning of the signal. After this energy drop, a steep gradient change takes place, which ends after approximately 2 ms. The same damage features are detected by the analysis in which thickness changes and stiffener influence is taken into account. In particular, the thickness changes lead to more energy losses during signal propagation, but not limiting the detectability of a delamination event. When looking at the intensity and the detectability

of delamination events, it is the most obvious damage feature detectable by means of WT analysis. As delaminations occur at lower impact energies and lead to sever loss of structural integrity, it is important this failure mode can be detected in all cases.

Level 5 - Matrix cracking The lower the decomposition level, the more influence changes in the structure have. Looking at the baseline analysis, matrix cracking is detectable after 2 ms from ToA at the sensor. When thickness changes are present in the structure, the detectability increases, evident in an energy drop just after the ToA at the sensor, to a significant increase in the gradient of the WT coefficients. the influence of the stiffener is in this case more evident, as the trend of the signal does not deviate as much from the baseline plots as the thickness change does. But, in this case, a drop in energy after the ToA at the sensor and the gradient change right after this event, are evidence that matrix cracking can also be detected with stiffener influence. Also, the level 5 decomposition is most vulnerable to primarily attenuation and slowness, as the signals from the stiffener and thickness influence are the least consistent.

For both the level 3 and 5 decompositions, linearity decreases. For the level 3 decomposition, it is still near similar and possible to determine a threshold value. Defining a threshold value for the level 5 decomposition is challenging. This statement does not only comply to the stiffened panel results, but also to the flat panel results. Ideally, the method will work without the knowledge of the pristine WT results. Linearity makes automation and the determination of a threshold easier.

6.2.2. Damage detection and quantification on a stiffener

To determine if damage can still be detected when an impact occurs on a stiffener, IL2 is further analysed. Also, to determine if the signal can still be detected when the sensor is placed on a stiffener, PZT4 is used. In this case, the 30 J and 40 J impact energies are considered pristine, as at 45 J the ultrasonic NDT result returns a small damaged area in the reflection C-scan. At this energy level and with this damage size, the algorithm was not able to detect a damage in the signal using any PZT sensor. The first detectable damages able to be measured, appeared in the results of the 70 J impacts. These results are therefore further analysed, for which Figure 6.8 will be used. Again, the levels 1, 2, 3 and 5 are used to identify respectively the damage modes matrix cracking, delamination, fibre/matrix debonding and fibre failure. For the fibre failure mode in level 1, no sensor was capable of detecting this composite failure mode. Also not at higher impacts which were executed up to 80 J. Due to lacking ultrasonic NDT results for this particular damage, it cannot be said with full certainty that this failure mode is not detectable. On the stiffener, there is a very high local stiffness compared to impact locations on the skin. Due to this high stiffness, the flexural displacement is also lower than for skin locations, leading to a lower potential of fibre failure being present. The level 2 decomposition however does show deviations of the signal when looking at the 70 J impact. Here, two regions are marked showing slight deviations in the gradient of the WT, where the pristine cases do not show similar behaviour. Due to the gradient difference being very small, this is also a hard failure mode to detect. Despite it being difficult to track, the results show it is not impossible. The level 3 analysis clearly shows the deviation of the signal. As discussed at IL1, there is an energy drop at the beginning of the signal, indicating an energy loss of the signal due to a delamination event. After this, the gradient of the signal deviates extremely from the pristine cases, marking the damage characteristics of a delamination event. Finally, the level 5 decomposition shows the results for matrix cracking, in which the main damage feature is the gradient change starting at 1.8 ms. At this level, lacking linearity again makes analysis harder.

Sub-conclusions IL2

Impact damages on stiffeners has been analysed in the previous section, of some sub-conclusions can be made. These conclusions are again based on the acoustic emission peak frequency CFRP damage modes as visualized in Figure 2.1.

Level 1 For the level 1 analysis, there is no evidence in the signal of fibre failure being present. It is also not evident in the ultrasonic NDT results that this failure mode has occurred. For this level, therefore no clear statement can be made if fibre failure in the skin is detectable when an impact occurs on a stiffener location.

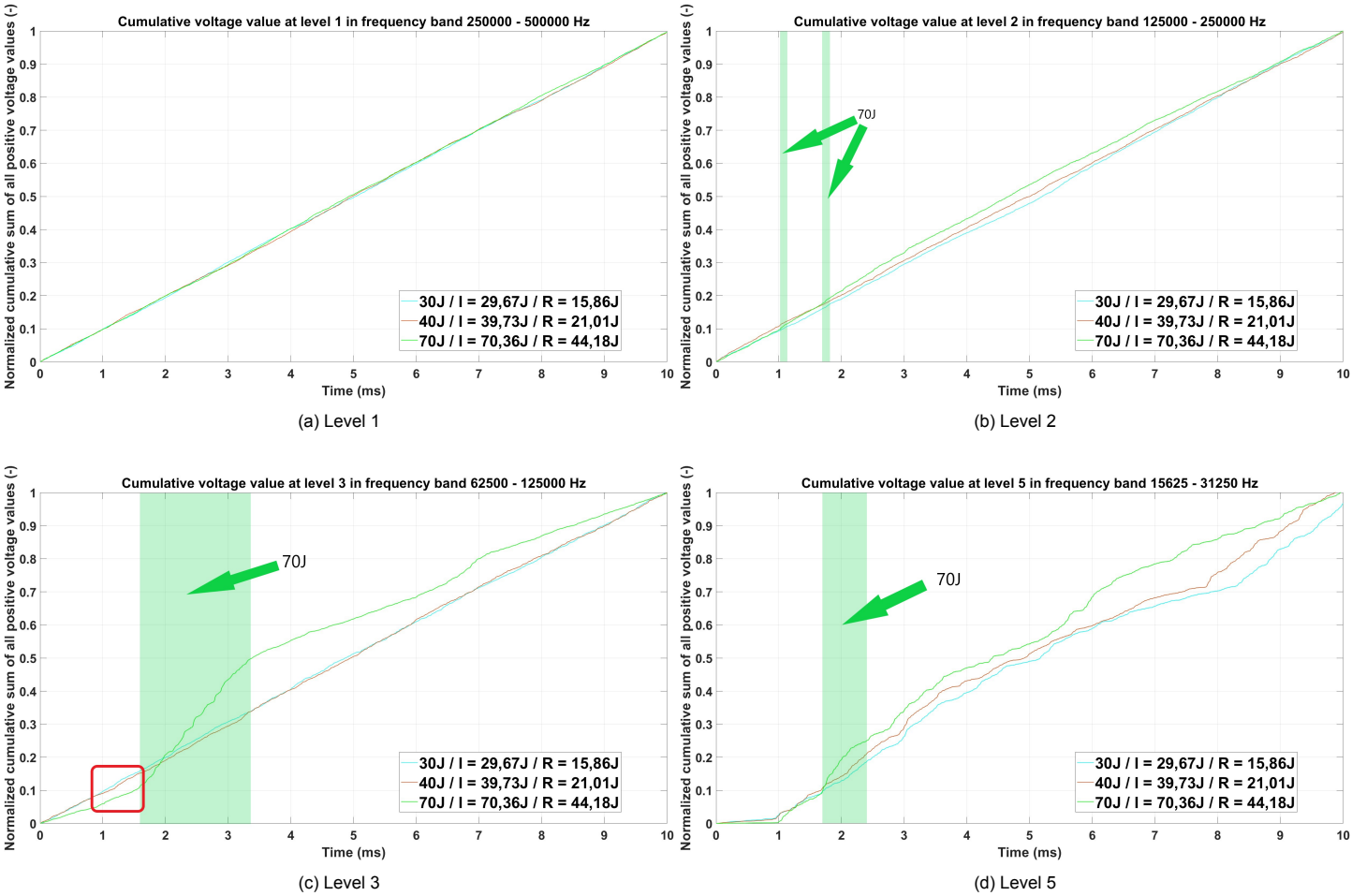

(a) Level 1 (b) Level 2

(c) Level 3 (d) Level 5

Figure 6.8: WT analysis for IL2 and PZT4.

Level 2 This decomposition level shows the first signs of damage being present. Although the deviations of the slope are only slight, it is possible to identify the damage events similar to the trends identified at IL1.

Level 3 The level 3 analysis shows exactly the same trends as the analysis done for IL1. Delamination of the skin seems to be the most detectable failure mode in CFRP materials using this method. Also, linearity of the normalized signals seems to drop the lower the analysis level as shown before. This will make it harder for determining thresholds for which this passive SHM system

Level 5 Although there is a deviation in the signal, it is less obvious than the analysis done for IL1. The main difference is the trend of the damaged signal, which tends to follow the pristine cases more than for instance the level 5 decomposition done for IL1. Again, this has to do with the local stiffness on the stiffener compared to the skin section, causing non-comparable responses. These lead to different results in the WT.

Comparing these results with the results of the analysis done for IL1, the damage characteristics of delaminations and matrix cracking are similar. Fibre/matrix debonding is however less detectable. Fibre failure may have not occurred and therefore no clear comparison can be made. Overall, the analysis of impact damages on a stiffener are harder to detect than when analyzing skin sections. The damaged WT values tend to follow the pristine trends better, making it harder to detect deviations in the signal. Also, the intensity of the WT deviations is lower than that of skin section analysis. Due to the high sensitivity of this sensor system and the use of the WT with the right wavelet, it is still possible to detect damages, also when the impact occurs on a stiffener section.

6.2.3. Damage detection and quantification using FBG sensors

For the analysis using the FBGs, also IL1 will be used. For good comparison of the analysis, ideally the FBG locations near the previous defined PZT locations are used. Due to technical problems of the FBG interrogator, only FBG1 was shown to be a reliable FBG sensor. The individual FBG responses have been determined by cold spray tests, of which the results are shown in Figure 6.9. It appears that when a sensor is frozen, all lower numbered FBG sensors also react to this change, leading to an output signal. In other words, the data produced by FBG2 to FBG8 will not be used in the upcoming analysis. This phenomena is not present when FBG1 is cold sprayed, making this the only reliable sensor for further analysis.

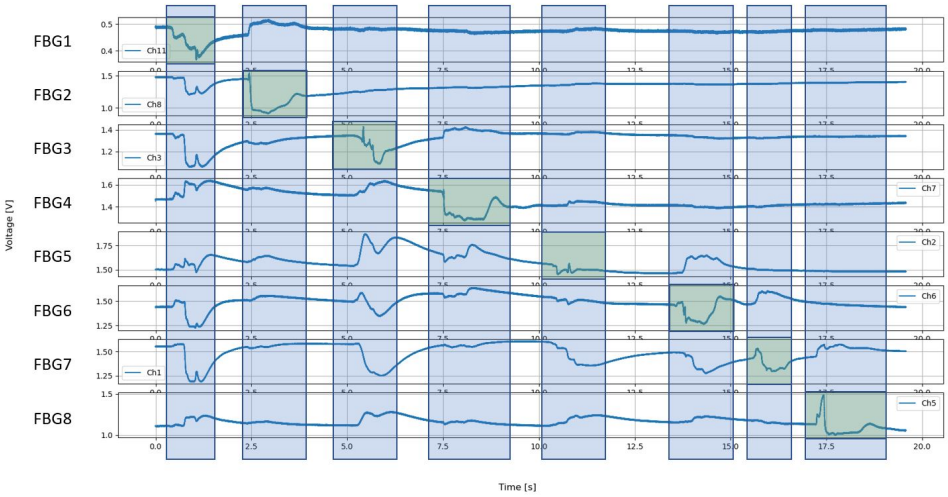

Figure 6.9: Cold spray response test of the FBG sensor system.

To determine if this sensor indeed measures valuable data, the FBG1 sensor data has been processed by the algorithm. Due to unexplainable data loss in the signal, the data has been compressed to the first 5 ms. In this time interval, there is no evidence of data loss. Figure 6.10 shows the level 1, 2, 3 and 5 decomposition for IL1 and FBG1. Again, the results are far from similar to the PZT data. The data is noisy and unreliable in the current set-up. Regardless of the incomparability to the PZT data, the FBG data does not show clear and similar trends for the pristine data, especially in the lower decomposition levels of the WT.

Figure 6.11 shows the power spectrum density plot for FBG1 and PZT1 at IL1 on the stiffened panel. Here, it is clearly seen that the frequency content of the PZT and the FBG are not similar, confirming why the results from Figure 6.10 show divergent results compared to the PZT data. The peak at around 340 kHz of the PZT data is the noise content. The noise content of the FBG data is scattered over the entire frequency spectrum.

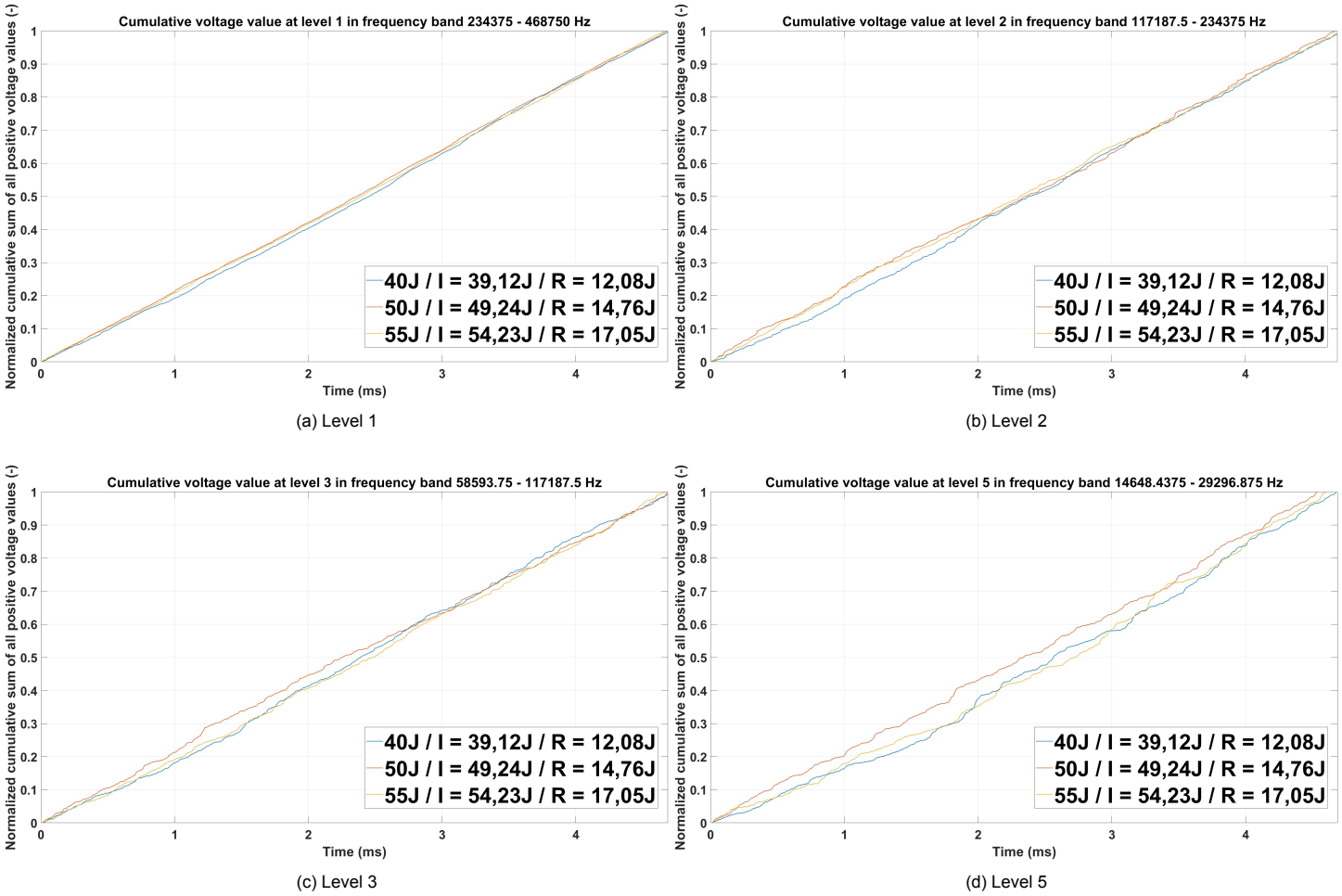

(a) Level 1

(b) Level 2

(c) Level 3

(d) Level 5

Figure 6.10: WT analysis for IL1 using FBG1

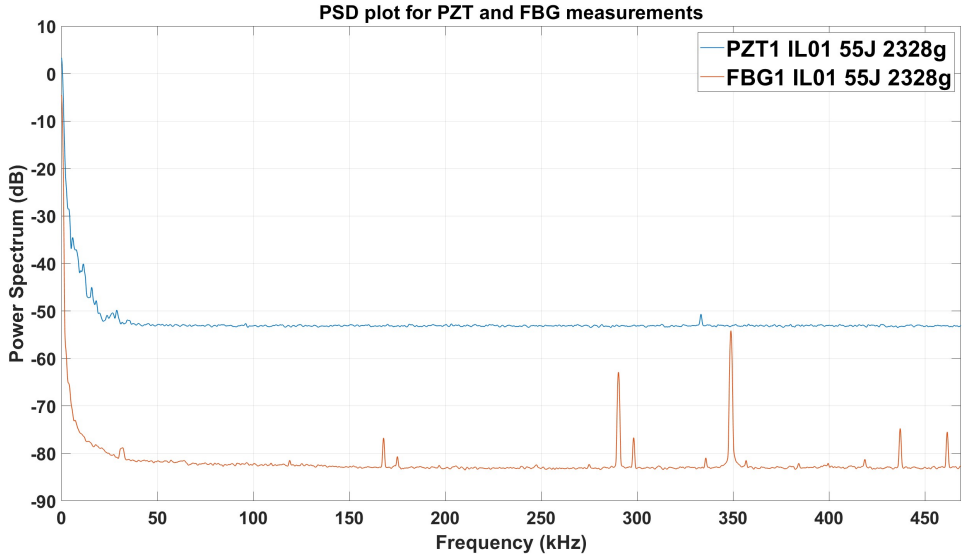

Figure 6.11: PSD plot for IL1, comparing the frequency content of the FBG and PZT signals over the whole frequency spectrum.

6.3. Conclusion

The analysis on the stiffened panel was done, taking the lessons identified from the flat panel into account. With more ultrasonic NDT results, clear damage initiation can be seen, meaning that a more in depth analysis could be done. Again, the peak frequencies of fibre failure, fibre/matrix debonding, delamination and matrix cracking, are used for damage quantification. This analysis has lead to sufficient results to answer the sub-question, stated as: "*How do the defined signal features from the simple composite square panel compare to a complex stiffened composite panel and what influence do the measurements over thickness steps and stiffeners have on the damage detection and quantification possibilities of the algorithm?* ". The answer to this research sub-question will be given below.

During impact testing, the phased array scans were performed after each impact, allowing for defining a baseline signal for each impact location to which the damaged signals could be compared. The **identified features** for decomposition levels 1, 2 and 3 in the baseline analysis are identical to the features identified on the flat panel. This means that the damage features are independent of the structural composition. For the levels 1, 2 and 3, respectively fibre failure, matrix/fibre debonding and delamination is detected by means of gradient changes in the WT. The deviations in the level 5 decomposition are primarily evident in the WT results right after the ToA at the sensor, evident as lower energy in the signal. Also, the trend of the signal deviates from the baseline signal, where no further trend analysis is performed due to the inconsistency at this level.

Due to the panel containing structural differences in the skin, **influence of thickness steps in the skin and the stiffener can be evaluated**. Compared to the baseline measurements, the thickness changes in the panel have more effect on the propagating signal than the stiffener does. This can be linked to slowness and attenuation factors when energy is transferred to thicker sections of the panel. Although the results are affected by thickness changes or stiffener influence, the algorithm is still capable of detecting the damages in all cases. The detection features are similar to the baseline results of the stiffened panel, but also to the flat panel results. This allows for a limited amount of sensors required for damage detection of large areas. Due to gradually increasing the impact energy and actively determining the damage size, an **analysis of cumulative increasing damage** is analysed. This analysis shows that a noticeable increase in the damage size needs to be present at the impact location, for the WT algorithm to detect the damage. When the increase in damage size is very small, it is not detectable. This result is interesting when an aircraft panel is struck multiple times at the same location, due to for instance hail. The capability of detecting these cumulative growing damages is thus also possible. The results for matrix cracking (decomposition level 5) however, are scattered and no clear trend can be determined. Although this scattering occurs, the damaged signals deviate from the baseline and are thus still indications for damage initiated after impact. Finally, **the influence of an impact directly on a stiffener** is analysed. A stiffener has a very high local stiffness compared to a skin section. The algorithm is again capable of detecting impact damage directly on the stiffener. These damages are indicated by means of gradient changes in the WT results. The detection of fibre failure however is not detected, for which no conclusion can be drawn. When looking at attenuation and slowness factors, the lower frequency decomposition levels are most affected, meaning that the detectability in these ranges are most vulnerable when distances or structural complexity are increased.

The analysis as described above has also been done using FBG data. the interrogator system used to obtain this data is unreliable. Unfortunately, other commercially available interrogator systems do not offer the required high sample rates. Therefore, the FBGT system, as implemented in this thesis, is not yet suitable for damage detection and quantification applications. The algorithm has been proved effective using PZT data. This means that the algorithm should also work for FBG data, if high sampling rate FBG interrogators are available.

6.4. Observations and lessons learned

Although knowledge has been gained during the tests on the flat panel, there are (additional) observations and lessons learned that will be described in this section. These points are briefly discussed in this section.

- After improving the FBGT set-up, cold-spray tests still showed that the FBG sensors in the fibre

have significant cross-talk. As FBG1 was not influenced, the possibility was present for this sensor to measure relevant impact data. The results however prove differently, where the signals lack higher frequency response data. This means that the FBGT system is not yet fully capable for damage detection application on structural components at this current state.

- Similar to the quantification possibility described at the flat panel, more research needs to be performed on the failure modes in the panels. This can be done by performing additional frequency response tests, where specific damages are induced. Analysing these results will lead to a more reliable conclusion regarding impact damage quantification.
- No tests have been performed at lower impact energies, after damaged had been induced. With these additional impact tests at non-damaging impact energies, the comparison in the baseline signals can be made. This can proof that indeed the damage has caused the additional frequency responses in the signal. Because the panel is already damaged, no additional frequency components should propagate through the panel.
- This research has also addressed cumulative damage growth. To determine if the response signal is indeed influenced by the already present damage at post damage impacts. This can also be argued more when additional non-damaging impacts are performed at these locations.
- It is not fully verified if fibre failure has occurred in the skin above the stiffener. Due to the high local stiffness, it is most likely that fibre failure has not occurred and is therefore not detected by the algorithm.
- For defining a threshold for damage detection, linearity is desirable. Everything that deviates from this trend, taking external factors into account, can be an indication for a damage event. The lower the decomposition level, the less linear the signals are. Further research may thus look at threshold definitions, using the WT coefficients or the cumulative sum values. Automation of the gradient changes may therefore be useful.
- The level 2 decomposition consists of both peak frequencies of fibre/matrix debonding and delamination. This makes the level 2 analysis slightly more difficult. But, using the level 3 decomposition for full delamination identification, a comparison can be made in the frequency characteristics. Future research can also use the WPT to split the frequency band to the desired ranges.
- Similar to the flat panel analysis, the negative WT values have not been taken into account. Using the absolute value, may lead to additional frequency components, which are desirable for the analysis.

7

Conclusions

7.1. Conclusions

Within the aerospace industry, down time of aircraft due to unplanned inspections, is expensive and causes more down time. Especially, composite materials are vulnerable for multiple failure modes due to external forces such as impacts, but these damages are not always visible without the use of advanced and expensive non-destructive testing (NDT) equipment. Therefore, the main research objective of this masters thesis was to investigate the capabilities of a piezoelectric Lead Zirconate Titanate (PZT) and a new state-of-the-art fibre Bragg grating (FBG) sensor system for passive impact damage detection on composite panels and possibly complex stiffened composite structures. This research objective has been achieved by impacting both a simple composite panel and a stiffened composite panel, both being monitored by the same FBG and PZT sensor systems. By gradually increasing the impact energies from non-damaging to damaging impacts, processing this data with a specially designed algorithm and analyzing the results, sufficient data of both the optical and piezoelectric sensor systems were gathered to extract the damage features from the signals.

To answer the research question, three sub-questions were defined. The first sub-question focused on selecting the wavelet transform (WT) analysis method and wavelet. Due to the high resolution in both time and frequency, essential for feature extraction, the wavelet transform is the ideal analysis method for the defined problem. Due to the high computational efficiency and the easy ability to analyse the results, the discrete wavelet transform is the chosen method. The wavelet, suitable for feature extraction, is the Daubechies 5 (db5) wavelet. This wavelet has a low amount of vanishing moments, but is still regular enough to fit the transient signal. Its asymmetric, compact supported and orthonormal characteristics, make this wavelet very suitable for the discrete wavelet transform (DWT) method and for feature extraction.

To answer the second research sub-question, in which identifying the signal features and linking this to specific damage types was the goal, impact tests have been performed on a flat composite panel. The region of interest within the signal, is within the first 10 ms of the signal. It is shown in the unprocessed signal, the short-time Fourier transform (STFT) and the wavelet transform, that the signal contains features which can be linked to the damage. The results of both the 100 kHz and 1 MHz sampling rate were analysed, for which damage detection was possible using the PZT data in both cases. For the 100 kHz data, the largest signal content is available in the first decomposition level. As this frequency band lies within the peak frequency range of matrix cracking, only this failure mode can be detected. The damage features are represented by gradient changes in the WT results, making them differ from the undamaged WT results. Similar analysis has been done for the 1 MHz sampling rate data, again only for the PZT sensors. With this data, the peak frequencies of fibre failure, fibre/matrix debonding, delamination and matrix cracking are detectable respectively in the level 1, level 2, level 3 and level 5 decompositions. The main damage features in the WT for fibre failure, fibre/matrix debonding and delamination are gradient changes, when compared to near linear trends of the pristine WT results. Matrix cracking however, is most evident as a energy drop of the propagating wave, visualized by a

lower energy values at the time of arrival (ToA) at the sensor.

The results of the flat panel have given decent results for damage detection and feature extraction. As this panel is not representative as a skin panel, a stiffened composite panel (of the same material as the flat panel) has also been impacted. This panel contained 2 thickness steps to both sides, has 3 stiffeners and has other dimensions than the flat panel. Similar to the flat panel, the damage features for fibre failure, fibre/matrix debonding and delamination are increased in the gradient of the WT result, deviating from the near linear trend of the pristine cases. Matrix cracking also shows a drop in energy, right at the ToA at the sensor. Due to the geometry differences, additional analyses has been done. The effect of the thickness changes and stiffener influence have been examined. In all cases, damage detection and quantification was possible. The changes in thickness steps have the most influence on the signal energy, evident by the damage characteristics (gradient changes) being less evident. A stiffener has limited influence on the detectability of the damage features. When impacting on a stiffener directly, the damage is also detectable, again containing the same damage features.

The FBGT-M1200 interrogator, sampling at a maximum of 937.5 kHz at each FBG, was unable to extract the signal features from the signal. Cross-talk, data loss and lacking higher frequency data components are the primary causes of lacking damage detection capabilities. However, similar WT results should be obtained using FBG sensors, when a suitable high sampling rate FBG interrogator is available.

Summarized, fibre failure, fibre/matrix debonding and delaminations are evident by gradient changes in the WT values of the impacts leading to damage. Even barely visible impact damages are detected by means of this passive SHM monitoring method. The pristine cases are near linear, where the damaged cases clearly deviate. This linearity allows for great potential in automating this damage detection algorithm, without knowing the pristine impact trends. However, the more decomposition levels are analysed, the more the levels deviate from the linear trend. Also, the trends for matrix cracking at these sampling frequencies lack, making it hard to determine a specific damage feature. These results also acknowledge the hypothesis defined, where the sensor data deviates for impact damage events in specific frequency bands. This answers the main research question, achieving this masters thesis goal.

Although the FBG data did not contain relevant damage features, the PZT data has provided sufficient data to conclude that impact damage detection is indeed possible, where different failure modes also return different signal features. This method thus has potential for development to a real-time impact monitoring system, for which some recommendations will be done in the next section.

7.2. Limitations

Although damage detection and damage feature extraction is possible with the developed methodology, there are some work limitations. These limitations are summarized in the following bullets.

- One of the main goals of this research was to investigate the potential of optical sensor systems used for damage detection capability. The FBGT system used in this research was new and not yet fully developed, introducing a risk in the research. Unfortunately, system improvements did not yet allow for the same damage detection capability as the PZT system did.

- The conclusions drawn for the flat panel are valid, but could be more specific when the phased array scans were performed after each impact. Lacking this data, all the signals needed to be taken into account, making the analysis more difficult. This was a lesson learned, taken into account during the tests on the stiffened panel. This lead to an easier but also clearer analysis.

- The panel has not been exposed to external forces such as vibrations, compression and tension, which is not representable for an in-service aircraft. Also, temperature, shape and impactor mass were kept as constant as possible where in real life situations, the shape, weight and temperature are different. Both panels were flat, which is not representative for real aircraft structures. These structures are most often curved of which this effect has not been studied.

- The ultrasonic NDT method used, did not allow the classification of the failure modes present in the panel. It only allowed for visualizing the extent of damage within the panel. Due to this limitation, the necessity of using predefined peak frequencies for damage cases was required for damage quantification. A deeper investigation in correlation between the decomposition level and the failure mode may be required for certain applications.
- The different vibrational modes have not been taken into account in this research. The weight of the impactor defines the primary vibration mode in which the panel will vibrate. Lower weights allow for guided waves to be dominant. Vibrational waves are dominant when higher impactor weights are used. Also impact time duration leads to different types of vibration modes.
- This research has focused on thickness variation and stiffener effect on the damage features. Maximum distances between sensors has not been taken into account.
- Not all data has been analysed of the large amount of data produced during the multiple tests and multiple sensor systems. Only the most interesting impact locations and reliable sensors have been used in this research.

7.3. Future work recommendations

Based on the sub-conclusions and discussion in the chapters of this thesis, incorporating this works limitations and improvements, some recommendations for future work on this subject can be defined.

- Many improvements and developments of the FBGT system have been applied to the system available at NLR. Data loss and sensor cross-talk need to be fixed in the next updates of the system, but the system has potential in matching the capabilities of the PZT sensors when fully operational. This will close the technological gap of the current available FBG interrogation systems.
- This work lacked active phased array scans, which made the analysis a lot harder. Future work should take the necessity of sufficient ultrasonic NDT data more into account.
- Further research can lead to a system in which the criteria of damage features in signals are incorporated and therefore no low impact energy comparison is needed. This will lead to a real time impact damage system. For this, a damage index can be determined from WT results. If this DI is exceeded, this will be an indication for a damage. For each frequency band, a DI can be determined and fully automated.
- To confirm if the damaged signal is different due to damage in relation to the impact energy, it is recommended to do additional lower energy impacts at certain locations after the damage impacts. If the signals at the low energy impacts are the same (linear trend) as those of the initial low energy impacts, the deviating signal can be more likely linked to a damage feature.
- This research is limited to static testing in ideal conditions. Future work can focus on testing in cold/hot environments, with external forces applied, with vibrations present and with more sophisticated aircraft structures. These research possibilities will increase the amount of case studies.
- More case studies should focus on damage detection and quantification of a single failure mode, to more precisely determine the features of different damages modes. Initiating a single type of composite failure is difficult with impacts, where this research proves that multiple failure modes initiate.
- During the in service life time of an aircraft, impacts from objects with different masses and geometry are highly plausible. Smaller objects with lower weight are more likely to impact an aircraft than 5 kg objects. Unfortunately, the drop tower limitations forced the use of higher impactor masses, which are more representable for impacts with tooling during maintenance. The weight does also have influence on the the dominant wave mode propagating through the panel. Future work could incorporate more realistic masses (corresponding to for instance hail and other foreign object damage) and analyse the effect of these different dominant wave modes on the damage

features. The theory for these dominant wave modes is described in the test plan in Appendix A.2.

- Future research can do additional tests to determine the maximum distance allowed between sensors for the damage detection capability to still be feasible. Attenuation and slowness factors can thus be clarified, leading to a standard sensor distance requirement within aerospace application regarding damage detection and quantification.
- Data from all sensors and impact locations are archived and can be further analysed by the algorithm for further research. Also, different wavelets can be used in the analysis, to determine the differences in results.

References

[1] J. Martin, “6 - Composite Materials,” in *Materials for Engineering (Third Edition)*, J. Martin, Ed., Third Edition, Woodhead Publishing, 2006, pp. 185–215, ISBN: 978-1-84569-157-8. DOI: https://doi.org/10.1533/9781845691608.2.185. [Online]. Available: https://www.sciencedirect.com/science/article/pii/B978184569157850006X.

[2] V. Karbhari, “2 - Fabrication, quality and service-life issues for composites in civil engineering,” in *Durability of Composites for Civil Structural Applications*, ser. Woodhead Publishing Series in Civil and Structural Engineering, V. M. Karbhari, Ed., Woodhead Publishing, 2007, pp. 13–30, ISBN: 978-1-84569-035-9. DOI: https://doi.org/10.1533/9781845693565.1.13. [Online]. Available: https://www.sciencedirect.com/science/article/pii/B9781845690359500025.

[3] A. Ghobadi, “Common type of damages in composites and their inspections,” *World Journal of Mechanics*, vol. 07, pp. 24–33, Jan. 2017. DOI: 10.4236/wjm.2017.72003.

[4] D. Kreculj and B. Rasuo, “Review of impact damages modelling in laminated composite aircraft structures,” *Tehnicki Vjesnik*, vol. 20, pp. 485–495, Jun. 2013.

[5] V. Giurgiutiu, “Damage and failure of aerospace composites,” pp. 125–175, Dec. 2016. DOI: 10.1016/B978-0-12-409605-9.00005-2.

[6] A. Rajabzadeh, “Accurate structural health monitoring in composites: With fibre Bragg grating sensors,” *Institutional Repository*, Oct. 2020. DOI: https://doi.org/10.4233/uuid:3c85713e-7158-4d67-b93b-54f02e213c12.

[7] S. Hassani, M. Mousavi, and A. H. Gandomi, “Structural health monitoring in composite structures: A comprehensive review,” *Sensors*, vol. 22, no. 1, 2022, ISSN: 1424-8220. DOI: 10.3390/s22010153. [Online]. Available: https://www.mdpi.com/1424-8220/22/1/153.

[8] V. Giurgiutiu, “16 - Structural health monitoring (SHM) of aerospace composites,” in *Polymer Composites in the Aerospace Industry*, P. Irving and C. Soutis, Eds., Woodhead Publishing, 2015, pp. 449–507, ISBN: 978-0-85709-523-7. DOI: https://doi.org/10.1016/B978-0-85709-523-7.00016-5. [Online]. Available: https://www.sciencedirect.com/science/article/pii/B9780857095237000165.

[9] A. G. Anisimov, R. M. Groves, and C. Schoemaker, “Delft University of Technology AE4ASM108 course reader, Experimental Techniques and Non-destructive Testing,” 2020/2021.

[10] J. Cai, L. Qiu, S. Yuan, L. Shi, P. Liu, and D. Liang, “Structural health monitoring for composite materials,” in *Composites and Their Applications*, N. Hu, Ed., Rijeka: IntechOpen, 2012, ch. 3. DOI: 10.5772/48215. [Online]. Available: https://doi.org/10.5772/48215.

[11] A. Güemes, A. Fernandez-Lopez, A. R. Pozo, and J. Sierra-Pérez, “Structural health monitoring for advanced composite structures: a review,” *Journal of Composites Science*, vol. 4, no. 1, 2020, ISSN: 2504-477X. DOI: 10.3390/jcs4010013. [Online]. Available: https://www.mdpi.com/2504-477X/4/1/13.

[12] S. Hassani, M. Mousavi, and A. Gandomi, “Structural health monitoring in composite structures: a comprehensive review,” *Sensors*, vol. 22, p. 153, Dec. 2021. DOI: 10.3390/s22010153.

[13] F. Guo, W. Li, P. Jiang, F. Chen, and Y. Liu, “Deep learning approach for damage classification based on acoustic emission data in composite materials,” *Materials*, vol. 15, p. 4270, Jun. 2022. DOI: 10.3390/ma15124270.

[14] A. K. Biswas, A. K. Datta, P. Topdar, and S. Sengupta, “Acoustic emission-based damage detection and classification in steel frame structure using wavelet transform and random forest,” *Periodica Polytechnica Civil Engineering*, vol. 66, no. 4, pp. 1183–1198, 2022. DOI: 10.3311/PPci.20447. [Online]. Available: https://pp.bme.hu/ci/article/view/20447.

[15] J. Bohse and A. Brunner, “Acoustic emission in delamination investigation,” in Dec. 2008, pp. 217–277, ISBN: 9781845692445. DOI: 10.1533/9781845694821.2.217.

[16] G. Qi, “Wavelet-based AE characterization of composite materials,” *NDT & E International*, vol. 33, no. 3, pp. 133–144, 2000, ISSN: 0963-8695. DOI: https://doi.org/10.1016/S0963-8695(99)00037-7. [Online]. Available: https://www.sciencedirect.com/science/article/pii/S0963869599000377.

[17] R. Gutkin, C. Green, S. Vangrattanachai, S. Pinho, P. Robinson, and P. Curtis, “On acoustic emission for failure investigation in cfrp: Pattern recognition and peak frequency analyses,” *Mechanical Systems and Signal Processing*, vol. 25, no. 4, pp. 1393–1407, 2011, ISSN: 0888-3270. DOI: https://doi.org/10.1016/j.ymssp.2010.11.014. [Online]. Available: https://www.sciencedirect.com/science/article/pii/S0888327010004176.

[18] J. L. Rose, “A Baseline and Vision of Ultrasonic Guided Wave Inspection Potential,” *Journal of Pressure Vessel Technology*, vol. 124, no. 3, pp. 273–282, Jul. 2002, ISSN: 0094-9930. DOI: 10.1115/1.1491272. eprint: https://asmedigitalcollection.asme.org/pressurevesseltech/article-pdf/124/3/273/5656578/273_1.pdf. [Online]. Available: https://doi.org/10.1115/1.1491272.

[19] R. James and V. Giurgiutiu, “Towards the generation of controlled one-inch impact damage in thick CFRP composites for SHM and NDE validation,” *Composites Part B: Engineering*, vol. 203, p. 108 463, 2020, ISSN: 1359-8368. DOI: https://doi.org/10.1016/j.compositesb.2020.108463. [Online]. Available: https://www.sciencedirect.com/science/article/pii/S1359836820335125.

[20] M. Mitra and S. Gopalakrishnan, “Guided wave based structural health monitoring: a review,” *Smart Materials and Structures*, vol. 25, no. 5, p. 053 001, Mar. 2016. DOI: 10.1088/0964-1726/25/5/053001. [Online]. Available: https://doi.org/10.1088/0964-1726/25/5/053001.

[21] Z. Su and L. Ye, *Identification of Damage Using Lamb Waves: from Fundamentals to Applications*. Jan. 2009, vol. 48, ISBN: 978-1-84882-783-7. DOI: 10.1007/978-1-84882-784-4.

[22] P. C. Vinh, “Scholte-wave velocity formulae,” *Wave Motion*, vol. 50, no. 2, pp. 180–190, 2013, ISSN: 0165-2125. DOI: https://doi.org/10.1016/j.wavemoti.2012.08.006. [Online]. Available: https://www.sciencedirect.com/science/article/pii/S0165212512001047.

[23] Z. Su, L. Ye, and Y. Lu, “Guided Lamb waves for identification of damage in composite structures: a review,” *Journal of Sound and Vibration*, vol. 295, no. 3, pp. 753–780, 2006, ISSN: 0022-460X. DOI: https://doi.org/10.1016/j.jsv.2006.01.020. [Online]. Available: https://www.sciencedirect.com/science/article/pii/S0022460X0600109X.

[24] M. T. H. Sultan, K. Worden, S. G. Pierce, D. H. W. J. Staszewski, J. M. Dulieu-Barton, and A. Hodzic, “On impact damage detection and quantification for CFRP laminates using structural response data only,” *Mechanical Systems and Signal Processing*, vol. 25, no. 8, pp. 3135–3152, Nov. 2011. DOI: 10.1016/j.ymssp.2011.05.014.

[25] N. Miesen, Y. Mizutani, R. M. Groves, J. Sinke, and R. Benedictus, “Lamb wave detection in prepreg composite materials with fibre Bragg grating sensors,” in *Sensors and Smart Structures Technologies for Civil, Mechanical, and Aerospace Systems 2011*, M. Tomizuka, Ed., International Society for Optics and Photonics, vol. 7981, SPIE, 2011, pp. 732–742. DOI: 10.1117/12.880215. [Online]. Available: https://doi.org/10.1117/12.880215.

[26] L. Cheng, H. Xin, R. M. Groves, and M. Veljkovic, “Acoustic emission source location using Lamb wave propagation simulation and artificial neural network for I-shaped steel girder,” *Construction and Building Materials*, vol. 273, p. 121 706, 2021, ISSN: 0950-0618. DOI: https://doi.org/10.1016/j.conbuildmat.2020.121706. [Online]. Available: https://www.sciencedirect.com/science/article/pii/S0950061820337107.

[27] P. Cawley and D. Alleyne, “The use of Lamb waves for the long range inspection of large structures,” *Ultrasonics*, vol. 34, no. 2-5, pp. 287–290, 1996, Cited by: 307. DOI: 10.1016/0041-624X(96)00024-8. [Online]. Available: https://www.scopus.com/inward/record.uri?eid=2-s2.0-0030171571&doi=10.1016%2f0041-624X%2896%2900024-8&partnerID=40&md5=9c5139fe162b14ffb210179dbd9c2a5d.

[28] V. Giurgiutiu, “Chapter 6 - guided waves,” in *Structural Health Monitoring with Piezoelectric Wafer Active Sensors (Second Edition)*, V. Giurgiutiu, Ed., Second Edition, Oxford: Academic Press, 2014, pp. 293–355, ISBN: 978-0-12-418691-0. DOI: https://doi.org/10.1016/B978-0-12-418691-0.00006-X. [Online]. Available: https://www.sciencedirect.com/science/article/pii/B978012418691000006X.

[29] V. Ewald, R. M. Groves, and R. Benedictus, “Transducer placement option for ultrasonic Lamb wave structural health monitoring (SHM) on damage tolerant aircraft substructure,” Sep. 2017. DOI: 10.12783/shm2017/14063.

[30] S. Pant, J. Laliberte, M. Martinez, and B. Rocha, “Derivation and experimental validation of Lamb wave equations for an n-layered anisotropic composite laminate,” *Composite Structures*, vol. 111, pp. 566–579, 2014, ISSN: 0263-8223. DOI: https://doi.org/10.1016/j.compstruct.2014.01.034. [Online]. Available: https://www.sciencedirect.com/science/article/pii/S0263822314000476.

[31] Z. Tian, L. Yu, and C. Leckey, “Delamination detection and quantification on laminated composite structures with Lamb waves and wavenumber analysis,” *Journal of Intelligent Material Systems and Structures*, vol. 26, no. 13, pp. 1723–1738, 2015. DOI: 10.1177/1045389X14557506. eprint: https://doi.org/10.1177/1045389X14557506. [Online]. Available: https://doi.org/10.1177/1045389X14557506.

[32] P. Ochôa, R. Groves, and R. Benedictus, “Effects of high-amplitude low-frequency structural vibrations and machinery sound waves on ultrasonic guided wave propagation for health monitoring of composite aircraft primary structures,” *Journal of Sound and Vibration*, vol. 475, p. 115 289, Feb. 2020. DOI: 10.1016/j.jsv.2020.115289.

[33] V. Giurgiutiu, “Chapter 7 - piezoelectric wafer active sensors – pwas transducers,” in *Structural Health Monitoring with Piezoelectric Wafer Active Sensors (Second Edition)*, V. Giurgiutiu, Ed., Second Edition, Oxford: Academic Press, 2014, pp. 357–394, ISBN: 978-0-12-418691-0. DOI: https://doi.org/10.1016/B978-0-12-418691-0.00007-1. [Online]. Available: https://www.sciencedirect.com/science/article/pii/B9780124186910000071.

[34] B. Lin and V. Giurgiutiu, “Modeling and testing of PZT and PVDF piezoelectric wafer active sensors,” *Smart Materials and Structures*, vol. 15, p. 1085, Jul. 2006. DOI: 10.1088/0964-1726/15/4/022.

[35] P. Groen, *An Introduction to Piezoelectric Materials and Components*. Mar. 2018.

[36] “Piezoelectric sensor : Circuit, specifications, and applications.” (), [Online]. Available: https://www.elprocus.com/what-is-a-piezoelectric-sensor-circuit-specifications-and-applications/. (accessed: 01.07.2022).

[37] B. Lin, V. Giurgiutiu, and P. Pollock, “Durability and survivability of piezoelectric wafer active sensors on metallic structure,” *Aiaa Journal - AIAA J*, vol. 48, Mar. 2010. DOI: 10.2514/1.44776.

[38] A. Raghavan, “Guided-wave structural health monitoring,” Jan. 2007. [Online]. Available: https://deepblue.lib.umich.edu/bitstream/handle/2027.42/77498/Raghavan_PhD_thesis_GWSHM.pdf%3Fsequence%3D1.

[39] V. Giurgiutiu, “Chapter 7 - fiber-optic sensors,” in *Structural Health Monitoring of Aerospace Composites*, V. Giurgiutiu, Ed., Oxford: Academic Press, 2016, pp. 249–296, ISBN: 978-0-12-409605-9. DOI: https://doi.org/10.1016/B978-0-12-409605-9.00007-6. [Online]. Available: https://www.sciencedirect.com/science/article/pii/B9780124096059000076.

[40] R. Di Sante, "Fibre optic sensors for structural health monitoring of aircraft composite structures: Recent advances and applications," *Sensors*, vol. 15, no. 8, pp. 18 666–18 713, 2015, ISSN: 1424-8220. DOI: 10.3390/s150818666. [Online]. Available: https://www.mdpi.com/1424-8220/15/8/18666.

[41] Y. Bai and Q. Bai, "Chapter 7 - Fiber optic monitoring system," in *Subsea Pipeline Integrity and Risk Management*, Y. Bai and Q. Bai, Eds., Boston: Gulf Professional Publishing, 2014, pp. 145–165, ISBN: 978-0-12-394432-0. DOI: https://doi.org/10.1016/B978-0-12-394432-0.00007-X. [Online]. Available: https://www.sciencedirect.com/science/article/pii/B978012394432000007X.

[42] S. Magne, S. Rougeault, M. Vilela, and P. Ferdinand, "State-of-strain evaluation with fiber Bragg grating rosettes: application to discrimination between strain and temperature effects in fiber sensors," *Applied optics*, vol. 36, pp. 9437–47, Jan. 1998. DOI: 10.1364/AO.36.009437.

[43] N. Zhang, C. Davis, W. Chiu, T. Boilard, and M. Bernier, "Fatigue performance of type I fibre Bragg grating strain sensors," *Sensors*, vol. 19, p. 3524, Aug. 2019. DOI: 10.3390/s19163524.

[44] N. Liu, T. Graver, L. Hsu, and J.-P. Ou, "Techniques of advanced FBG sensors: Fabrication, demodulation, encapsulation, and their application in the structural health monitoring of bridges," *Pacific Science Review*, vol. 5, pp. 116–121, Jan. 2003.

[45] B. Tahir, M. Saeed, A. Afaq, *et al.*, "Effect of sensor gauge length on strain sensitivity of a fiber Bragg grating system," *Chinese Journal of Physics*, vol. 49, Oct. 2011.

[46] R. Gafsi and M. A. El-Sherif, "Analysis of induced-birefringence effects on fiber Bragg gratings," *Optical Fiber Technology*, vol. 6, no. 3, pp. 299–323, 2000, ISSN: 1068-5200. DOI: https://doi.org/10.1006/ofte.2000.0333. [Online]. Available: https://www.sciencedirect.com/science/article/pii/S106852000090333X.

[47] FBGS. "Components." (), [Online]. Available: https://fbgs.com/components/. (accessed: 22.08.2022).

[48] ITFTechnologies. "ITF sensor FBG sensors single." (), [Online]. Available: http://www.itftechnologies.com/fbg-sensors-single.html#data-sheet. (accessed: 22.08.2022).

[49] Engionic. "Overview of FBG manufacturing technologies." (), [Online]. Available: https://engionic-femto-gratings.de/en/technology/manufacturing-technologies. (accessed: 22.08.2022).

[50] FOSCO. "What are APC (angled physical contact) fiber connectors?" (), [Online]. Available: https://www.fiberoptics4sale.com/blogs/archive-posts/95041478-what-are-apc-angled-physical-contact-fiber-connectors. (accessed: 22.08.2022).

[51] T. Buck, M. Müller, and A. Koch, "Theoretical assessment of an all-optical temporal low-pass filter for dynamic fiber Bragg grating signals," *Journal of Sensors*, vol. 2011, Jan. 2011. DOI: 10.1155/2011/302380.

[52] M. M. Werneck, R. C. da Silva Barros Allil, and F. V. B. de Nazaré, "Fiber Bragg gratings: Theory, fabrication, and applications - interrogation techniques of fiber Bragg gratings," in SPIE, 2017. DOI: 10.1117/3.2286558.ch6. [Online]. Available: https://lens.org/097-871-984-882-328.

[53] G. Bennett. "All you ever wanted to know about optical transmission bands." (), [Online]. Available: https://www.infinera.com/blog/all-you-ever-wanted-to-know-about-optical-transmission-bands/tag/optical/. (accessed: 21.10.2022).

[54] C. Díaz, C. Leitão, C. Marques, *et al.*, "Low-cost interrogation technique for dynamic measurements with FBG-based devices," *Sensors*, vol. 17, p. 2414, Oct. 2017. DOI: 10.3390/s17102414.

[55] L. B. Jackson, *Digital filters and signal processing: with MATLAB exercises*. 2010, vol. Third Edition, ISBN: 9781475724585. DOI: 10.1007/978-1-4757-2458-5.

[56] Mathworks. "Iir filter design." (), [Online]. Available: https://nl.mathworks.com/help/signal/ug/iir-filter-design.html. (accessed: 31.03.2023).

[57] Mathworks. “FIR filter design.” (), [Online]. Available: https://nl.mathworks.com/help/signal/ug/fir-filter-design.html. (accessed: 31.03.2023).

[58] C. M. Akujuobi, *Wavelets and Wavelet Transform Systems and Their Applications*. Springer International Publishing, 2022. DOI: 10.1007/978-3-030-87528-2.

[59] B.-W. Jang and C.-G. Kim, “Real-time detection of low-velocity impact-induced delamination onset in composite laminates for efficient management of structural health,” *Composites Part B: Engineering*, vol. 123, pp. 124–135, 2017, ISSN: 1359-8368. DOI: https://doi.org/10.1016/j.compositesb.2017.05.019. [Online]. Available: https://www.sciencedirect.com/science/article/pii/S1359836817310016.

[60] H. Kim and H. Melhem, “Damage detection of structures by wavelet analysis,” *Engineering Structures*, vol. 26, no. 3, pp. 347–362, 2004, ISSN: 0141-0296. DOI: https://doi.org/10.1016/j.engstruct.2003.10.008. [Online]. Available: https://www.sciencedirect.com/science/article/pii/S0141029603002517.

[61] T.-P. Le and P. Argoul, “Continuous wavelet transform for modal identification using free decay response,” *Journal of Sound and Vibration*, vol. 277, no. 1, pp. 73–100, 2004, ISSN: 0022-460X. DOI: https://doi.org/10.1016/j.jsv.2003.08.049. [Online]. Available: https://www.sciencedirect.com/science/article/pii/S0022460X03012124.

[62] B.-W. Jang and C.-G. Kim, “Real-time estimation of delamination occurrence induced by low-velocity impact in composite plates using optical fiber sensing system,” *Composite Structures*, vol. 189, pp. 455–462, 2018, ISSN: 0263-8223. DOI: https://doi.org/10.1016/j.compstruct.2018.01.095. [Online]. Available: https://www.sciencedirect.com/science/article/pii/S0263822317319116.

[63] F. Ciampa and M. Meo, “Acoustic emission source localization and velocity determination of the fundamental mode A0 using wavelet analysis and a Newton-based optimization technique,” *Smart Materials and Structures*, vol. 19, no. 4, p. 045 027, Mar. 2010. DOI: 10.1088/0964-1726/19/4/045027. [Online]. Available: https://dx.doi.org/10.1088/0964-1726/19/4/045027.

[64] J.-M. Yang, Z.-W. Yang, and C.-M. Tseng, “Damage detection in stiffened plates by wavelet transform,” *International Journal of Naval Architecture and Ocean Engineering*, vol. 3, no. 2, pp. 126–135, 2011, ISSN: 2092-6782. DOI: https://doi.org/10.2478/IJNAOE-2013-0055. [Online]. Available: https://www.sciencedirect.com/science/article/pii/S2092678216302151.

[65] R. Janeliukstis, S. Rucevskis, P. Akishin, and A. Chate, “Wavelet transform based damage detection in a plate structure,” *Procedia Engineering*, vol. 161, pp. 127–132, 2016, World Multidisciplinary Civil Engineering-Architecture-Urban Planning Symposium 2016, WMCAUS 2016, ISSN: 1877-7058. DOI: https://doi.org/10.1016/j.proeng.2016.08.509. [Online]. Available: https://www.sciencedirect.com/science/article/pii/S1877705816327175.

[66] A. Teolis, *Computational Signal Processing with Wavelets*. Oct. 2017, vol. 1, ISBN: 978-3-319-65747-9. DOI: https://doi.org/10.1007/978-3-319-65747-9. [Online]. Available: https://link.springer.com/book/10.1007/978-3-319-65747-9.

[67] M. Haase and J. Widjajakusuma, “Damage identification based on ridges and maxima lines of the wavelet transform,” *International Journal of Engineering Science*, vol. 41, no. 13, pp. 1423–1443, 2003, Damage and failure analysis of materials, ISSN: 0020-7225. DOI: https://doi.org/10.1016/S0020-7225(03)00026-0. [Online]. Available: https://www.sciencedirect.com/science/article/pii/S0020722503000260.

[68] J. Barros, R. Diego, and M. Apraiz, “Applications of wavelet transform for analysis of harmonic distortion in power systems: A review,” *Instrumentation and Measurement, IEEE Transactions on*, vol. 61, pp. 2604–2611, Oct. 2012. DOI: 10.1109/TIM.2012.2199194.

[69] S. Aggarwal and N. Chugh, “Signal processing techniques for motor imagery brain computer interface: a review,” *Array*, vol. 1-2, p. 100 003, Aug. 2019. DOI: 10.1016/j.array.2019.100003.

[70] E. A. Robinson and S. Treitel, *Digital imaging and deconvolution : the ABCs of seismic exploration and processing*. 2008, ISBN: 9781560801481. DOI: http://dx.doi.org/10.1190/1.9781560801610.

[71] I. Daubechies, *Ten lectures on wavelets*. Society for industrial and applied mathematics, 1992, ISBN: 978-0-89871-274-2. [Online]. Available: https://tudelft.on.worldcat.org/oclc/898887072.

[72] M. G. E. Schneiders, "Wavelets in control engineering," 2001. [Online]. Available: https://research.tue.nl/en/studentTheses/wavelets-in-control-engineering.

[73] MathWorks. "Introduction to wavelet families." (), [Online]. Available: https://nl.mathworks.com/help/wavelet/gs/introduction-to-the-wavelet-families.html#f3-1009153. (accessed: 16.01.2023).

[74] D. Sundararajan, "Sundararajan fundamentals of the discrete haar wavelet transform," 2011. [Online]. Available: https://api.semanticscholar.org/CorpusID:43942486.

[75] PyWavelets. "Wavelet discrete Meyer (FIR approximation) (DMEY)." (), [Online]. Available: https://wavelets.pybytes.com/wavelet/dmey/. (accessed: 20.10.2023).

[76] R. W. Hamming, "Chapter 1 Haar wavelets," 1999. [Online]. Available: https://dsp-book.narod.ru/PWSA/8276_01.pdf.

[77] R. W. Hamming, "Chapter 2 Daubechies wavelets," 1999. [Online]. Available: https://dsp-book.narod.ru/PWSA/8276_02.pdf.

[78] MathWorks. "Extremal phase." (), [Online]. Available: https://nl.mathworks.com/help/wavelet/gs/extremal-phase-wavelet.html. (accessed: 16.01.2023).

[79] Mathworks. "Symaux." (), [Online]. Available: https://nl.mathworks.com/help/wavelet/ref/symaux.html#mw_ec619515-d7bc-4775-aa8f-f4d96b9240f9. (accessed: 14.04.2023).

[80] M. X. Cohen, "A better way to define and describe Morlet wavelets for time-frequency analysis," *bioRxiv*, 2018. DOI: 10.1101/397182. eprint: https://www.biorxiv.org/content/early/2018/08/21/397182.full.pdf. [Online]. Available: https://www.biorxiv.org/content/early/2018/08/21/397182.

[81] Mathworks. "Wavelet families." (), [Online]. Available: https://nl.mathworks.com/help/wavelet/ug/wavelet-families-additional-discussion.html. (accessed: 20.01.2023).

[82] Mathworks. "Waveinfo." (), [Online]. Available: https://nl.mathworks.com/help/wavelet/ref/waveinfo.html. (accessed: 20.01.2023).

[83] H. Zhu, "Wavelet transform for processing power quality disturbances," *EURASIP Journal on Applied Signal Processing*, vol. 2007, pp. 176–176, Dec. 2007. DOI: 10.1155/2007/47695.

[84] MathWorks. "Choose a wavelet." (), [Online]. Available: https://nl.mathworks.com/help/wavelet/gs/choose-a-wavelet.html. (accessed: 14.04.2023).

[85] M. Gherlone, P. Cerracchio, M. Mattone, M. Di Sciuva, and A. Tessler, "An inverse finite element method for beam shape sensing: Theoretical framework and experimental validation," *Smart Materials and Structures*, vol. 23, p. 045 027, Mar. 2014. DOI: 10.1088/0964-1726/23/4/045027.

[86] L. Colombo, D. Oboe, C. Sbarufatti, F. Cadini, S. Russo, and M. Giglio, "Shape sensing and damage identification with iFEM on a composite structure subjected to impact damage and non-trivial boundary conditions," *Mechanical Systems and Signal Processing*, vol. 148, p. 107 163, 2021, ISSN: 0888-3270. DOI: https://doi.org/10.1016/j.ymssp.2020.107163. [Online]. Available: https://www.sciencedirect.com/science/article/pii/S0888327020305495.

[87] M. Abambres, M. Marcy, and G. Doz, "Potential of Neural Networks for Structural Damage Localization," Dec. 2021. DOI: 10.36227/techrxiv.12672194.v2. [Online]. Available: https://www.techrxiv.org/articles/preprint/Potential_of_Neural_Networks_for_Structural_Damage_Localization/12672194.

[88] N. P. Raut, A. Kolekar, and S. Gombi, “Optimization techniques for damage detection of composite structure: a review,” *Materials Today: Proceedings*, vol. 45, pp. 4830–4834, 2021, Second International Conference on Aspects of Materials Science and Engineering (ICAMSE 2021), ISSN: 2214-7853. DOI: https://doi.org/10.1016/j.matpr.2021.01.295. [Online]. Available: https://www.sciencedirect.com/science/article/pii/S2214785321003849.

[89] B.-W. Jang and C.-G. Kim, “Impact localization on a composite stiffened panel using reference signals with efficient training process,” *Composites Part B: Engineering*, vol. 94, pp. 271–285, 2016, ISSN: 1359-8368. DOI: https://doi.org/10.1016/j.compositesb.2016.03.063. [Online]. Available: https://www.sciencedirect.com/science/article/pii/S1359836816301081.

[90] Q. H. Doan, T. Le, and D.-K. Thai, “Optimization strategies of neural networks for impact damage classification of RC panels in a small dataset,” *Applied Soft Computing*, vol. 102, p. 107 100, 2021, ISSN: 1568-4946. DOI: https://doi.org/10.1016/j.asoc.2021.107100. [Online]. Available: https://www.sciencedirect.com/science/article/pii/S1568494621000235.

[91] A. Califano, N. Chandarana, L. Grassia, A. D’Amore, and C. Soutis, “Damage detection in composites by artificial neural networks trained by using in situ distributed strains,” *Applied Composite Materials*, Oct. 2020. DOI: 10.1007/s10443-020-09829-z.

[92] A. Datteo, G. Busca, G. Quattromani, and A. Cigada, “On the use of ar models for SHM: A global sensitivity and uncertainty analysis framework,” *Reliability Engineering & System Safety*, vol. 170, pp. 99–115, 2018, ISSN: 0951-8320. DOI: https://doi.org/10.1016/j.ress.2017.10.017. [Online]. Available: https://www.sciencedirect.com/science/article/pii/S0951832017302557.

[93] D. Nardi, L. Lampani, M. Pasquali, and P. Gaudenzi, “Detection of low-velocity impact-induced delaminations in composite laminates using auto-regressive models,” *Composite Structures*, vol. 151, pp. 108–113, 2016, Smart composites and composite structures In honour of the 70th anniversary of Professor Carlos Alberto Mota Soares, ISSN: 0263-8223. DOI: https://doi.org/10.1016/j.compstruct.2016.02.005. [Online]. Available: https://www.sciencedirect.com/science/article/pii/S0263822316300253.

[94] B. Zamorano and N. Elvin, “Passive high-speed impact damage assessment in composite panels using embedded piezoelectric sensors,” *Journal of Intelligent Material Systems and Structures*, vol. 27, no. 1, pp. 104–116, 2016. DOI: 10.1177/1045389X14560368. eprint: https://doi.org/10.1177/1045389X14560368. [Online]. Available: https://doi.org/10.1177/1045389X14560368.

[95] A. De Luca, D. Perfetto, A. De Fenza, G. Petrone, and F. Caputo, “Guided wave SHM system for damage detection in complex composite structure,” *Theoretical and Applied Fracture Mechanics*, vol. 105, p. 102 408, 2020, ISSN: 0167-8442. DOI: https://doi.org/10.1016/j.tafmec.2019.102408. [Online]. Available: https://www.sciencedirect.com/science/article/pii/S0167844219302460.

[96] D.-U. Sung, C.-G. Kim, and C.-S. Hong, “Monitoring of impact damages in composite laminates using wavelet transform,” *Composites Part B: Engineering*, vol. 33, no. 1, pp. 35–43, 2002, ISSN: 1359-8368. DOI: https://doi.org/10.1016/S1359-8368(01)00051-8. [Online]. Available: https://www.sciencedirect.com/science/article/pii/S1359836801000518.

[97] B.-W. Jang, S.-O. Park, Y.-G. Lee, C.-G. Kim, and C.-Y. Park, “Detection of impact damage in composite structures using high speed FBG interrogator,” *Advanced Composite Materials*, vol. 21, no. 1, pp. 29–44, 2012. DOI: 10.1163/156855111X620874. eprint: https://www.tandfonline.com/doi/pdf/10.1163/156855111X620874. [Online]. Available: https://www.tandfonline.com/doi/abs/10.1163/156855111X620874.

[98] A. Huber, *The dispersion calculator: An open source software for calculating dispersion curves and mode shapes of guided waves*, version v2.4. [Online]. Available: https://www.dlr.de/zlp/en/desktopdefault.aspx/tabid-14332/24874_read-61142.

[99] TenCate. “Tencate Cetex and CFRT thermoplastic advanced composites.” (), [Online]. Available: https://pdf.aeroexpo.online/pdf/toray-advanced-composites/tencate-cetex-thermoplastic-brochure/172149-4521.html. (accessed: 23-03-2023).

[100] R. Olsson, “Mass criterion for wave controlled impact response of composite plates,” *Composites Part A: Applied Science and Manufacturing*, vol. 31, no. 8, pp. 879–887, 2000, ISSN: 1359-835X. DOI: https://doi.org/10.1016/S1359-835X(00)00020-8. [Online]. Available: https://www.sciencedirect.com/science/article/pii/S1359835X00000208.

A

Test plan composite square panel impact damage tests

A.1. Test plan

Introduction This work instruction describes impact tests to be performed on a square (1x1 m) composite plate planned on 12 May, 31 May and 15 September 2023. The tests are executed to collect impact response data for two different sensor types (FBG and PZT). During the tests in May, non-damaging low impact energy impacts are performed, followed by higher impact energy tests. The higher energy impacts will initially cause small damages and will be characterized by means of an active SHM phased array scan. During the tests in September, larger damages will be initiated, up to a puncture in the panel. These damages will also be characterized by a phased array scan. The impact tests will be performed at room temperature using the drop tower. Duration of the test is estimated at 3 days.

Preparation

- Stripped and recoated FBG sensors for the FBGT system (8 sensors) should be installed on the composite plate using Z70 adhesive
- Test article should be firmly mounted to the table with aluminium clamping frame, which cannot move during testing.
- PZT sensors should be applied on the bottom of the test panel.
- All measuring equipment should be available and functionally checked before testing.

Equipment

- Composite square plate (1x1 m) with installed FBGs and PZTs
- Aluminium support frame, adjusted for more stiffness due to boundary condition tests
- Drop tower Redondo FBGT-M1200
- Technobis Gator (on Redondo FAESense fibre)
- Handyscope HS6 + HS5
- Phased array Omniscan-M-PA16-128
- Rotronic Hygrometer

A.1.1. Reference documents

- Manuals of the used equipment.
- Previous impact “prove of concept” test: TH-01-WI-002-FG SquarePanel tests (available at NLR).

A.1.2. Preparation activities

Test object The test object is a flat PEKK AS4D composite panel with the dimensions of 1000 x 1000 mm (length x width) consisting of a quasi-isotropic lay-up $[-45, 0, +45, 90]_{3S}$ with a ply thickness of 0.14 mm, which can be seen in Figure A.1. The panel is clamped within an aluminium support frame,

of which the frame is also shown in Figure A.1. Bolts along the clamping frame allow for a tight fixture of the composite panel during testing. The panel fixed in the frame, is clamped as whole to a heavy steel table, which prevents the test set-up from moving during testing. The clamps holding the panel to the table will be fixed tight and will not be adjusted during testing, to prevent results from being altered. This means that the orientation of the panel compared to the table will be the same during testing.

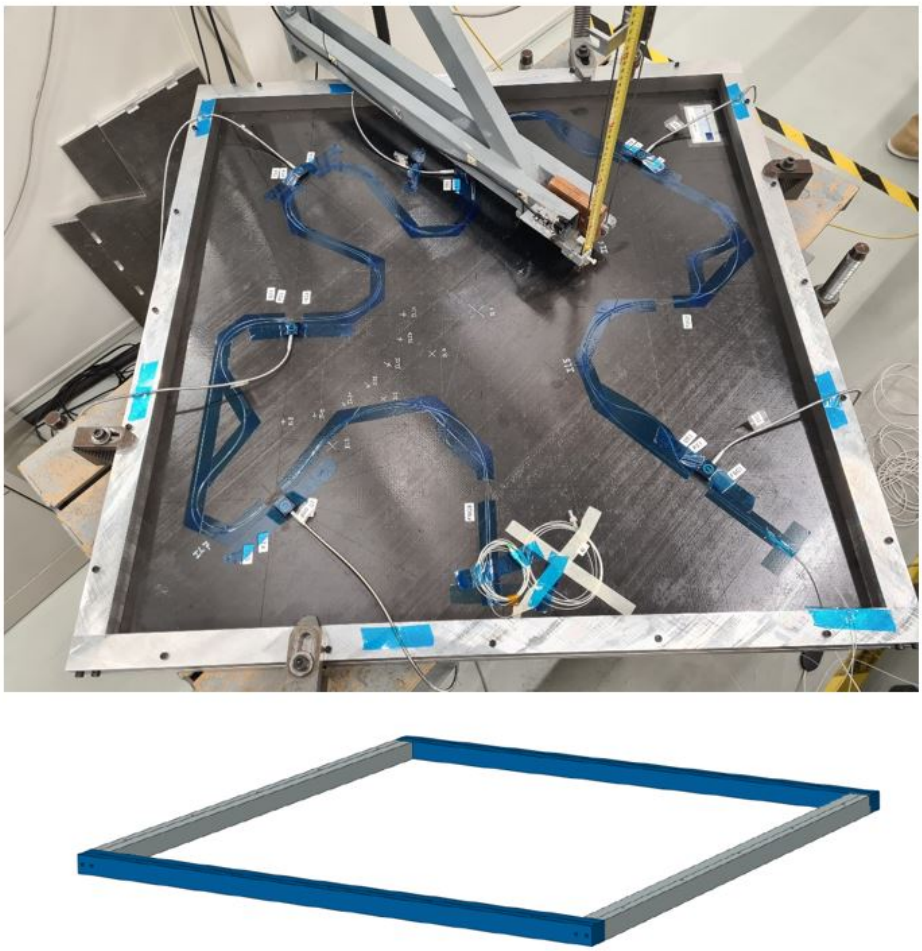

Figure A.1: Square composite plate with an aluminium clamping frame, allowing for fixed boundary conditions (with dimensions 40(w) x 1040(l) x 55(h) mm) along the specimen.

Test set-up Figure A.2 shows the test set-up used during the tests, including (from left to right) equipment for the Optics11, FBGT-M1200, Technobis Gator and the PZT systems. The drop tower also consists of calculating and monitoring software for calculating the time-force curves and returning the real and rebound impact energy in Joules (J). The two laptops to the right are used for gathering test observations. Figure A.3 shows the drop tower set-up, consisting of a heavy table to secure the panel and its frame, a ruler to determine drop height and the impactor on guidelines. The impactor is fitted with an adjustable weight, adjustable impactor diameter and a force measuring device. The data of the Optics11 and Technobis Gator systems are not used for this thesis, but is included for data gathering for NLR.

Mark sensor and impact locations on the plate The coordinate system of the test panel is shown in Figure A.4. The coordinate system is divided in sections (marked by the dashed line), to precisely locate the sensors and impact locations. The impact locations marked with a red star are the where the non-damaging and small damages are created on the 12th and 31st of May. The impact locations marked with a yellow star are the locations where additional impact tests have been performed on the 15th of

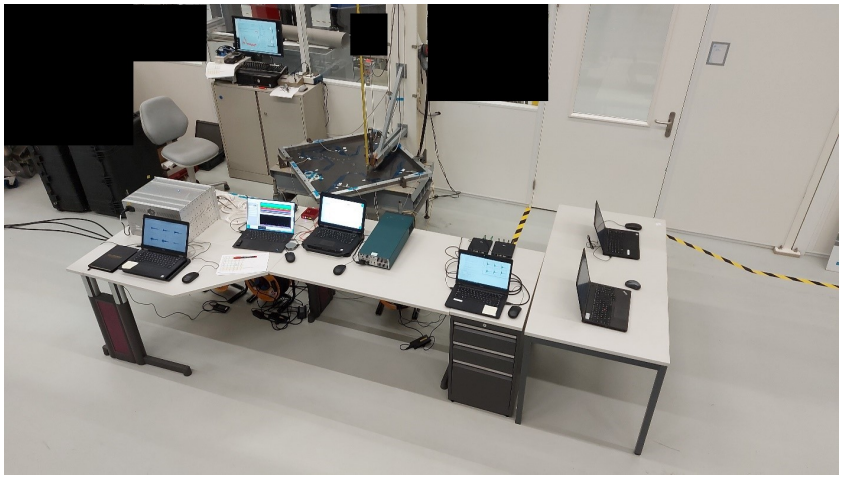

Figure A.2: Test set-up

Figure A.3: Drop tower

September. This Figure also indicates the sensor positions and sensor orientations. Prior to testing, the coordinates and orientation of the FBGs and PZTs should be measured/determined and marked with a white marker (impact locations) and stickers (sensor positions). The measurement values are to be inserted in Table A.1.

Installation of the FBG sensors Eight FBG sensors will be installed on the composite plate for the FBGT system, see Figure A.4, using Z70 adhesive. The remainder of the fibre will be mounted to the plate with Kapton tape to stop fibre movement during testing.

Take photographs of all sensors and impact locations Take a detailed photograph of each sensor and of the whole plate for reference.

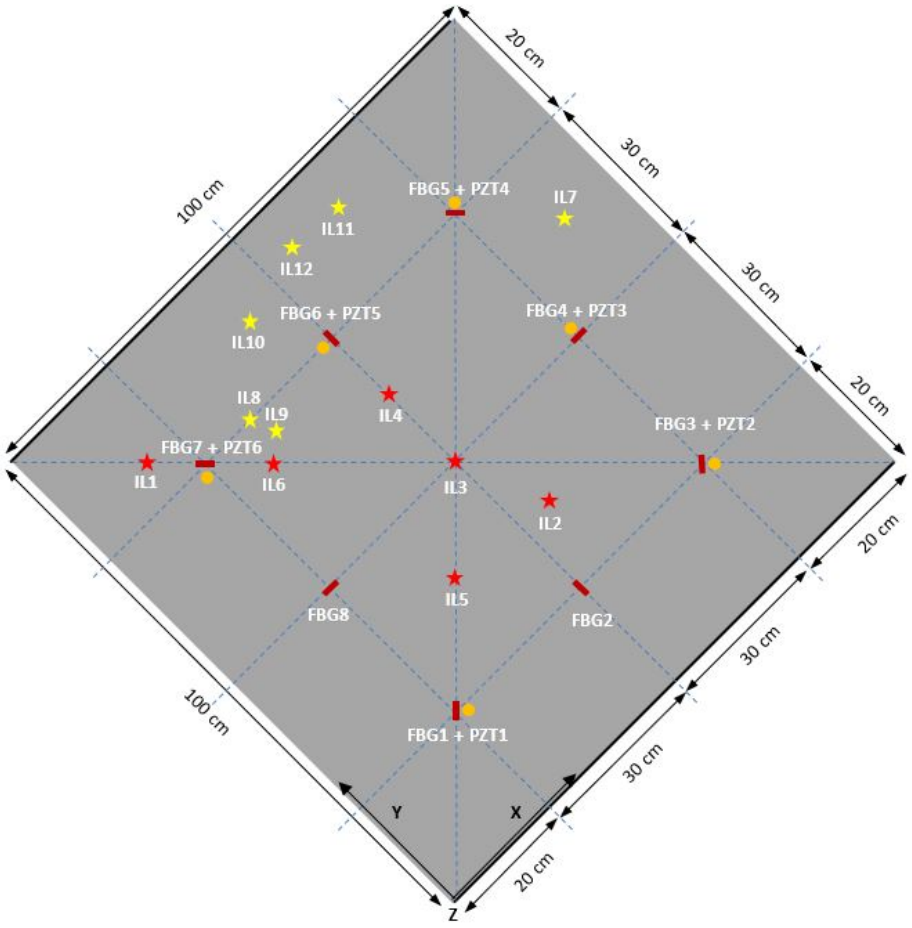

Figure A.4: Impact locations (⋆ IL) and sensor locations (▬ FBG ● PZT) , Figure not scaled.

Mount the plate to the drop tower table after installation of all sensors The plate will be mounted at all four edges in an aluminium frame that will be clamped to the drop tower table by means of clamps. The table is made of steel and does not allow for any movement of the set-up during testing. The clamps prevent the clamped plate to move in respect to the table during testing.

Connect the measurement equipment Connect the optical fibres to the interrogators and check correct operation of the system and note the nominal wavelength of each FBG in Table A.1 using the FAE Sense software. Import the saved settings .uni file into the software to assure the same settings during each test. Connect the six piezoelectric sensors to the DAC and check correct operation of the system and note the channel numbers in Table A.1. Set the system sampling frequency to the required settings.

Prepare the drop tower impactor Several impact head diameters are available: 6, 16, 25.4 and 50 mm. For both tests in May, only the 16 mm impactor will be used. During the first day of testing, the impactor has a total mass of 1.154 kg. The second day of testing, the weight of the impactor is increased to 2.356 kg. The final day of testing, the impactor mas is increased to 5.658 kg with the 50mm impactor diameter. To create a penetration, the impactor diameter is changed to 16 mm, leading to a total mass of 5.504 kg. The impactor should be checked on proper functioning with a low energy level impact on a scrap wooden piece. The software will measure the real impact and rebound energy after each test.

Peripheral equipment

- Laptops with installed DAC and FAE Sense software (NLR)
- Drop tower

Table A.1: Sensor and impact locations for Composite plate, measured from the inside of the boundary conditions.

	x-location (mm)	y-location (mm)	Sensor angle (degrees), angle measured from x-axis	Nominal wavelength FBGT (nm)	Channel number FBGT	Channel number Gator
FBG1	*178*	*179*	*45*	*1529.67*	*9*	*1*
FBG2	*479*	*178*	*90*	*1534.82*	*13*	*2*
FBG3	*779*	*182*	*45*	*1539.84*	*10*	*3*
FBG4	*778*	*477*	*0*	*1543.70*	*3*	*4*
FBG5	*777*	*780*	*-45*	*1548.48*	*7*	*5*
FBG6	*474*	*779*	*90*	*1553.63*	*2*	*6*
FBG7	*177*	*779*	*-45*	*1558.35*	*6*	*7*
FBG8	*178*	*478*	*0*	*1563.13*	*1*	*8*
	x-location (mm)	**y-location (mm)**	**Sensor angle (degrees), angle measured from x-axis**	**Channel number PZT**		
PZT1	*188*	*172*	*-*	*CH1*		
PZT2	*768*	*174*	*0*	*CH2*		
PZT3	*779*	*481*	*0*	*CH3*		
PZT4	*779*	*781*	*-45*	*CH4*		
PZT5	*478*	*780*	*90*	*CH5*		
PZT6	*188*	*786*	*0*	*CH6*		
IL1	*112*	*844*	*-*	*-*		
IL2	*574*	*280*	*-*	*-*		
IL3	*477*	*479*	*-*	*-*		
IL4	*477*	*600*	*-*	*-*		
IL5	*349*	*348*	*-*	*-*		
IL6	*254*	*702*	*-*	*-*		
IL7	*870*	*610*	*-*	*-*		
IL8	*293*	*781*	*-*	*-*		
IL9	*306*	*733*	*-*	*-*		
IL10	*405*	*840*	*-*	*-*		
IL11	*606*	*891*	*-*	*-*		
IL12	*536*	*888*	*-*	*-*		

- Writing desks
- Power supplies
- Rotronic temperature and humidity measuring device

Photo capture

Photo camera to take photographs of the test setup, mainly with smartphones.

DAQ systems

- Rotronic temperature and humidity measuring device, represented in Figure A.5.
- Redondo Optics interrogator FBGT-M1200, represented in Figure A.6. The FAE Sense software, provided with the Redondo interrogator system, will be used for data acquisition and storage for later signal analysis.
- Phased array Omniscan-M-PA16-128 active measuring system with ultrasonic gel, represented in Figure A.7.
- Handyscope HS6D-500 DIFF USB-oscilloscope + HS5 from NLR for active/passive PZT measurement, represented in Figure A.8.

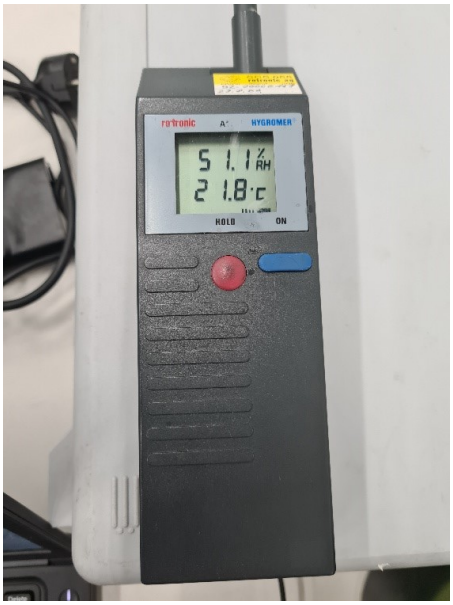

Figure A.5: Rotronic temperature and humidity measuring device.

Figure A.6: Redondo Optics interrogator FBGT-M1200.

Figure A.7: Phased array Omniscan-M-PA16-128.

A.1.3. Execution of impact tests

Record the test environmental conditions and relative humidity before and after the test and insert the values in Table A.2. The order of impacts at the locations on the individual test dates are:

- 12 May: IL2, IL3, IL4, IL5, IL6 and last IL1
- 31 May: IL2, IL3, IL6 and last IL1

Figure A.8: Handyscope HS6D-500 DIFF USB-oscilloscope (left) and HS5 (right).

- 15 September: IL8, IL7, IL9, IL10, IL11 and last IL12

Table A.2: Environmental conditions on the three testing days

12-5-2023				
Plate ID	**Temperature before testing ($^{\circ}C$)**	**Humidity before testing (%)**	**Temperature after testing ($^{\circ}C$)**	**Humidity after testing (%)**
COMP	*21.8*	*51.1*	*22.4*	*47.7*

31-5-2023				
Plate ID	**Temperature before testing ($^{\circ}C$)**	**Humidity before testing (%)**	**Temperature after testing ($^{\circ}C$)**	**Humidity after testing (%)**
COMP	*21.8*	*45.9*	*23.0*	*49.8*

15-9-2023				
Plate ID	**Temperature before testing ($^{\circ}C$)**	**Humidity before testing (%)**	**Temperature after testing ($^{\circ}C$)**	**Humidity after testing (%)**
COMP	*22.0*	*44.3*	*23.9*	*44.8*

The results and observations are included in a test matrix, including all parameters and the remarks which were noticed. The impact energies will be increased after every non-damaging impact test, which makes this the reference signal. Impact energies are then increased. After a damage is spotted, active SHM (phased array scan) will be applied to confirm if damage is present. If no damage is present, the impact energy will be increased on that location. During testing on all three days, some additional remarks have been noted. These remarks can have effect on the response signals or feature extraction and are therefor necessary to address in this Section.

Remarks during tests on 12 May 2023:

- The FBG sensors 1, 2 and 3 do not give good responses, for which more details are given in Section A.2.
- During the proof of concept tests, performed before the damaging impact tests (TH-01-WI-002-FG SquarePanel tests), it was proven that the software was not fully compatible with the hardware (FBGT-M1200 and the fibre). This issue is within the LabView driver, used for USB data transmission. The problems were not fixed yet and therefor had effect on the results. The main effect is that data gets lost during measurement, shown as large data shifts in the signal amplitude. Some signals, or parts in that signal, may therefor be irrelevant.
- Although the system was calibrated by means of the instructions and the experience of previous tests, the signals seemed to slightly shift in baseline voltage during the day. This can be due to the system reaching higher temperatures, but also due to environmental conditions. This needs to be taken into account during data analysis.
- During impacts, the sensor PZT6 at IL1 came loose at higher energy impacts. To avoid the sensor coming loose again during higher energy impacts, IL1 will be the last location where damaging impacts will be induced. The reason why the sensor came loose is most likely caused by effect of the boundary conditions at IL1 after an impact. The sensor functioned correctly after refitting it to the panel, also at high energy impacts/

- The temperature during testing increased slightly, but it stayed within the region where no correction has to be made for the FBGT-M1200 results.
- Damages are assessed by visual inspection, after which is decided to apply a phased array scan or not. To keep track of the decisions made, the remarks are added in the test matrix.
- As 40J impacts at IL6 did not lead to big damages yet, it has been decided to increase the interval between different impacts to 10J. This decision has been made as IL6 is the closest to boundary conditions compared to the other impact locations within the sensor network and should have damage at lower impact energies compared to the other locations. This, due to the increased flexural behaviour of the panel further away from the boundary conditions.
- PZT sampling rate has been fixed to 100kHz, to prevent the data files requiring much data storage space.
- The measured data rate of the FBGT system shifts between the 7.1 - 7.5 MHz during testing. The fixed sampling frequency is set at 7.5 MHz over 8 FBG channels (1 channel is 1 FBG). This leads to a fixed sampling frequency of 937.5 kHz per FBG.
- The Gator system was attached to a fibre which was optimized for the FBGT-M1200 system. The expected results of the Gator are therefor poor, but can maybe still be used for signal analysis.

Remarks during tests on 31 May 2023:

- The software and test set-up are exactly the same as during the tests on 12 May 2023. FAESense calibration has been slightly adjusted, to increase the system performance.
- The PZT sampling frequency has been set to 100 kHz.
- As higher energies could not be reached with the 1.154 kg weight (height of the drop tower was the limiting factor), the weight was doubled. Lower, non-damaging impacts, were performed again, to compare the results of the effect of a different impactor weight.
- The increase in energy level interval was changed at IL1 and IL6 to 5J increments due to these locations being close to the boundary conditions. Damages are expected to be achieved at lower impact energies, compared to the other impact locations within the sensor network. The other locations keep the 10J increment of impact energy.
- During the impact with ID39, the panel hit the steel table. It was decided to lift the panel compared to the steel table, to prevent the panel hitting the table again. The impact was repeated and the panel stayed clear of the table.
- Two locations were not impacted due to the testing time and the fact that enough data (100 impacts) was gathered for signal analysis.

Remarks during tests on 15 September 2023

- The software and test set-up are exactly the same as during the tests on 12 and 31 May 2023. The FAESense calibration has been used from the latest impact tests and has not been adjusted.
- PZT sampling frequency has been set to 1 MHz to achieve nearly the same amount of data points as the FAESense system.
- IL1 and IL6 could not be impacted with the bigger diameter impactor tip and the optical fibre being to close to the impact location. The fibre would be damaged if these locations were chosen. Therefore other locations IL7 and IL8 have been chosen.
- During testing, the sensor response if PZT1 and PZT2 are not good. This means that this data from these sensors should not be used for signal analysis.
- When the 170J impact on IL8 was performed and no significant damage has been found, the theory was that the location was damaged at the dented location, not being able to have the desired load transfer in the panel to induce for instance delaminations. On the other locations, only 2 impacts were induced; 1 low energy non-damaging impact after which a damaging impact at high energy levels was performed.
- Because no significant damages were induced by the 50 mm impactor diameter at IL8, other than dents and some fibre breakage at the bottom of the panel at the impact locations, it has been decided to decrease the impactor diameter to 16 mm and keep the impactor weight the same. Due to the smaller mass of the impactor tip, the mass was set to 5.504 kg. Impact locations 7, 9, 10, 11 and 12 were impacted with this set-up.

A.2. Test plan explanation

The test plan of the impact tests on the square composite panel is presented in this appendix. The choices made for the tests will be represented and discussed here. These choices consist of the panel characteristics, boundary conditions, sensor types, sensor locations, sensor orientation, impact locations, impactor characteristics, interrogation method and the active SHM method.

Composite panel characteristics The panel that will be tested is a 1-by-1 meter square panel, fabricated with a Polyetherketoneketone (PEKK) semi-crystalline thermoplastic polymer. This is a aerospace grade composite material used in aircraft structures such as leading edges, pylons, panels, stiffeners, brackets and interior design. The properties of the panel are given in Table A.3. Prior to the first test, some non-damaging impacts have been performed to test the systems used during this damaging test. The panel is thus undamaged prior to the impact damage tests, confirmed by performing a phased array scan before the damaging tests.

Table A.3: Square panel material properties and engineering constants. [99]

SQUARE PANEL MATERIAL PROPERTIES AND ENGINEERING CONSTANTS	
Material	PEKK AS4D
Resin	Polyetherketoneketone (PEKK)
Fibre	AS4D
Glass transition temperature	$160°C$
Cure temperature	$371°C$
Lay-up	Quasi Isotropic $[-45, 0, +45, 90]_{3s}$
Plies	24 plies
Ply thickness	0.14 mm
$E1$	136.528 GPa
$E2$	4.214 GPa
$E3$	10.734 GPa
G_{12}	4.214 GPa
G_{13}	4.214 GPa
G_{23}	4.214 GPa
υ_{12}	0.43
υ_{13}	0.48
υ_{23}	0.53
ρ	1590 kg/m^3

Boundary conditions The boundary conditions will be fully clamped, ensuring that the plate will be clamped at the edges in all three dimensions. In other words, the displacements and rotations at the boundary conditions will be constrained. This means that when the wave arrives at the boundary condition, it is rotated 180 degrees upon reflection. Free or hinged boundary conditions are not chosen, to prevent rotations at the boundary conditions to happen. The boundary conditions have been stiffened after the conclusion that the previous clamping mechanism was not sufficient for the given impact table. The table is physically smaller than the panel. The overhang of the panel requires a stiffer clamping frame to better suppress the vibrations. These tests were done to test the newly received FBG systems as proof of concept of the system.

When performing impacts on panels of all materials, one must take into account that the duration of the impact leads to different types of panel responses. Olsson [100] showed in his paper that the response of the panel is primarily determined by the impact duration and mass ratio of the panel and

the impactor, rather than the velocity of the impactor. Large impact masses tend to generate quasi-static responses which are strongly dependent on the panel size and the boundary conditions. Low impact masses generate responses which are not dependent on the plate size or the applied boundary conditions. Small impact times are defined as impacts that last shorter than the propagation time of through-the-thickness waves, of which dilatational waves are the dominant wave form. When impact times are larger (boundary conditions are not reached by a major wave before the impact is over), flexural waves dominate. For much large impact times, the boundary conditions are affecting the wave responses, leading to quasi-static responses. These responses are visually represented in Figure A.9. BVIDs are most often caused by the short and long impact times. [100]

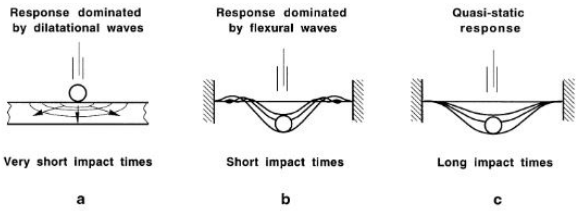

Figure A.9: Impact responses of the panel with a very short impact time (a), a short impact time (b) and a long impact time (c), taken from [100]

Impactor masses that are smaller than $\frac{1}{5}$ of the affected plate mass, lead to responses that are dominated by flexural waves. Impactors that are twice as heavy as the mass of the panel, lead to a quasi-static response. [100]

Sensor types During the test, two types of sensors will be used for passive SHM. The thesis will focus on the FBG sensors, as the state-of-the-art FBG interrogation system is based on optical signals. As this method is not yet proven, PZT sensors will also be used. These sensors and interrogation methods are well understood and allow for FBG signal validation. In total eight FBGs are located on the panel, at which PZT sensors are located at six of these locations.

Sensor locations The PZT and FBG sensors are located as such, that a sensor network is formed. The sensors are put 20 cm away from the boundary conditions, to delay boundary condition interference upon reflection and also to create a large area within the sensor network in which the impacts can occur. This also allows for tests of impacts outside the sensor network, to investigate the influence of the impact location regarding damage characteristics in the response signal. Also, the quality of the sensor response is taken into account. During previous conceptual tests with the FBGT-M1200 system, the FBG sensors 1, 2 and 3 gave a bad signal response compared to the calibrated Technobis Gator system. This can be clearly seen in Figure A.10 where the Gator and the FBGT-M1200 results on the same optical fibre (with the same sensors) are shown. FBG1, FBG2 and FBG3 show clear deviations on the signal response compared to the other FBGs.

Sensor orientation The sensor location is also taken into account in the test plan. As stated in 3 the sensor orientation of FBGs have influence on the signal response. Placing the sensor parallel to the propagation direction of the wave, theoretically gives better results than placing them perpendicular to the wave propagation direction. To test if this is also valid for real-time impact damage testing, the sensors are placed in 0^o, 45^o and 90^o orientations, compared to the defined coordinate system in the test plan.

Impact locations There will be in total twelve locations at which damaging impacts will occur, hereafter indicated by impact locations (IL). IL1 to IL6 are impacted on 12 and 31 May. IL7 to IL12 are impacted on 15 September. Regarding the knowledge gathered by performing all the impacts over a total of three days, the locations are chosen as discussed below:

- IL1: This location is chosen to determine if the sensors are capable of detecting damage events after impact outside of the sensor network, which is close to two boundary conditions and the FBG sensor 7. This sensor is placed parallel (0^o offset) to the propagation direction of the impact

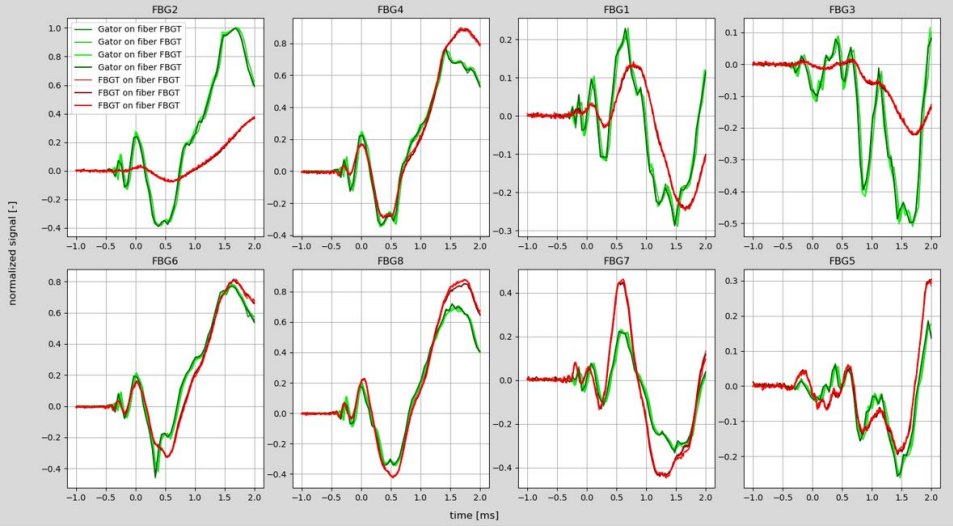

Figure A.10: Gator and FBGT-M1200 sensor response when connected to the same fibre.

waves, ensuring optimal sensor response. PZT6 will also record at the same location as FBG7. This will be the last location that will be impacted during testing.

- IL2: This location is chosen to have an impact close to FBG sensors 1, 2 and 3 (PZTs 1 and 2), also introducing an slight offset in the angle of the impact. This, to have different results compared to impact location 4. This is the first location to be damaged, thus no other damages can affect the results at any sensor on the panel. The location is also determined to overcome interference of the impacts at location 3.
- IL3: This IL is chosen as it is at the center of the sensor network. The sensors should all have the same time of arrivals, so the comparison should similar. It is possible that the introduced damage at location 2 may affect the results at the FBG sensors 1, 2 and 3 (and PZTs 1 and 2). The differences in response due to sensor orientation, and thus angle of incidence of the wave at which it propagates to the sensor, can be shown with these results.
- IL4: This location is chosen to get signal responses from the FBGs 5, 6 and 7 (PZTs 4, 5 and 6), which will not be affected by the damage introduced at IL3. The FBG sensor 5 and 7 are in the same orientation, but the angle of the propagating wave will be different at both sensors.
- IL5: This location will initiate an impact close to FBG sensors 1, 2 and 8, (and PZT 1). FBG1 is oriented parallel to the wave propagation direction, leading to optimal responses at this sensor. Testing the 45^o angle of FBG 2 and 8 compared to the wave propagation direction is also included.
- IL6: This location is chosen to determine the sensor FBG7 (and PZT6) reaction with a close impact to the sensor (0^o offset compared to signal propagation). IL2 to IL5 are damaged and may affect the response signals at sensors other than FBGs 6, 7 and 8 (and PZTs 4, 5 and 6).
- IL7: This is a location outside of the sensor network, close to the boundary conditions. This location was impacted in stead of IL1 due to the fibre being to close to the impact location with the larger impactor size. Also, FBG4 and FBG5, together with PZT3 and PZT4, are oriented in a suitable manner compared to the wave propagation direction. Other locations near two boundary conditions (similar to IL1 at different corners) are not chosen, as the FBG sensors along the x-axis do not return the best results and due to the FBG sensor orientations of FBG4, FBG5 and FBG6.
- IL8: This location is chosen as other low impact energy impacts have been performed here. Ik is also near good sensors and still within the sensor network.
- IL9: This location is chosen as alternative for IL6 (from previous tests), to prevent to do impacts on a already slightly damaged IL. IL9 is close to IL6, which will also give good results by the nearby sensors.

- IL10: This location is chosen to do impacts outside of the sensor network, halve way in between the boundary conditions and the sensor network.
- IL11 and IL12: They are both chosen as similar impact locations, but slightly apart, as the second impact energy levels of both locations are changed significantly. IL11 will be tested with 2 impacts of 30J and 100J to try and create a delamination. IL12 is impacted with 20J and 170J respectively to create a significant puncture. These locations are also chosen, as experience from other impacts have shown that impacts within the sensor network take a lot of energy to create a small damage. This has to do with the low stiffness this panel has and therefore the freedom of flexing upon an impact.

The impact locations are separated as far from each other as possible, to limit the effect of the already induced damages during impacts. During the measurements, more damages are within the panel, weakening it. Though, the impact order is chosen as such that this effect is as minimal as possible but to also create enough data for the signal analysis on a sufficient amount of impact locations.

Impactor characteristics Several impactors are present at NLR, which allow for different impactors and weights. To minimize the data variables, a constant diameter for the impactor is selected at a single impact location. Also the weight is kept constant as much as possible during testing at a single IL. During testing, the impactor weight and diameter can be changed accordingly to induce different types of damages. The details of the diameter and weight are shown in Appendix A.

Interrogation method The miniature FBG Transceiver to be used for this analysis is the Redondo Optics FBGT-M1200, which has the capability of sensing 12 FBGs on a single fibre. It is capable of monitoring stress-strain relations, temperature shifts and vibrations using the wavelength division multiplexing method. The light source operates in the C-band, for which every single FBG has its own detection channel. The demodulation technique is based on AWG. The sampling frequency is 500 kHz for on a single channel based on the FBGT-M1200 datasheet. In practice, the sampling frequency seems to be higher (937.5 kHz), which will be further analyzed during the signal analysis. The system has two light sources of which the first is a semiconductor optical amplification (SOA) light source and the second a superluminescent diode (SL(E)D). The SOA was implemented by the manufacturer to broaden the bandwidth of the light source, but in practice this does not work. Therefore, only the SLED will be used as broadband light source.

Active SHM method Active SHM will be used to classify the damages due to the impacts. The active SHM data will be acquired using a phased array omniscan-M-PA16-128 measuring system. For better coupling between the panel and the roller, an acoustic couplant is sprayed over the are which is to be scanned.

B

Impact test damage overview

This appendix shows the damages initiated from all impact tests on all locations. The sub-figures (a) consist of a top view, bottom view and the active A-, B-, C- and D-scan results. An A-scan is the most basic representation and shows the wave amplitude and transit time (waveform). The top scan is a C-scan representing the attenuation on the backwall over the panel from the top view. The plain white area marks the location where the phased array scanner cannot make contact to the panel, which is the dent due to the impact. The middle scan is the inverse value (reflection) of the top C-scan, indicating the area of the damaged parts. The higher the intensity, e.g. the more red it becomes, the higher the extent of the damage. The bottom scan is a through the thickness B-scan, where the top line is the front wall, the second orange line is the backwall and the additional bottom blue lines is the reflection of the backwall. These reflections are not representing the panel anymore and will not be used for further analysis. The bottom right plot is the cross-sectional view (D-scan) of the damaged area, in which the layers are the same as the B-scan (front wall, back wall and back wall reflections). The repeat echo of a damage can be visible when the distance between the damaged layer and its reflection is the same as the distance from the first ply to that specific damage. The reflection does not indicate an additional damage and is lower in intensity than the damage of which it is a reflection of.

In addition to the active scan results, the area of the damaged location is calculated. The Figures used for this calculation are included in the sub-figures (b) and (c) for all impact locations. Based on the image pixels and the x- and y-axis scale from the Omniscan system, the area of the damaged location can be approximated. This is done by converting the selected image to a binary image, from which the black pixels (indicating the damaged location) are determined. Converting this back to an area size, using the scale and the amount of pixels, returns the area in SI-units. The left picture of sub-figures (b) display the cutout of the reflection C-scan, containing the inner damaged area data. The right picture shows the binary image of that location, also called the montage of the damaged area. Sub-figures (c) contain the blend of the cutout and the binary image. This allows for a quick overview how well the binary image area approaches the cutout area. This area calculation method does not return exact area calculations, but do approach the damaged area sufficiently for this analysis. The areas of the damages at each location are included in Table B.1 for the flat panel and in Table B.2 for the stiffened panel.

B.1. Flat panel

IL1

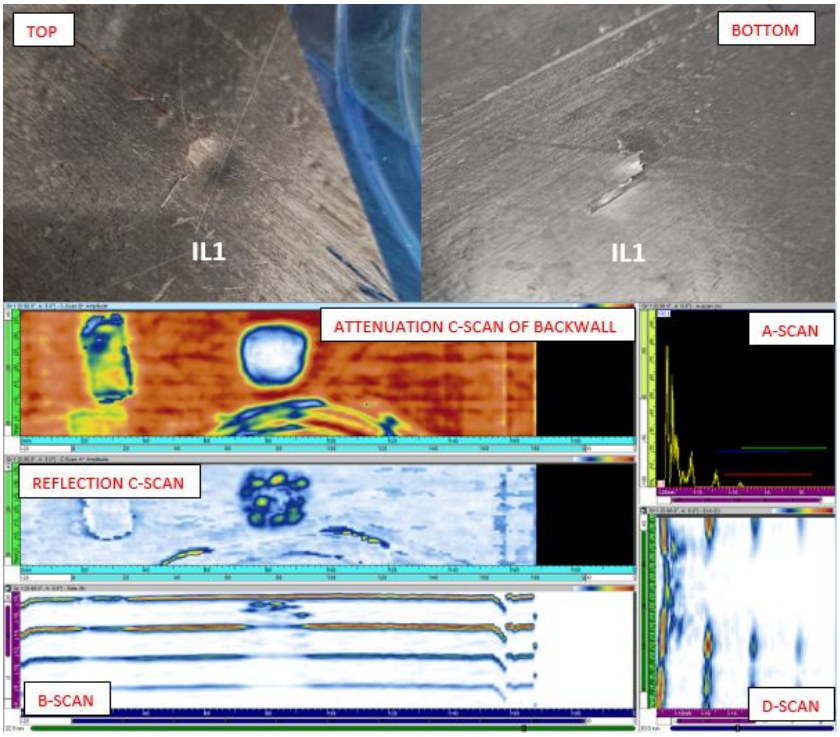

(a) Overall damage, consisting of pictures and active SHM scan

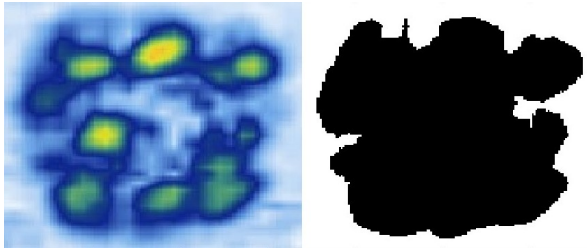

(b) Montage of damaged area

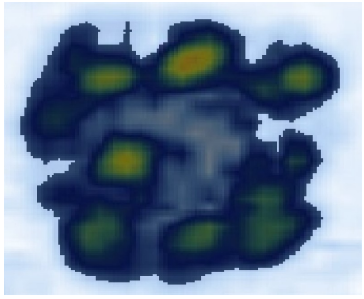

(c) Blend of damaged area

Figure B.1: IL1 damage after 50J impact, of which the top is dented, delaminations are present over the entire thickness and the bottom is cracked.

IL2

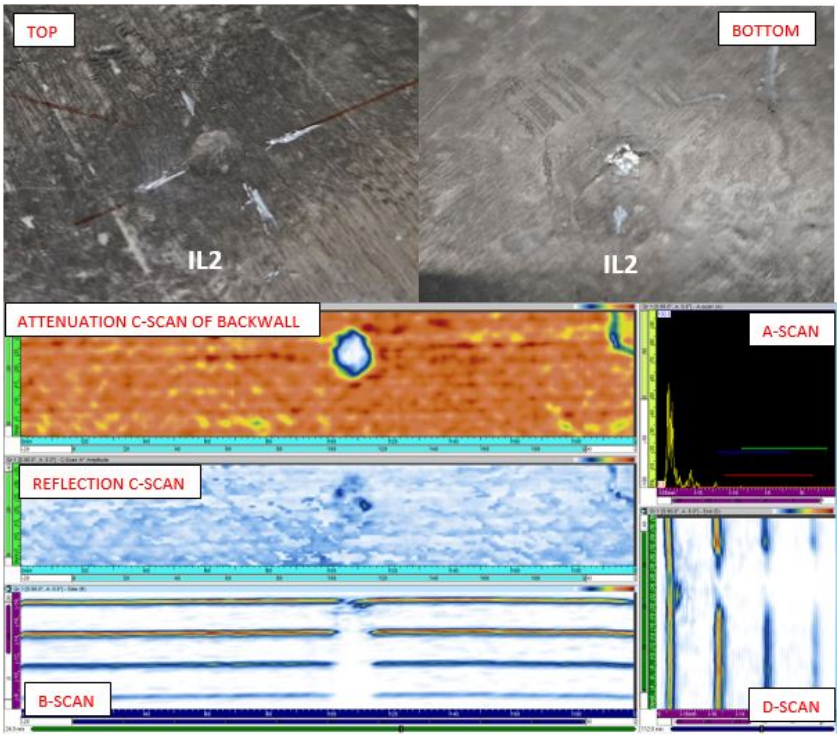

(a) Overall damage, consisting of pictures and active SHM scan

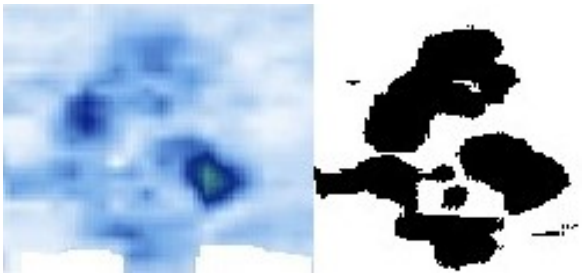

(b) Montage of damaged area

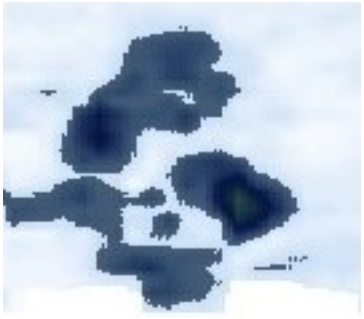

(c) Blend of damaged area

Figure B.2: IL2 damage after 85J impact, of which the top is dented, delaminations are present over the entire thickness and the bottom is cracked.

IL3

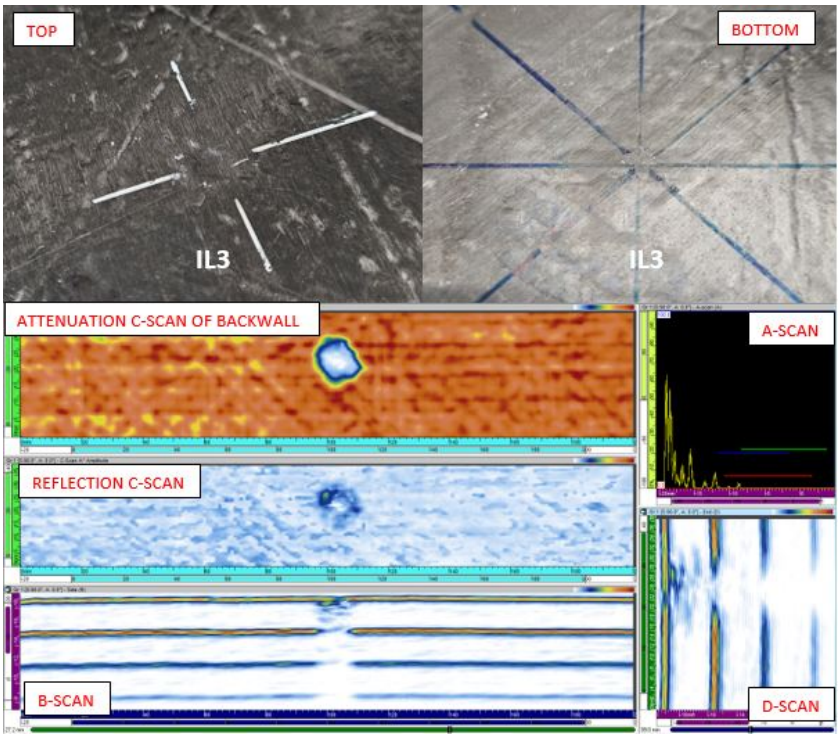

(a) Overall damage, consisting of pictures and active SHM scan

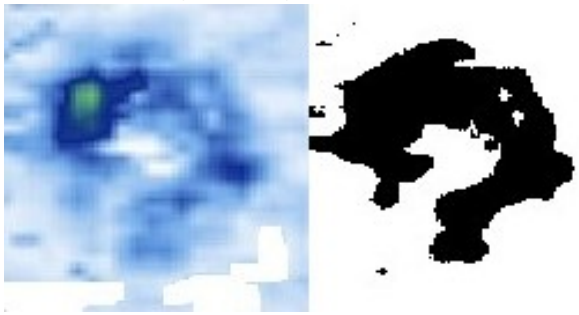

(b) Montage of damaged area

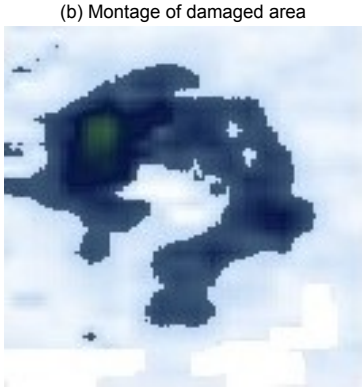

(c) Blend of damaged area

Figure B.3: IL3 damage after 85J impact, of which the top is dented and delaminations are present at the surface.

IL4

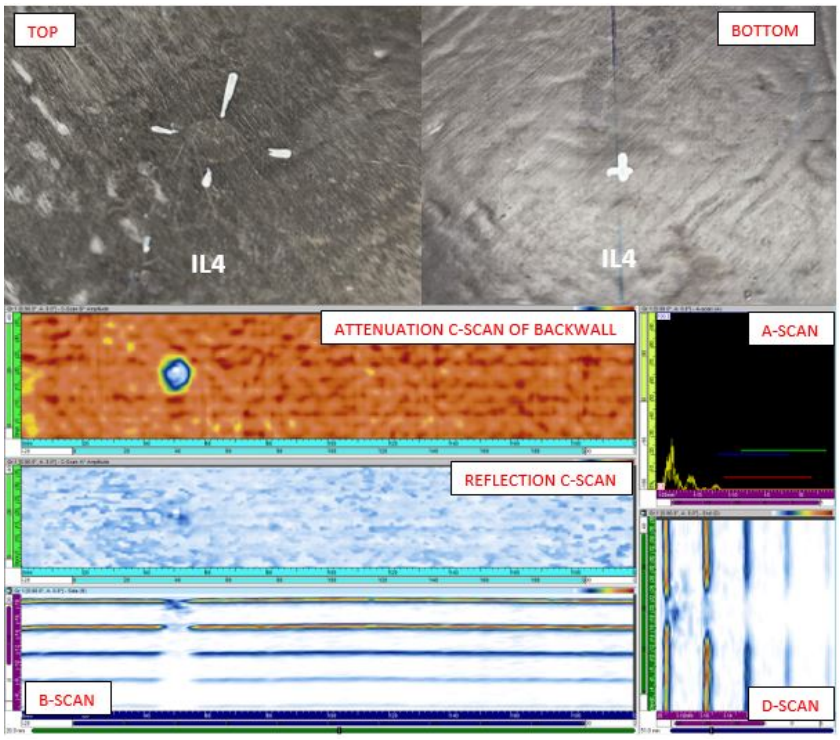

(a) Overall damage, consisting of pictures and active SHM scan

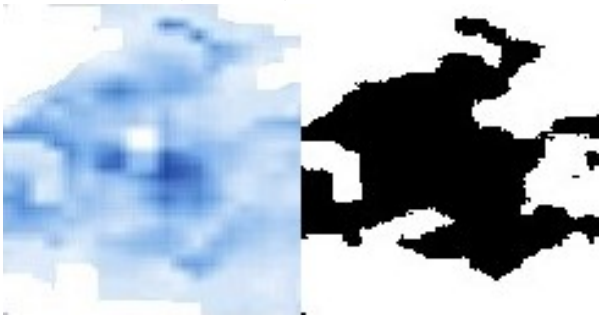

(b) Montage of damaged area

(c) Blend of damaged area

Figure B.4: IL4 damage after 45J impact, of which the top is dented, delaminations are present at the surface and the bottom is dented.

IL5

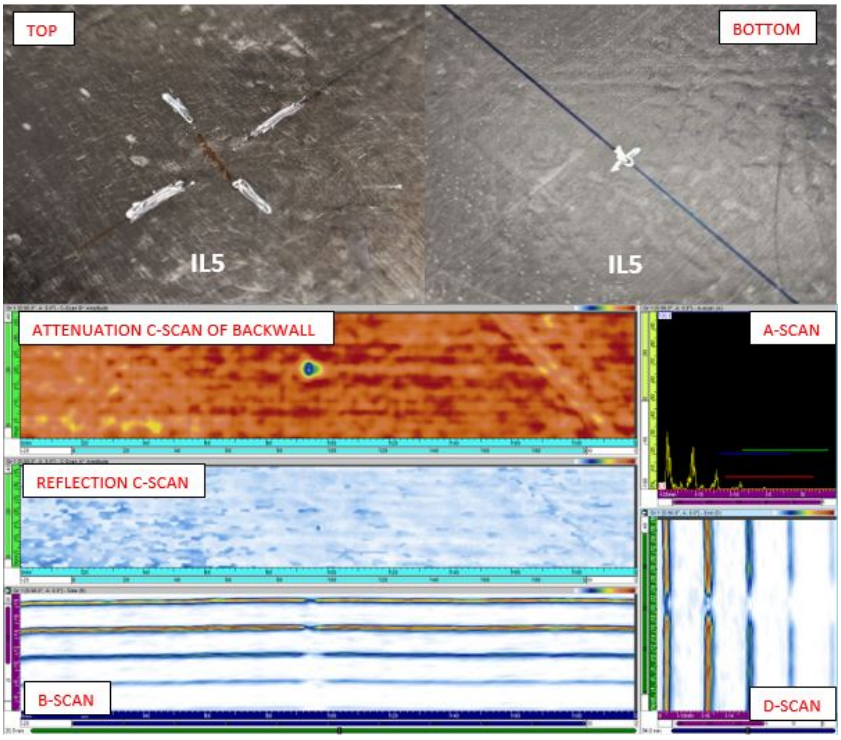

(a) Overall damage, consisting of pictures and active SHM scan

Figure B.5: IL5 damage after 45J impact, of which the top is slightly dented and no internal damages (no attenuation in the reflection C-scan).

IL6

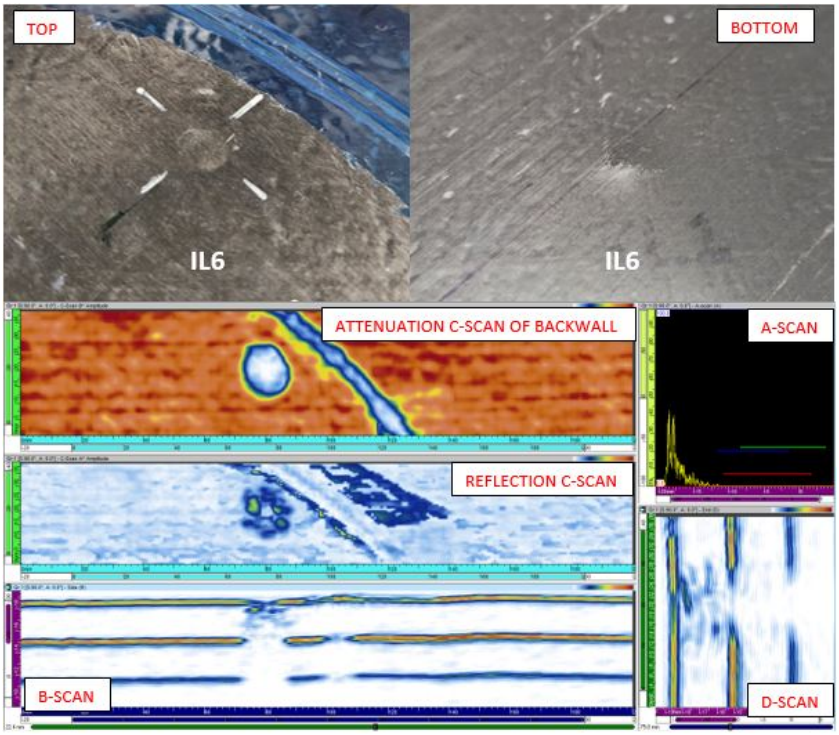

(a) Overall damage, consisting of pictures and active SHM scan

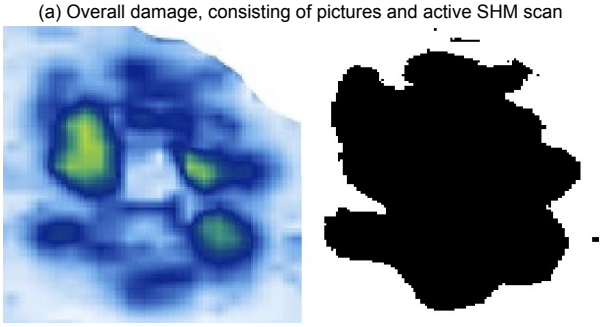

(b) Montage of damaged area

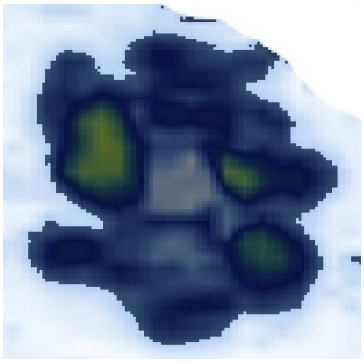

(c) Blend of damaged area

Figure B.6: IL6 damage after 80J impact, of which the top is dented and cracked, delaminations are present at the surface level and the bottom is cracked.

IL7

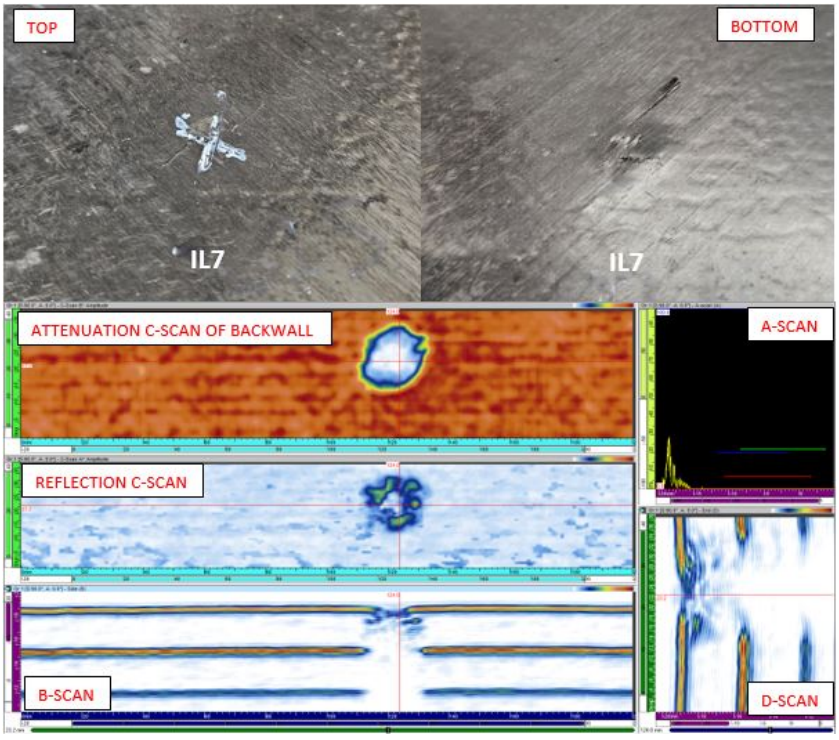

(a) Overall damage, consisting of pictures and active SHM scan

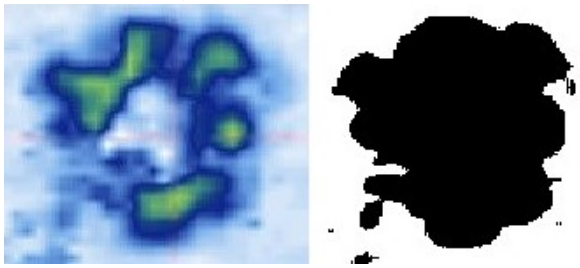

(b) Montage of damaged area

(c) Blend of damaged area

Figure B.7: IL7 damage after 70J impact, of which the top is dented and cracked, delaminations are present at the surface level and the bottom is cracked.

IL8

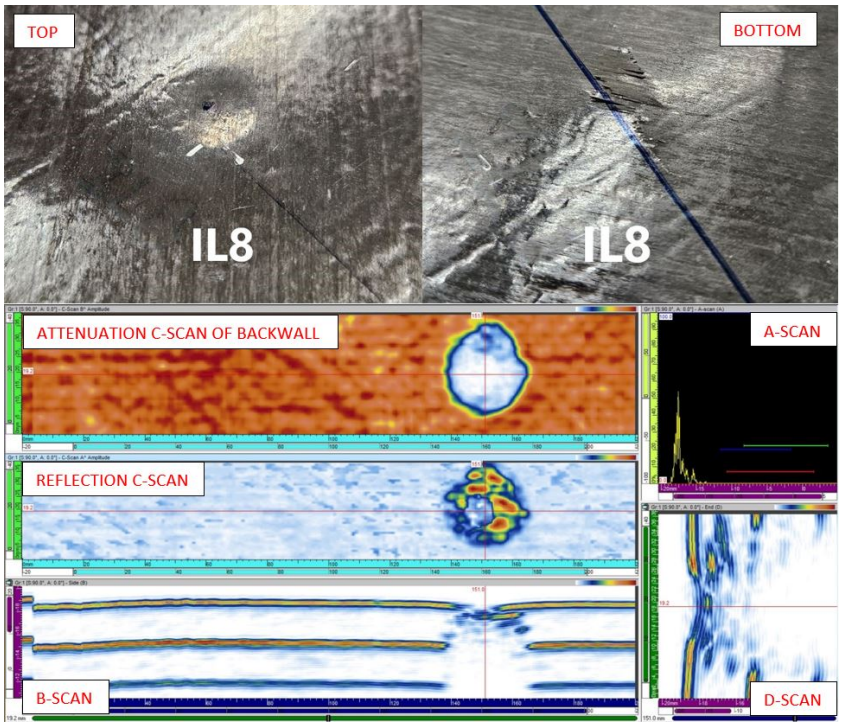

(a) Overall damage, consisting of pictures and active SHM scan

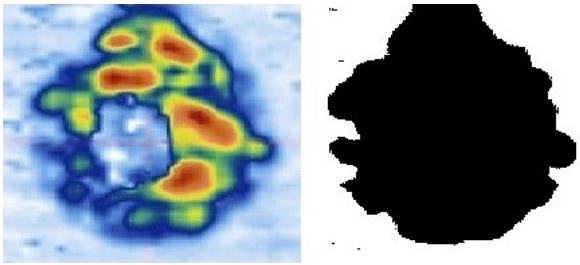

(b) Montage of damaged area

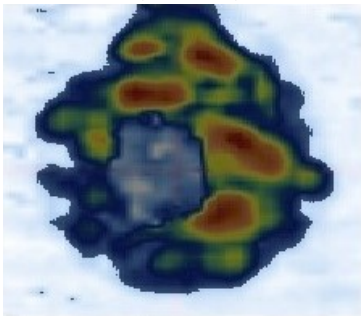

(c) Blend of damaged area

Figure B.8: IL8 damage after 170J impact, of which the top is dented, delaminations are present till halve the thickness of the panel and the bottom is cracked.

IL9

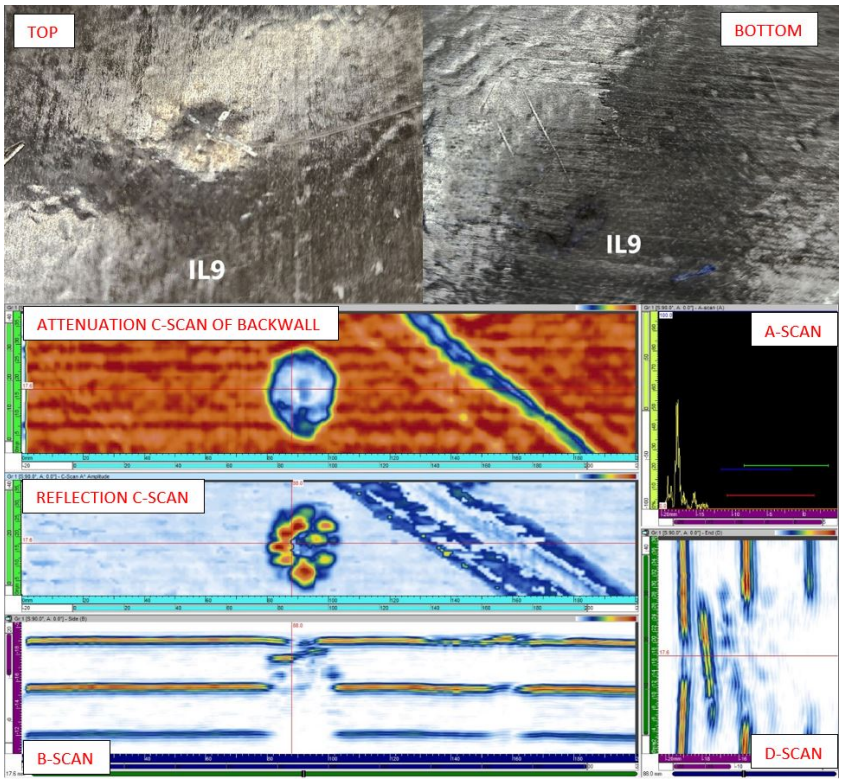

(a) Overall damage, consisting of pictures and active SHM scan

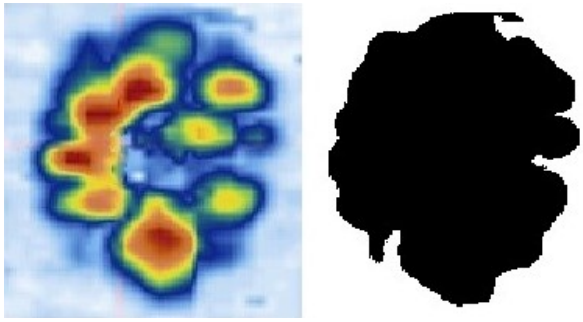

(b) Montage of damaged area

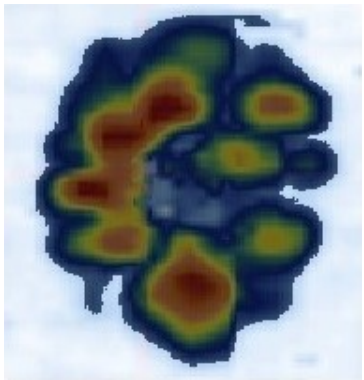

(c) Blend of damaged area

Figure B.9: IL9 damage after 130J impact, of which the top is dented, delaminations are present till halve the thickness of the panel and the bottom is cracked.

IL10

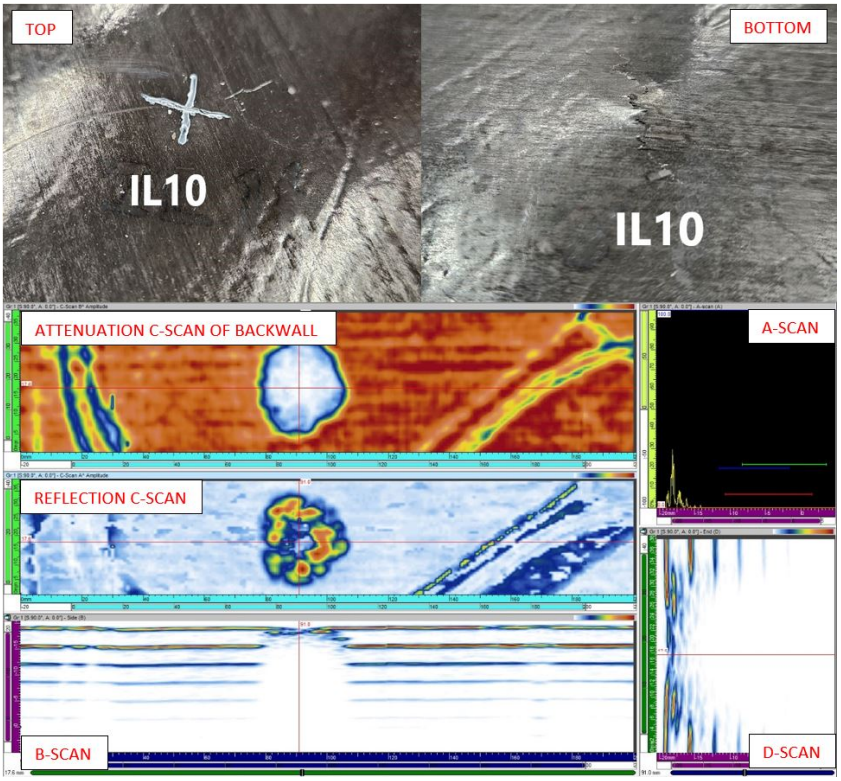

(a) Overall damage, consisting of pictures and active SHM scan

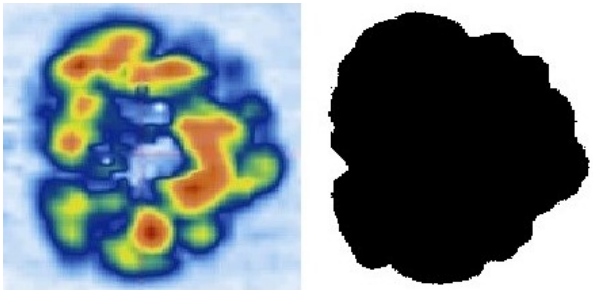

(b) Montage of damaged area

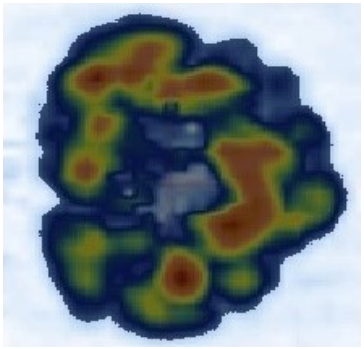

(c) Blend of damaged area

Figure B.10: IL10 damage after 170J impact, of which the top is dented, delaminations are present over the entire thickness of the panel and the bottom is cracked.

IL11

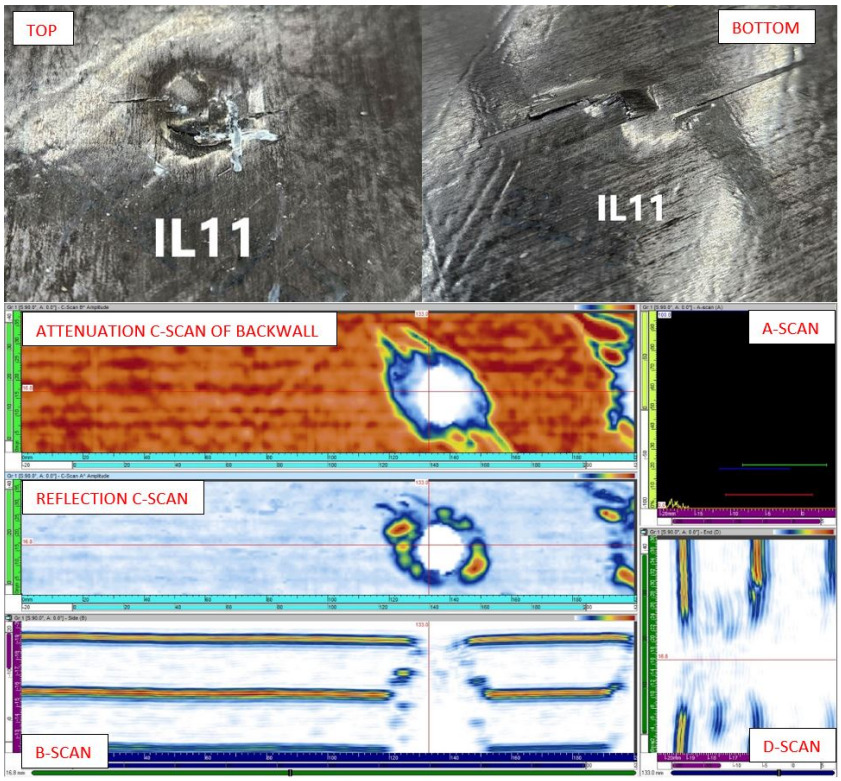

(a) Overall damage, consisting of pictures and active SHM scan

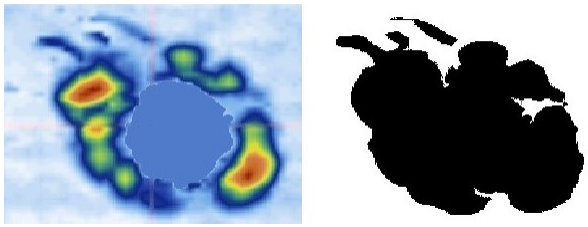

(b) Montage of damaged area

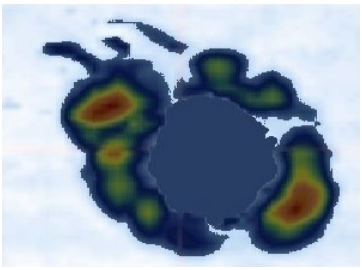

(c) Blend of damaged area

Figure B.11: IL11 damage after 100J impact, where a near puncture has occurred, delaminations are present over the entire thickness of the panel and the bottom is cracked.

IL12

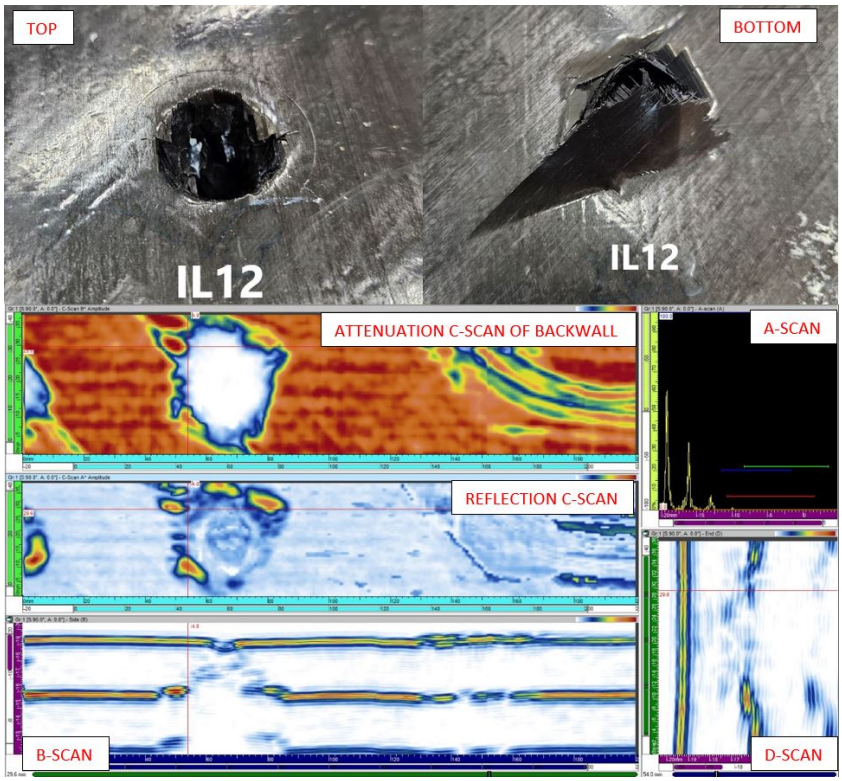

(a) Overall damage, consisting of pictures and active SHM scan

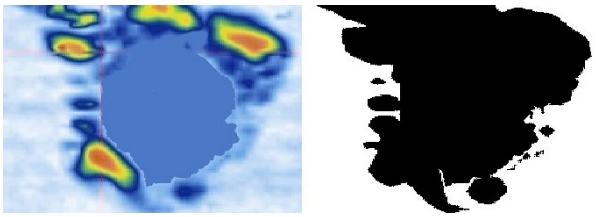

(b) Montage of damaged area

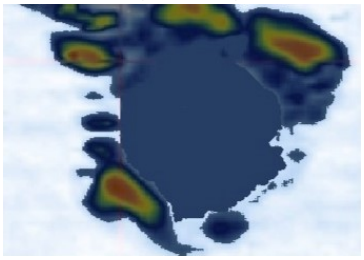

(c) Blend of damaged area

Figure B.12: IL12 damage after 170J impact, at which a penetration has occurred and where delaminations outside the penetrated area are present.

Damage overview

Table B.1: Damage overview and the damage sizes for each impact level on the flat panel.

IL [#]	DAMAGE		
	Image reference	Damage type	Damage size [mm^2]
1	B.1	Dented Delaminated Cracked	361
2	B.2	Dented Delaminated Cracked	129
3	B.3	Dented Delaminated	143
4	B.4	Dented Delaminated	179
5	B.5	Dented	0
6	B.6	Dented Cracked Delaminated	246
7	B.7	Dented Cracked Delaminated	314
8	B.8	Dented Delaminated Cracked	657
9	B.9	Dented Delaminated Cracked	529
10	B.10	Dented Delaminated Cracked	701
11	B.11	Near puncture Delmainations	745
12	B.12	Puncture Delaminations	1094

B.2. Stiffened panel

IL1

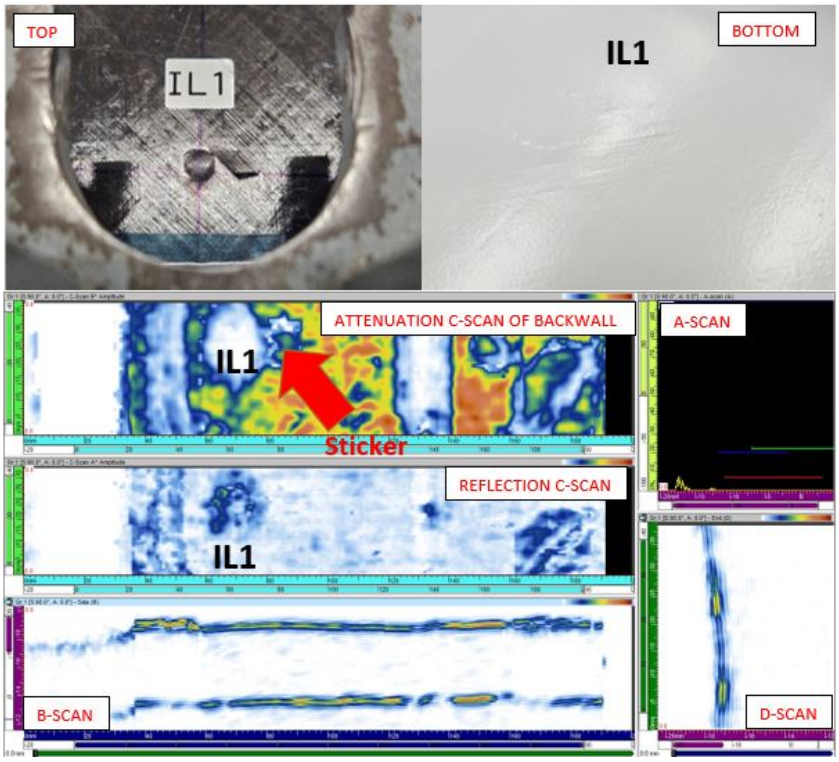

(a) Overall damage, consisting of pictures and active SHM scan

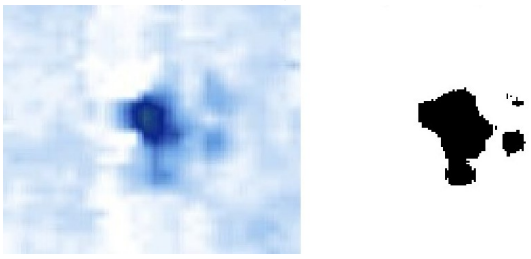

(b) Montage of damaged area

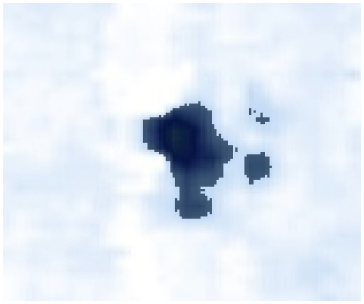

(c) Blend of damaged area

Figure B.13: Damage at IL1 on the stiffened panel after 55J impact, containing a dent with a crack on the surface and internal damage.

IL2

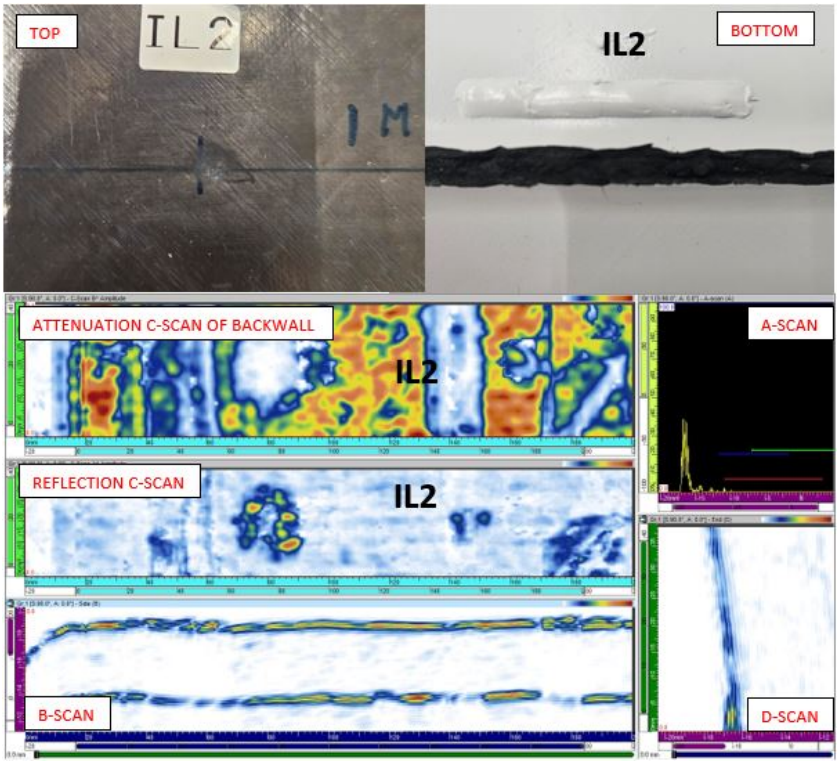

(a) Overall damage, consisting of pictures and active SHM scan

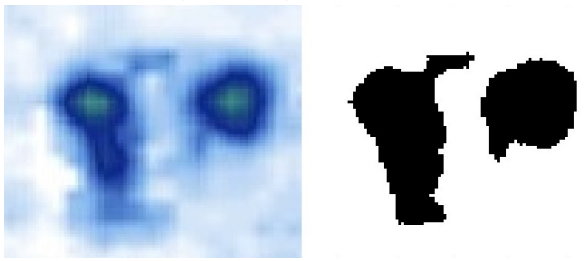

(b) Montage of damaged area

(c) Blend of damaged area

Figure B.14: Damage at IL2 on the stiffened panel after 70J impact, containing a dent and internal damage.

IL3

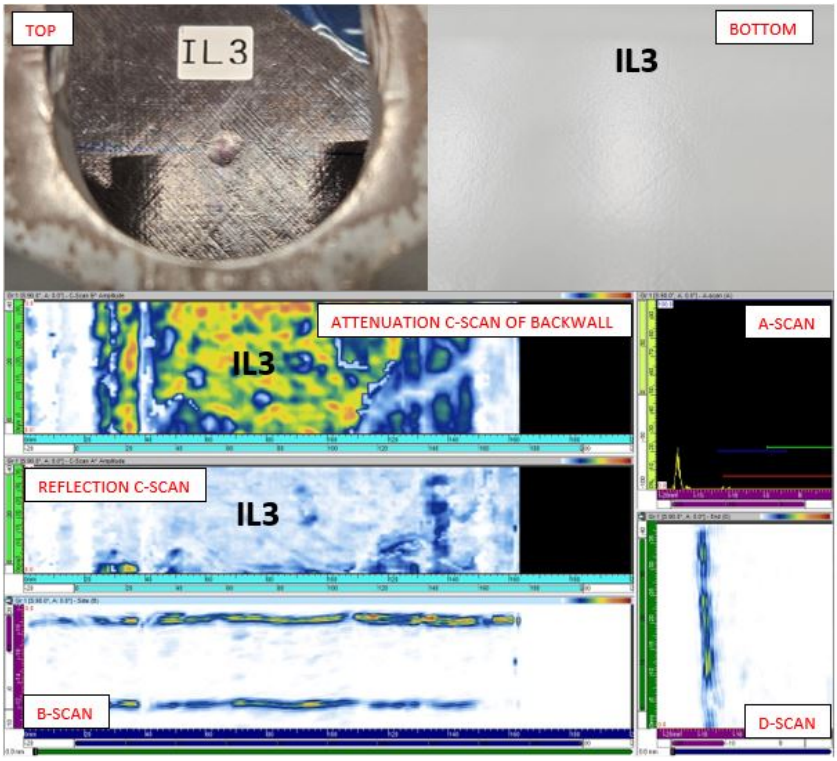

(a) Overall damage, consisting of pictures and active SHM scan

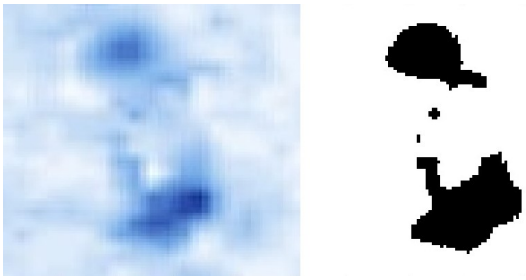

(b) Montage of damaged area

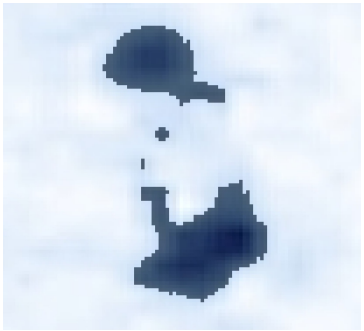

(c) Blend of damaged area

Figure B.15: Damage at IL3 on the stiffened panel after 55J impact, containing a dent and internal damage.

IL4

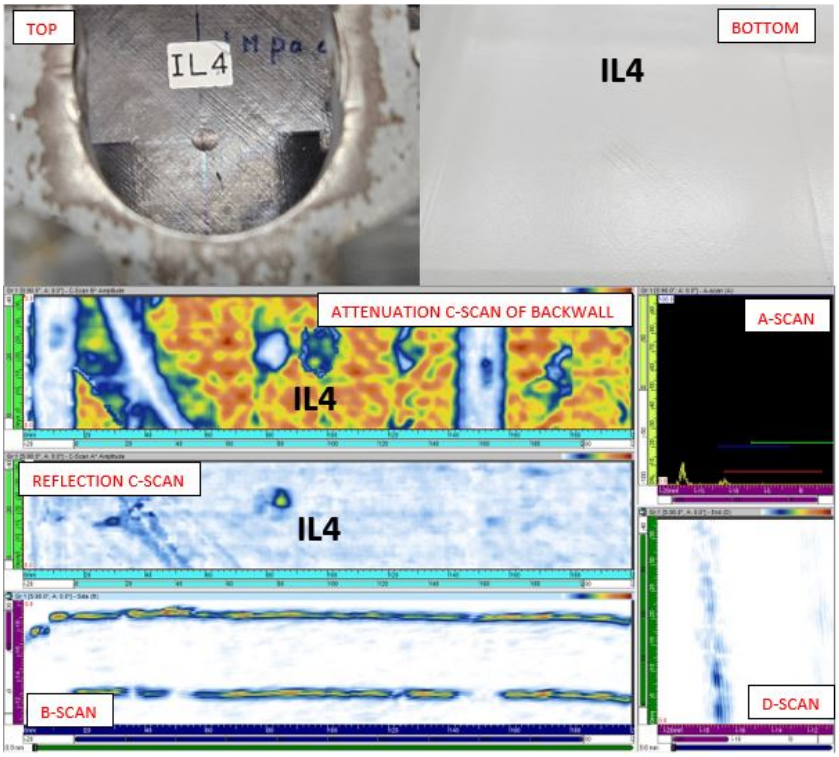

(a) Overall damage, consisting of pictures and active SHM scan

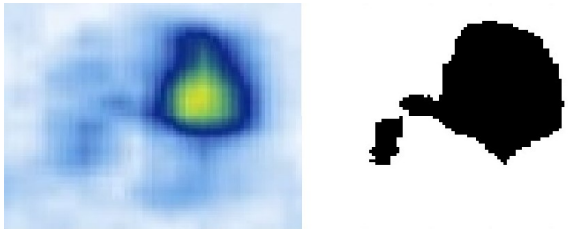

(b) Montage of damaged area

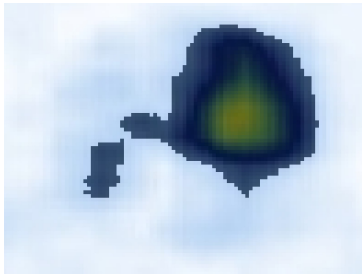

(c) Blend of damaged area

Figure B.16: Damage at IL4 on the stiffened panel after 50J impact, containing a dent and internal damage.

Damage overview

Table B.2: Damage overview and the damage sizes for each impact level on the flat panel.

IL [#]	DAMAGE		
	Image reference	Damage type	Damage size [mm^2]
1	B.13	Dented Cracked Internal damage	45
2	B.14	Dented Internal damage	79
3	B.15	Dented Internal damage	45
4	B.16	Dented Internal damage	55